KU LEUVEN

ARENBERG DOCTORAL SCHOOL

Faculty of Science

Investigation of Self-Assembled Monolayers (SAM) for Advanced Interconnects Schemes

Yiting Sun

Supervisors:

Prof. Steven De Feyter

Dr. Silvia Armini

Dissertation presented in partial fulfillment of the requirements for the degree of Doctor of Science (PhD): Chemistry

June 2017

Investigation of Self-Assembled Monolayers (SAM) for Advanced Interconnects Schemes

Yiting SUN

Examination committee:
Prof. Thierry Verbiest, chair
Prof. Steven De Feyter, supervisor
Dr. Silvia Armini, supervisor
Prof. Stefan De Gendt
Prof. Christophe Detavernier
Dr. Guy Vereecke
Prof. Mikhail Baklanov
(NCUT)

Dissertation presented in partial fulfillment of the requirements for the degree of Doctor of Science (PhD): Chemistry

June 2017

Uitgegeven in eigen beheer, Yiting Sun, Kapeldreef 75, B-3001 Leuven (Belgium)

是日已過．命亦隨減．
如少水魚．斯有何樂．
大眾．
當勤精進．如救頭燃．
但念無常．慎勿放逸．
——普賢警眾偈

With the passing of this day,
Our lives are that much less.
Just like a fish in a shrinking pond,
How could pleasure and amusement bring happiness?
Followers!
Endeavour with diligence now,
as if putting out fire on your head.
Remember the transitory nature of life,
be watchful not to indulge in idleness

– Samantabhadra Bodhisattva's Verse For Admonition Of The Assembly

Acknowledgement

First of all, I would want to thank my promoter Professor Steven De Feyter for the continuous support through so many years. His insight and vision in science have shed light through the mist. He always found time for me in his tight schedule.

I would like to express my sincere gratitude to my advisor Dr. Silvia Armini, who has been my rock and supported me consistently. She gave me the chance of starting my PhD in this exciting field which rejuvenated my life. There are tough times during my PhD when I felt lost and it was she who kept me going and encouraged me with her great patience. As both a successful female scientist and a very nice person, she gives me the freedom to pursue and explore in my field yet holds me to a high standard, motivates me by her dedication and her contagious enthusiasm for research. This PhD would not be possible without her.

I would want to thank Dr. Mikhail Baklanov. I received invaluable advice from him with regards to my data analysis and design of experiments. He is one of the smartest people I know. I always get inspired and motivated from the discussions with him. As a very nice mentor, he always seeks to promote the growth of students, nourish their study with his experience, knowledge, and brilliance. Instead of giving answers, he likes to provoke thinking by asking questions. He is influencing me by sharing his joy in research yet he is demanding and has strict criteria for research.

I would want to thank the members of my committee - Professor Stefan De Gendt - for his suggestions in improving this research. I would want to thank Guy Vereecke for his scientific advice in TDS measurements and FTIR. I would like to thank Professor Thierry Verbiest for chairing my PhD committee. I would want to thank my program managers Tőkei Zsolt and Boemmels Juergen, my managers Peter Leunissen and Herbert Struyf for helpful career advice and providing me with space to do my research. Xiumei Xu for sharing scientific insights with me, Jean-Francois de Marneffe for valuable comments to my paper (via Ferrata are amazing, thanks for racing with a train to get us back to Leuven) and Quoc Toan Le for the discussion in cleaning and XPS. I feel lucky to have the chance to know all low-k guys who are very helpful and resourceful: Liping Zhang (thanks for the help on low-k etch and the discussions) and Patrick Verdonck (thanks for depositing low-k wafers and GISAX measurements). Thanks, Professor Uedono for PAS measurement. Thanks Ainhoa for help in SAMs spin coating, thanks, Arantxa, Tinne and Jana for their pioneering experiments on SAM which paved the way for my PhD. Thanks Elisabeth Levrau and Professor Christophe Detavernier who helped on ALD deposition. Thanks, my lunch pals Murad, Markus and Abitosh for the entertaining time we experienced. Thanks, my loyal friends who support no matter what: Rocky Wang, Chengxun Liu, Liu Yang, Xiumei Xu, Ming Zhao. Thanks, my dear parents and my brother who indulge me pursuing what I want to do. Thanks, my precious daughter Alisa, who enriches my life and brings exceptional meaning into it. Thank you М и ш а for your accompany and support. You are such a person who is like sunshine which radiates energy to people close to you. Your intelligence, your kindness in helping others unconditionally and your dedication to work always makes me respect you and I feel very lucky to know you.

Yiting
June 2017

Abstract

To address the problem of increasing resistance-capacitance (RC) delay with interconnect downscaling, porous low-k materials are introduced as a replacement for the traditional SiO_2 dielectric. The carbon-rich chemistry and porous structure of these materials bring in new challenges in integrating them into Back-End-of-Line (BEOL) fabrication. One of the biggest challenges is metal, moisture and barrier precursor diffusion into the pores, which increases the k value. In this PhD work, the possibility of sealing porous low-k materials with self-assembled monolayers (SAMs) is explored. The SAMs pore sealing strategy consists of three steps: i) pretreatment of the low-k surface in order to introduce silanol groups indispensable for SAM attachment; ii) deposition of SAM to seal the low-k surface against the subsequent barrier precursor; iii) formation of a thin metal barrier to avoid the penetration of moisture and copper ions. The focus of this work is the first step: to compare different pretreatments for low-k surface activation, with a purpose to enable SAM deposition. Four types of pretreatments are studied and explored. For each individual pretreatment, a SAM deposition followed by a metal barrier deposition is performed to test the effectiveness of pretreatments. In the first part of this work, the relationship between hydrophilic layer thickness, pore size, and SAMs distribution is studied. Understanding is gained that surface-confined pretreatment is crucially important for the pore sealing with SAMs.

The target of successful pretreatments is maximizing the surface silanol group density while minimizing the thickness of the damage layer. In the first method, three wet treatments are studied and this method can not introduce sufficient silanol group density on the surface. The second method is to evaporate a thin silicon film on top of low-k then oxidize it to silicon dioxide as add-on hydrophilic layer. This process, however, can not be accurately controlled and might be problematic when fabricating patterned structures. An integration based method is also tested. In this method, the low-k pores are stuffed with a polymer-based protector during fluorocarbon plasma patterning, afterwards, the polymers are removed by thermal annealing. It is found that the polymers stuffing approach can reduce low-k damage but is less efficient in mitigating damage from vacuum ultraviolet (VUV). Pretreatments by plasmas are studied as a fourth method and CO_2 plasma is the preferred pretreatment because the CO_2 ions have high oxidizing potential and get easily discharged, therefore it can create silanol groups on the surface without damaging the deeper layer of low-k film.

Samenvatting

Om het probleem van toenemende weerstand capaciteit (RC) delay bij interconnect downscaling aan te pakken, worden poreuze lage-k materialen geïntroduceerd ter vervanging van de traditionele SiO_2 diëlectrica. De koolstofrijke chemie en poreuze structuur van deze materialen brengt nieuwe uitdagingen voor integratie lijdens Back-End-of-Line (BEOL) fabricatie. Eén van de grootste uitdagingen is metaal-, vocht- en barrière-precursor-diffusie in de poriën, wat aanleiding geeft tot een toename van de k-waarde. In deze PhD studie wordt de mogelijkheid van het afsluiten van de poreuze lage-k materialen met zelf-geassembleerde monolagen (SAM) uitgezocht. De SAMs poriënafdichtingsstrategie bestaat uit drie stappen: i) voorbehandeling van het laag-k oppervlak om silanolgroepen te introduceren die onontbeerlijk zijn voor SAM-binding; ii) afzetting van SAM om het laag-k oppervlak tegen de volgende barrière precursor te verzegelen; iii) vorming van een dunne metaalbarrière om de penetratie van vocht en koperionen te voorkomen. De focus van dit werk is de eerste stap: het vergelijken van diverse voorbehandelingen voor lage-k oppervlakte activatie, met als doel SAM depositie in staat te stellen. Verschillende soorten voorbehandelingen worden bestudeerd en onderzocht. Voor elke individuele voorbehandeling wordt een SAM-afzetting gevolgd door een metaalbinderafzetting uitgevoerd om de effectiviteit van voorbehandelingen te testen. In het eerste deel van dit werk wordt de relatie tussen hydrofiele

laagdikte, poriegrootte en SAMs-verdeling bestudeerd. Daaruit blijkt dat oppervlaktebehandeling cruciaal is voor een goede afsluiting van de poriën met SAMs. Een reeks voorbehandelingen worden getest met als doel de dichtheid van silanolgroepen aan het oppervlak te maximaliseren en de dikte van de beschadigingslaag te minimaliseren. In de eerste methode, drie "natte"behandelingen worden getest en geen enkele van deze kan voldoende silanolgroepen aan het oppervlak introduceren. De seconde methode is het verdampen van een dunne siliciumfilm op het lage-k materiaal. Oxidatie van die film tot siliciumdioxide vormt een hydrofiele laag. Dit proces kan echter niet nauwkeurig genoeg gecontroleerd worden en kan problemen veroorzaken bij patroonstructuren. Een andere benadering is gebaseerd op het vullen van de lage-k poriën met polymeren in combinatie tijdens fluorkoolstof plasma-patroonvorming, gevolgd door het verwijderen van de polymeren. Deze aanpakt beperkt de schade aan het lage-k materiaal maar is minder efficiënt bij het voorkomen van schade veroorzaakt door vacuüm ultraviolet (VUV) straling. Voorbehandelingen door verschillende plasmas worden bestudeerd. Een behandeling met een CO_2 plasma draagt de voorkeur weg omdat de CO_2 ionen een hoog oxiderend vermogen hebben en gemakkelijk ontladen kunnen worden. Via deze behandeling kunnen silanolgroepen aan het oppervlak gecreëerd worden zonder de diepere lagen van het lage-k materiaal te beschadigen.

Symbols

α	Polarizability, $C \cdot m^2 \cdot V^{-1}$
β	Reactive loss probability
Δ	Amplitude ellipsometric angle (Delta), °
γ	Interfacial energy, $J \cdot m^{-2}$
γ_{loss}	Total loss probability
γ_{rcmb}	Recombination coefficient
μ	Dipole moment, $C \cdot m$
ν	Wavenumber, cm^{-1}
Ψ	Phase ellipsometric angle (Psi), °
ρ	Density, $g \cdot cm^{-3}$
ρ_{res}	Resistivity, $\Omega \cdot m$
θ	Water contact angle, °
θ_{c}	Critical angle, seconds of arc
ε	Permittivity, $F \cdot m^{-1}$
$\varepsilon_{\text{absb}}$	Molar attenuation coefficient, $M^{-1} \cdot m^{-1}$

A	Absorbance
a	Tortuosity
A_{cntct}	Contact area, m^2
B_{eff}	Effective polarizability of a unit of volume
C	Capacitance, F
c	Molar concentration of chemical bonds, M^{-1}
c_l	Speed of light, $3 \times 10^8 m \cdot s^{-1}$
d	Film thickness, nm
d_N	Nominal film thickness, nm
d_S	SiO_2 thickness measured by 2 layer model, nm
E	Energy, keV
f(n)	Parameter calculated from RI, f(n)=$\Delta\big((n^2-1)/(n^2+2)\big)$
F(z)	Collision frequency per unit surface area, $cm^{-2} \cdot s^{-1}$
h	Plank constant, $6.626 \times 10^{34} J \cdot s$
I	Area integration of a peak in FTIR spectra
k	Dielectric constant or relative permittivity
k_b	Boltzmann constant, $1.38 \times 10^{-23} J \cdot K^{-1}$
k_d	Mean depth of radical penetration between two collisions with the pore wall, nm
k_r	Reaction rate constant
k_{SD}	Dielectric constant of the damaged sidewall of low-k

L	Line length, m
l	Path length of light, m
L_{pen}	Radical penetration depth, nm
N	Number of molecules per unit volume, cm^{-3}
n	Refractive index
n_{aft}	Refractive index after the deposition of a thin film based on 1-layer Cauchy model
n_{air}	Refractive index of air
n_{bfr}	Refractive index before the deposition of a thin film based on 1-layer Cauchy model
n_{eff}	Effective refractive index of the multicomponent film.
n_{meas}	Refractive index as measured by spectroscopic ellipsometry
N_{rcmb}	Random walk steps that particles travel before recombination
n_{SAM}	Refractive Index of SAM
n_s	Refractive Index of the low-k skeleton
P	Porosity, %
P_{mp}	Metal pitch, m
q	Pore interconnectivity parameter
q_z	Scattering vector along the direction of the film thickness
R	Resistance, Ω

R_p	Pore radius, nm
S	Surface density of chemical groups, cm^{-2}
T	Temperature, °C
t	Time, s
T_{mt}	Metal thickness, m
T_{SD}	Thickness of the damaged sidewall layer of low-k, nm
V	Volumetric fraction of each component in dielectric film, %
z	Depth, nm

List of Abbreviations

$(EtCp)_2Mn$	Ethyl bisethyl cyclopentadienyl-manganese
Al_2O_3	Aluminium oxide
ALD	Atomic layer deposition
APTMS	(3-aminopropyl) trimethoxysilane
BCN	Boron carbon nitride
BEOL	Back-end-of-line
BN	Boron nitride
CCP	Capacitively coupled plasma
CF_4	Tetrafluoromethane
CL	Wet cleaning to remove post-etch residues
CMOS	Complementary metal–oxide–semiconductor
CMP	Chemical mechanical polishing
CNS	Central nervous system
CNSAM	11-cyanoundecyltrichlorosilane
CO_2	Carbon dioxide
Delta	Amplitude ellipsometric angle
DETA	(3-trimethoxysilylpropyl)diethylenetriamine

ECD	Electrochemical deposition
EDL	Equivalent damage layer
EFTEM	Energy-filtered transmission electron microscopy
EP	Ellipsometric porosimetry
FEOL	Front-end-of-line
FTIR	Fourier transform infrared spectroscopy
H_2O_2	Hydrogen peroxide
H_2SO_4	Sulfuric acid
HF	Hydrogen fluoride
HSE	Health, safety and environment
IC	Integrated circuits
ICP	Inductively coupled plasma
IPA	Isopropanol
ITRS	International technology roadmap for semiconductors
k value	Relative dielectric constant
Low-k	Low dielectric constant material
Mesopores	Pores with diameter between 2 nm and 50 nm
Micropores	Pores with diameter less than 2 nm
MnN	Manganese nitride
MSE	Mean square error
OSG	Organosilicate glass
PEALD	Plasma enhanced atomic layer deposition
PECVD	Plasma enhanced chemical vapor deposition
PGMEA	Propylene glycol monomethyl ether acetate
PID	Plasma-induced damage

pl	Plasma
PMMA	Poly(methyl methacrylate)
PMO	Periodic mesoporous organosilica
p-OSG	Porous organo-silicate glass
Pristine	As-deposited (low-k film)
PS	Pore stuffing pretreatment
PSD	Pore-size distribution
Psi	Phase ellipsometric angle
PVD	Physical vapor deposition
RBS	Rutherford backscattering spectrometry
RH	Relative humidity, %
RI	Refractive index
RIE	Reactive-ion etching
RPM	Revolutions per minute
SAM	Self-assembled monolayer
SE	Spectroscopic ellipsometry
Si(1nm)	Evaporated and oxidized silicon film with 1 nm of nominal evaporated thickness
Si(5nm)	Evaporated and oxidized silicon film with 5 nm of nominal evaporated thickness
SiC	Silicon carbide
SiN	Silicon nitride
SiO_2	Silicon dioxide
SOC	Spin-on carbon
SOG	Spin-on glass

SPM	Sulfuric peroxide mixture
TaN	Tantalum nitride
TDMAT	Tetrakis[(dimethyl)amido]titanium
TEM	Transmission electron microscopy
TEMAH	Tetrakis(ethylmethylamino)hafnium
TiN	Titanium nitride
TiO_2	Titanium oxide
TMAH	Tetramethylammonium hydroxide
TNT	Tantalum-nitride/tantalum stack
TOF-SIMs	Time-of-flight secondary ion mass spectrometry
ULK	Ultra low k (k <2.5)
ULSI	Ultra-large-scale integration
US	Pore unstuffing treatment by thermal annealing
UV	Ultraviolet
UVO	Ultraviolet ozone
VUV	Vacuum ultraviolet
WCA	Water contact angle
WN	Tungsten nitride
XPS	X-ray photoelectron spectroscopy
XRD	X-ray diffraction
XRR	X-ray reflectivity

Chemical structures of precursors

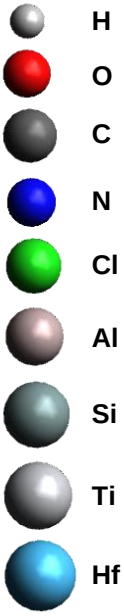

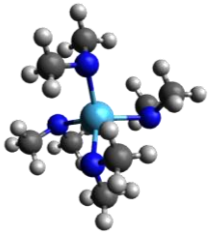

TEMAH
Tetrakis(ethylmethyl-amino)hafnium

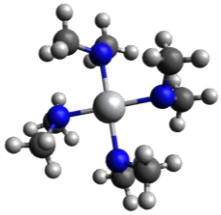

TDMAT
Tetrakis[(dimethyl)-amido]titanium

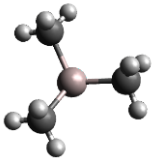

TMA
Trimethyl-aluminium

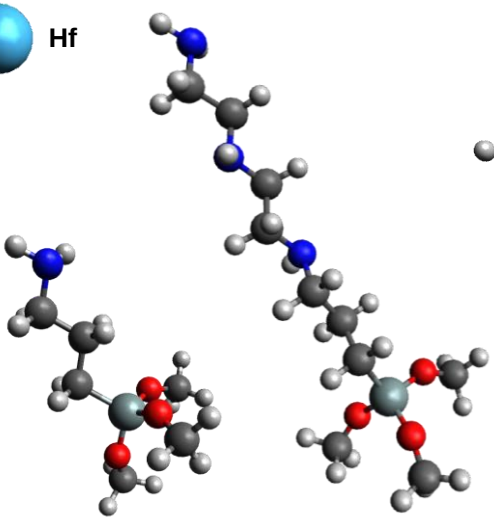

APTMS
(3-aminopropyl)-trimethoxysilane

DETA
(3-trimethoxysilylpropyl)-diethylenetriamine

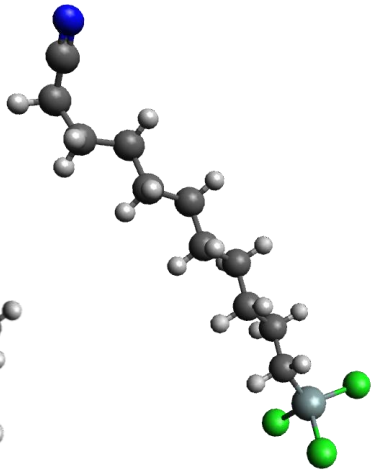

CNSAM
11-cyanoundecyl-trichlorosilane

Contents

Chapter 1

General introduction

1.1 Interconnect and downscaling

The embark of PC and smart phone technique which cause unfathomable changes to human life could be traced back to the middle of 20th century, a miraculous era when the beauty of digital electronics was unveiled with the creation of the first computer. The early generations of electronics were assembled manually from discrete electronic components. People then realized that they can manufacture all components from the same material with different areas doped by electron-rich and electron-deficient impurities, put them on the same substrate and have them interconnected by metal wiring. This revolutionary invention was named as integrated circuits (IC). With the advances in silicon semiconductor manufacturing, mass production of such integrated circuits was made possible. Transistor represents a basic building block of modern devices, while the way of assembly of transistors into simple logic nodes defines the semiconductor technology. Nowadays the majority of ICs are fabricated using a technology called complementary metal–oxide–semiconductor (CMOS) which provides

high noise immunity and low static power consumption and therefore was preferred over its counterparts like N-type metal-oxide-semiconductor.
The IC structure can be divided into two parts: Front-End-of-Line (FEOL) where transistors are formed directly on silicon crystal and Back-End-of-Line (BEOL) where isolated elements are wired by interconnects (Figure 1.1).[1] The function of this wiring system is to distribute clock and other signals and to provide power/ground to the various functional sets. In this thesis, we are focusing on the dielectric material in BEOL interconnects which separates the conducting wires from each other. Figure 1.2 shows the chemical structure of this material.

In 1965, Gordon Moore made an empirical observation that silicon-based IC technology is scalable[3]: the number of transistors in the most advanced ICs doubles approximately every two years. This amazing fact has been driving the whole IC industry for the past several decades both economically and technically: for every few years, people could recycle their electronics and purchase new ones with smaller size, cheaper price and faster speed. This empirical "rule" is also serving as a target that industry has been striving to keep up with, referred to as "roadmap". The huge profit generated was accordingly invested back in the research thus helping to sustain Moore's law, that is why it is called a self-fulfilling prophecy. However, this seemingly perfect loop has hit a hurdle when the feature dimension scaled down to dozens of atoms. Advances in technology are limited by physical law and even the smallest manufacturing fluctuations cause a dramatic change in electrical properties of devices and bring extra burdens on reliability.

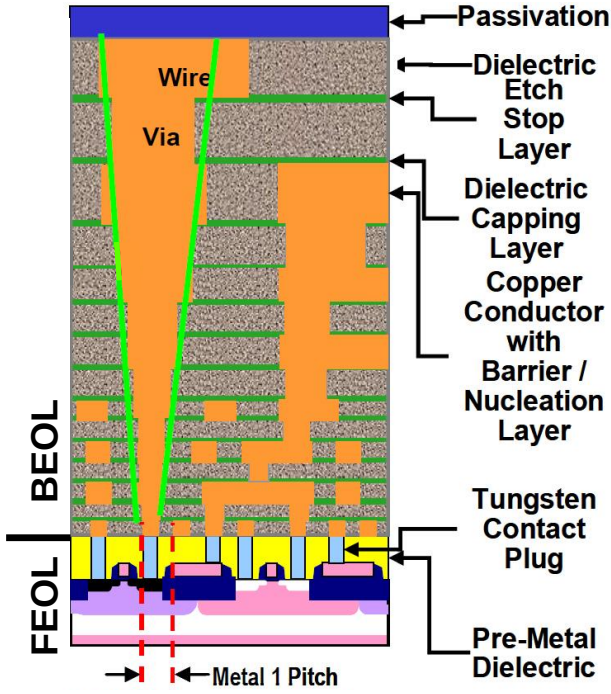

Figure 1.1: Typical Cross-sections of Hierarchical Scaling MPU Device [1]

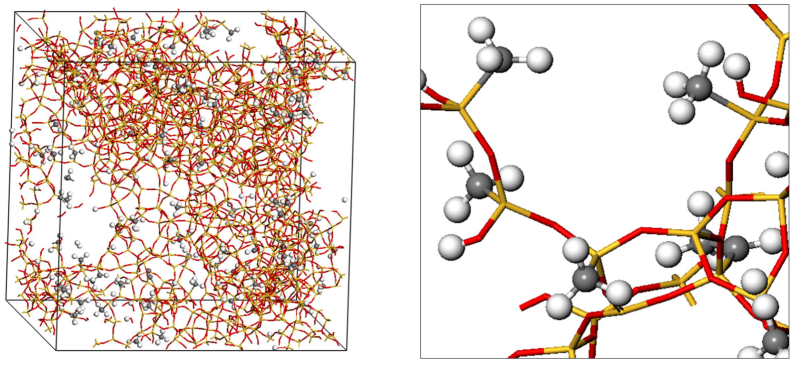

Figure 1.2: 53.5% porous organosilicate structure models and close-up. Silica backbone structure is red (oxygen) and yellow (silicon) with the added hydrogens (white) and carbon (gray) atoms.[2]

1.2 Resistance capacitance (RC) delay and low-k dielectrics

Downscaling influences the device performance in two ways: gate delay and RC delay. RC delay is caused by the capacitance and resistance associated with the metal lines. It is proportional to signal propagation delay and is a widely used figure-of-merit for interconnect performance. The mathematics equation to calculate RC-delay is:

$$R \cdot C = 2 \cdot \rho_{\mathrm{res}} k \varepsilon_0 \cdot \left(\frac{4L^2}{{P_{\mathrm{mp}}}^2} + \frac{L^2}{{T_{\mathrm{mt}}}^2}\right) \tag{1.1}$$

where R is line resistance, C is line capacitance, L is line length, $\mathrm{P_{mp}}$ is metal pitch (sum of line width and line spacing), $\mathrm{T_{mt}}$ is metal thickness, ρ_{res} is resistivity, ε_0 is vacuum permittivity, k is the relative dielectric constant of the interlayer dielectric.

Gate delay refers to the delay caused by the transistors in the Front-End-of-Line (FEOL) gate. As shown in Figure 1.3, in technical nodes of 250 nm and larger, shrinking the dimensions will improve the performance because there is less gate delay. While for smaller nodes, RC delay is more important. Shrinking the cross-section of a wire increases its resistance and bringing wires closer together increases the capacitance between the wires. Therefore as device size decreases, RC delay increases and becomes a serious limitation to performance. In order to decrease the RC delay, metals with low resistivity and dielectrics with low dielectric constant are introduced. The former has been achieved by replacing the conventional Al with Cu (36% decrease in resistivity ρ_{res}) while the latter is being developed by replacing SiO_2 with low-k material which has a lower k value (40% decrease in k value).

Clausius–Mossotti equation (Equation 1.2) is the link between the dielectric

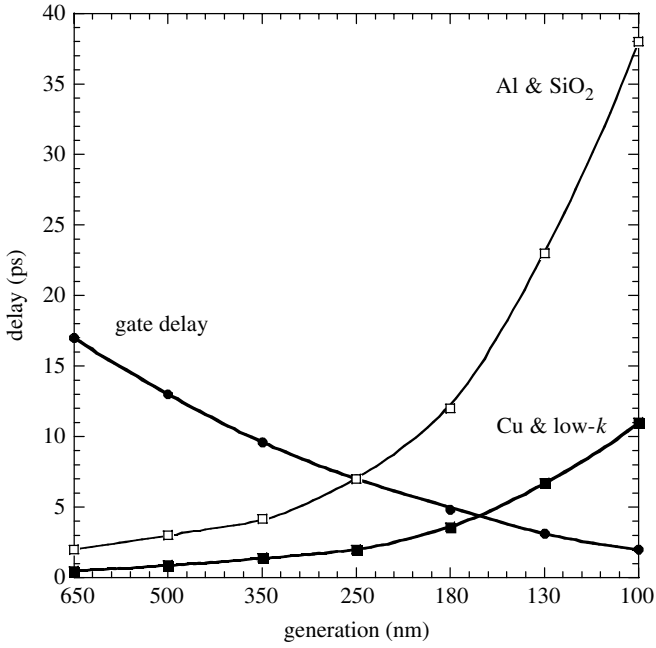

Figure 1.3: Gate and interconnect delay versus technology generation. Reproduced from Havemann et al.[4]

constant of a material with its intrinsic property.

$$\frac{k-1}{k+2} = \frac{N}{3\varepsilon_0}(\alpha_\mathrm{e} + \alpha_\mathrm{i} + \frac{\mu}{3k_\mathrm{b}T}) \tag{1.2}$$

where N is the number density of the species, the parts in the bracket is the molecular polarizability contribution from various species, which contains three terms. The first term α_e is the electronic polarizability, which describes the displacement of the cloud of bond electrons with reference to the nucleus under an applied electric field, α_i is the ionic polarizability which is induced by the displacement of the nuclei by the applied electric field, thereby stretching or compressing the bond length. The third term $\mu/3k_\mathrm{b}T$, describes the dipolar polarization, where μ is the orientation polarizability, $\mathrm{k_b}$ is Boltzmann constant, T is absolute temperature. This

term is the thermal averaging of the permanent electric dipole moments in the presence of an applied field.

As indicated by Equation 1.2, k value of a certain material depends on the density and the polarizability of components. Therefore, there are two possible ways to decrease the k value of a material: i) by decreasing the dipole strength of the chemical bond within the material or ii) by lowering the total number of dipoles. The former is realized by using materials having chemical bonds with lower polarizability than Si-O bonds, like Si-C. The latter is achieved by introducing pores and lowering the density. This is why a porous low-k material consists of CH_X groups has lower k value than SiO_2.

Figure 1.4 and 1.2 shows the structure of low-k deposited by plasma enhanced chemical vapor deposition (PECVD). Compared with traditional SiO_2, porosity and carbon are introduced into this material, which decrease the dielectric constant of the film. -CH_X groups make the film hydrophobic and avoid the uptake of water from the ambient.[5] Figure 1.5 shows the structure of another type of low-k: periodic mesoporous organosilica (PMO). This material is different than PECVD low-k in a way that the pores are arranged in a periodical order, therefore the mechanical properties are better than PECVD low-k.

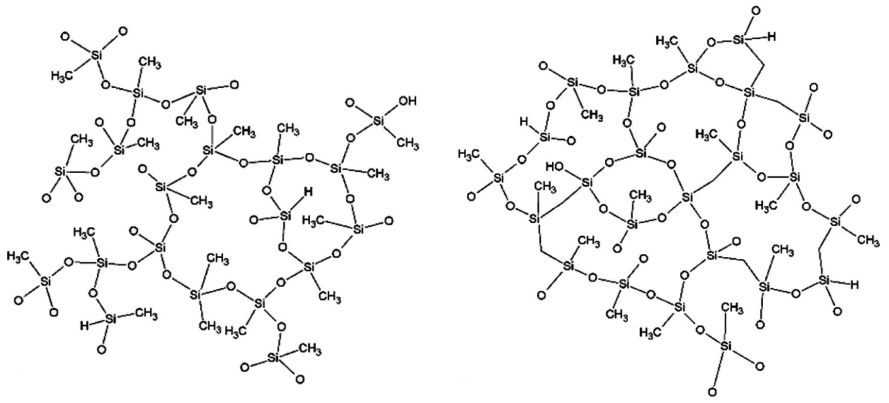

Figure 1.4: Porous SiOCH with and without Si-CH_2-Si bonds [6]

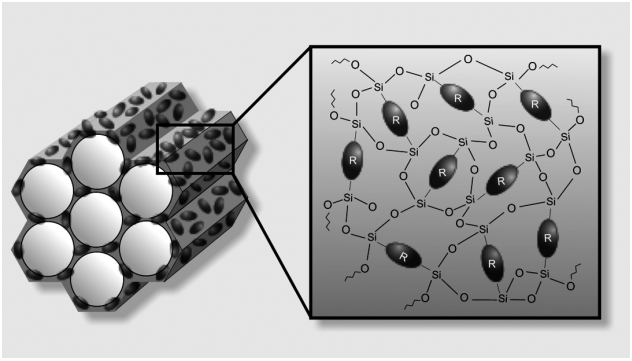

Figure 1.5: Structure of Periodic Mesoporous Organosilica (PMO). R represents organic functional group. [7]

1.3 Damascene process and low-k integration

Semiconductor devices are manufactured in specialized plants called FAB or foundry. The fabrication of integrated circuits can be broadly divided into two phases of FEOL and BEOL. The CMOS fabrication starts from the preparation of silicon monocrystals by purifying sand and after several complicated steps, a cylindrical ingot of the silicon crystal is formed. This cylindrical ingot is then sliced to less than 1 mm disks called "wafers". With

repetitive steps of oxidation, photolithography (normally composed of resist coating, exposure, development, and strip), cleaning, etching, deposition and ion implantation, devices are formed on the wafers. The metal wiring is fabricated with a process called "Damascene".[8] Figure 1.6 shows an example of Cu-damascene process, which includes the following steps:

1. Deposition of inter-level dielectrics
2. Via formation in the inter-level dielectrics using lithography and dry etching
3. Trench formation in the inter-level dielectrics
4. Deposition of metal barrier film
5. Cu seed deposition and Cu filling using electroplating
6. Removal of unnecessary Cu films around the trench region using chemical mechanical polish (CMP), and deposition of interlevel dielectric barriers.

In the contemporary Ultra-Large-Scale Integration (ULSI) devices this procedure would normally be repeated for 6-10 times until a multi-layer wiring system is constructed (Figure 1.1). Eventually, the wafers are cleaved into small blocks with certain circuit function (called "dies") and then packaged as individual chips. Figure 1.7 give examples of BEOL stack used by industry[10]by the time this dissertation is prepared, showing where low-k is used.

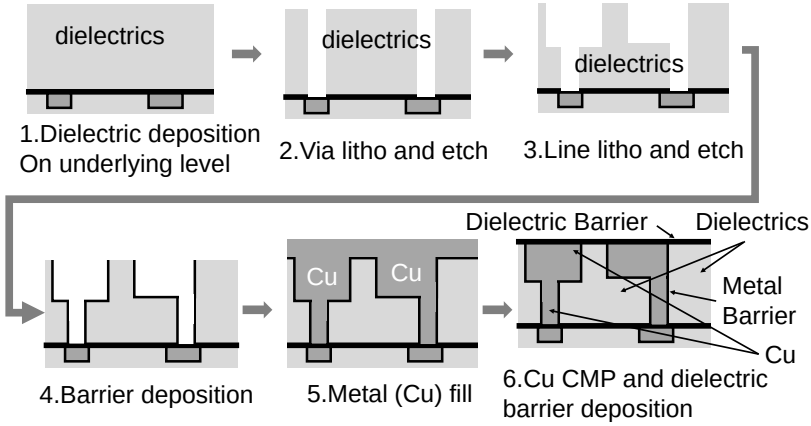

Figure 1.6: Schematic representations of the dual damascene copper/dielectrics integration. Reproduced from Baklanov et al. [9]

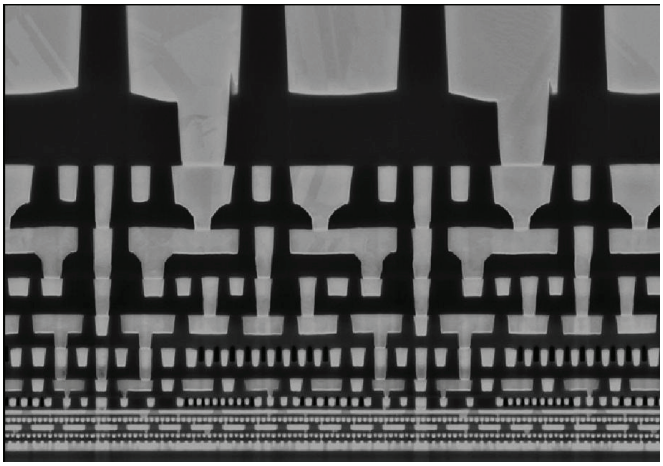

Figure 1.7: BEOL stack of Intel's 14 nm logic IC with 52 nm pitch at metal 2. Metal 0 - Metal 11 in cross section. Low-k is used in metal 0-10. [10]

1.4 Barrier indiffusion and pore sealing challenges

The integration of porous ultra-low k materials into damascene process is challenging: the pores in the dielectric lowers the mechanical strength of the material. In the second step of etching (Figure 1.6), the plasma species penetrate, break Si-CH_3 bonds and turn the top part of SiCOH low-k film into a SiO_2-like material. This top part chemically modified by plasma is called "damage layer". In the 4th step of metal barrier deposition, species from barrier precursors can diffuse into the pores. Those penetrations are undesirable, as they cause a change in the electrical properties of the dielectric, which may severely undermine device performance. [11][12][13]On microporous low-k with a pore size smaller than 2 nm, the barrier precursor is less likely to penetrate due to steric effects. However, on mesoporous low-k, an additional sealing layer is needed in order to avoid barrier precursor penetration.

In order to keep capacitance within spec, the most important parameters of sealing layer are k value and the minimal thickness. Figure 1.8 shows the isocapacitive curves of k value and thickness of the damaged sidewall obtained by simulation. k_{SD} is the k value of the sidewall. T_{SD} is the thickness of the sidewall, including damage layer, sealing layer and the part of low-k contaminated by barrier precursor (If the sealing layer is working well, the thickness of metal barrier indiffusion layer is 0). According to ITRS roadmap, only 2.4% capacitance increase is tolerable for next generation technical node. Therefore (k_{SD},T_{SD}) must fall in the light grey zone. If a sealing layer with relatively high k value might be considered, it must be able to seal with very small thickness. Table 1.1 lists the dielectric constant of some dielectrics. Some of them have been considered as a candidate for sealing material. For example if SiN is used as sealing layer, the thickness has to be limited to 0.2 nm in order to have only 2.4% increase in capacitance. The k value for water is also listed for reference.

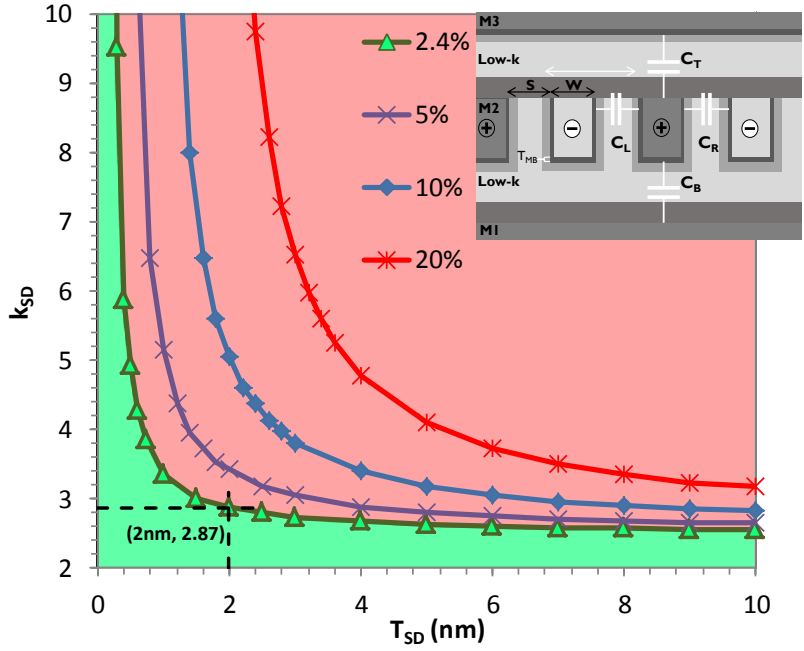

Figure 1.8: Isocapacitive curve for International Technology Roadmap (ITRS) sidewall specs on capacitance. The "sidewall damage" (SD) refers to all the parts of low-k affected by damascene processing steps: the plasma damaged layer, the sealing layer and the indiffusion layer from metal barrier deposition. Legend is the capacitance increase due to side wall damage. T_{SD} is the thickness of damaged sidewall. k_{SD} is the k value of the damaged sidewall.[14]

In addition to thickness and k value, there are several other parameters equally important for a successful sealing. The most important criteria of pore sealing layer are listed below:

- **Thin**: The total thickness of sealing/densified/sealant diffusion layer has to be less than 3 nm. The surface vs. bulk selectivity of the sealant deposition procedure should be high to avoid diffusion.
- **Dense**: The sealing layer has to be dense and pinhole free

Table 1.1: k value of materials

Material	k value
SiO_2	3.9
Al_2O_3	9.1
H_2O	80.1
TiO_2	86.0-173.0
SiN	7.0-8.0
SiC	9.5-10.0
BN	4.2-4.6
BCN	3.9

- **Adhesive**: The sealing layer should be able to help the nucleation of subsequent metal barrier/metal deposition
- **Damage-free**: the sealing process should not damage low-k

The first two items in themselves are already contradicting to realize. Despite decades of efforts, it is still not easy to seal the porous low-k material. The sealing layers are either too thick, indiffusing too deep, not dense enough, not compatible with barrier, or deteriorating adhesion. In next chapter, the pore sealing solutions found in literature will be reviewed in terms of those criteria.

Chapter 2

Introduction of pore sealing

2.1 State-of-the-art of pore sealing

Ever since the introduction of porous low-k material, the copper and metal barrier diffusion problem comes along. Many pore sealing approaches have been explored over the last two decades. As mentioned in Chapter 1, the challenges in low-k pore sealing are to form a dense sealing layer with very limited thickness (less than 3 nm in total including damage layer, sealing layer and sealant diffusion layer[15]). The processing conditions have to be optimized to avoid precursor or plasma diffusion into bulk low-k, while on the other hand ensure the high density of sealing layer on the surface. The pore sealing solutions evolve together with the evolution of low-k material. In this work, methods reported for low-k pore sealing are categorized into three types: plasma densification, inorganic sealants and organic sealants.[16][17]

2.1.1 Pore sealing with plasma induced densification

Reactive ion etching (RIE) by plasma has been applied to dielectric material during patterning (etching, stripping, ashing and cleaning). There are three major species in plasma: ions, radicals and ultraviolet (UV) photons. The porous low-k material is susceptible to plasma induced damage: the organic carbon-containing groups can be removed by radicals and photons and the top surface can be densified by ion-bombardment. Many papers have been devoted to the study of low-k damage during plasma treatments.[18][19] At the early generation of microporous low-k, plasma densification is a convenient way to modify the pores on the top few tens of nanometers and create a densified layer to stop barrier diffusion. The concept of pore sealing with plasma is to expose low-k film to plasma (after etching and cleaning but before metal barrier deposition). The plasma species will cause pore wall collapse and densification. The target is to form conformal and continuous sealing layer on top of the pores while avoiding damages to the bulk. This is done by careful selection of plasma chemistry, smart design of plasma chamber and optimization of plasma treatment conditions (power, bias, time, pressure, temperature). Nitrogen contained plasmas (NH_3 or N_2+H_2) are generally preferred for pore sealing purpose. Possibly because chemisorption of NH_x radicals result in Si-N and C-N bonding which leads to bridging of the opening of the pores.[20]
The dissertation of Goethals [21] gives a literature review of pore sealing solutions by year 2012. Plasmas of interest include He[22][23][24], N_2[25] and NH_3[26][27][28][29]. Oxygen plasma is mainly used to benchmark other plasmas and in most researches it is found to be too deteriorating. Similar to oxygen plasma, Whelan et al.[30] applied ultraviolet ozone (UVO) treatment to low-k and reported sealing on <1 nm pore size low-k. Aimadeddine et al.[27] compared CO/O_2 and NH_3 plasma treatments. They found that oxygen containing plasma deteriorates the electrical properties as well as reliability while RIE by NH_3 plasma enhances the

dielectric reliability. The same author studied CH_4 plasma and reported that CH_4 plasma passivates the side wall and the sealing even outperforms the NH_3 plasma.[31]

Puyrenier et al.[28][32] compared several different plasma treatment conditions and evaluated the sealing using various techniques. They concluded that He and NH_3/N_2 have no sealing effect while NH_3 plasma seals the pores.

Posseme et al.[29] investigated the sealing efficiency of reducing and oxidizing ash chemistries. He found that RIE by NH_3 plasma is efficient to prevent metallic precursor diffusion. They also found that even for the plasma that seals according to Rutherford Backscattering Spectrometry (RBS) and resistance-capacitance (RC) tests, solvents could still diffuse into the pores. The porosity of plasma treated sample is closed to that of pristine samples.

Urbanowicz et al. [33] reported that exposing low-k (with pore radius around 0.9 nm) to a sequential treatment of He and NH_3 could seal the pores. Braginsky et al. [24] furthered this idea and reported that He plasma pretreatment could protect the film from subsequent exposure to oxygen or hydrogen atoms generated from downstream plasma. The sealing mechanism is also discussed in his work.

A similar finding was made by Shoeb and Kushner [20] that a 2 step treatment of low-k by He and NH_3 plasmas could seal the surface without bulk damage. However, pores in excess of 1 nm in radius are difficult to seal due to the inability of N-bonding to bridge the pore opening. Figure 2.1 shows the influence of the pore radius on the sealing efficiency of the top surface and sidewalls of patterned low-k films. It can be seen that the pore sealing efficiency decreases with increasing pore sizes and that the side walls are even more challenging to seal. Therefore, plasma sealing is only relevant for microporous films. Since the low-k materials with lower dielectric constant will inevitably have a higher porosity, a larger pore size and a higher degree of the pore interconnectivity, a deeper penetration of

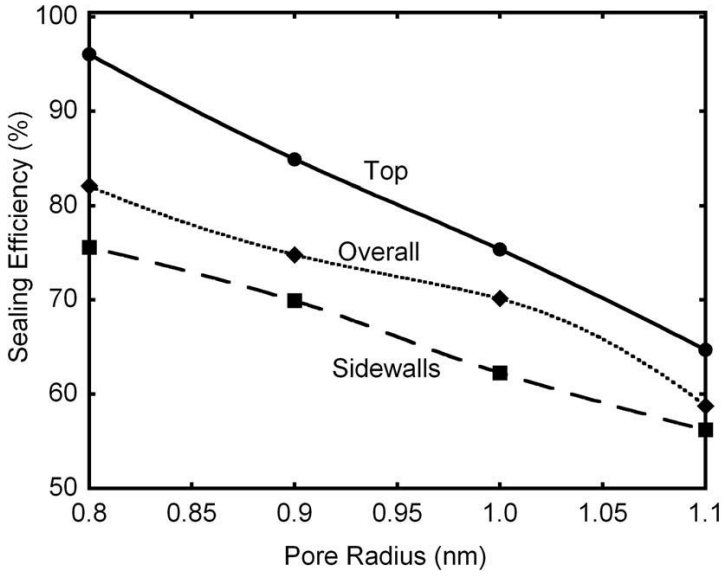

Figure 2.1: Sealing efficiency (the fraction of pores that were initially open to the plasma and are sealed after plasma) as a function of pore radius. Sealing efficiency decreases with increasing pore radius as the N-N bonding has a limited extent.[20]

the active plasma species into the bulk low-k material is expected on ultra low-k. Therefore plasma pore sealing is not applicable for low-k with larger pore sizes. That is probably the reason why the number of publications in this field decreased after 2011.

The other limitations of plasma etching include the thickness loss, k-value increase, moisture uptake and bad sealing performance on sidewalls due to anisotropic modification. The plasmas also break Si-CH_3 bonds and turning the top part of SiCOH low-k film into a SiO_2-like material. This top part chemically modified by plasma is called "damage layer". As mentioned in Section 1.4 Figure 1.8, the plasma induces damages and deteriorates low-k.

2.1.2 Pore sealing with inorganics

Pore sealing with silicon-based inorganics is one of the first solutions investigated. The major challenge of this approach comes from the deposition techniques: physical vapour deposition (PVD) layers are not considered due to poor conformality. Atomic layer deposition (ALD) layers would diffuse before a conformal sealing film is formed. Plasma enhanced atomic layer deposition (PEALD) might be damaging for low-k material. Chemical vapor deposition (CVD) would also have the problem of forming a conformal film. In all cases, to seal the low-k with a pore radius of r nm, a sealing layer with a minimum thickness of $t > r$ nm is normally required. In the PhD thesis of Iacopi [34], she reviewed the possibility of sealing low-k with PECVD SiC and she found that thicker SiC is needed to form pin-hole free barriers.

Mourier et al. deposited SiO_2 on low-k (pore size of 3.4 nm) by PECVD as sealing layer. They found that 5 nm film already shows sealing. They observed that an improvement of leakage current and capacitance with an order of magnitude is achieved by applying pore sealing process.[12]

Bonitz et al. investigated how the pore size influences the barrier integrity and found that on 3 nm pores, the CVD SiO_2 improves slightly the barrier integrity while on 7 nm pores, the SiO_2 has no effect on barrier integrity.[35]

Chen et al. deposited a SiC layer with PVD Ta(N) in 0.13 μm single damascene structure. They found that the addon layer reduces the surface roughness from 1.5 nm to 0.4 nm. By using this addon layer, the thickness of the barrier can be reduced from 12 nm to 5 nm, lowering the contribution to total metal line resistance from barrier layer.[36][37]

De Rouffignac et al. from the group of Gordon deposited first a sub-nanometer aluminum catalyst, then a 4 nm silica by ALD and found that it could seal the 5.5 nm pores against 1.5 nm thick WN. The stack of low-k/silica/WN/Co/Cu shows good electrical and adhesion properties. The 4 nm of silica thickness exceeds the pore radius (2.75 nm), therefore, it can

seal the pores.[38]
Jousseaume et al. deposited SiC by PECVD and compared the sealing performance of SiC with SiO_2. They found that a minimum of 7.5 nm sealing layer is needed to seal the pores with a size of 3.4 nm.[39]
Jiang et al. deposited silica by PEALD with a concept that sealing material can be spatially defined by the supply of plasma irradiation. But the initial pore size of low-k in the experiment is already small (2nm).[40]
Ahearn et al. deposited CVD BCN film and tested the sealing against CVD Ta compounds. They found that a minimum of 3.9 nm BCN is needed to seal the 1.9 nm pore size low-k and BCN penetrates into low-k until the pore openings are pinched off as the sealing film deposits.[41]
More recently, Ishikawa and Kimura et al. deposited PEALD SiN film on top of low-k 2.0 after UV restoration. The UV restoration is meant to repair the low-k damage after plasma etching during patterning. They tested the sealing against a certain wet chemistry (not specified in the paper) and TiN precursor. They claimed that 1 nm SiN is sufficient to seal the 3.3 nm pores. Sealing is achieved by combining UV restoration and SiN layer.[42][43]
We summarize the researches on pore sealing with add-on layer in Table 2.1. The sealing option with inorganics has difficulty in sealing the 3 nm pore size low-k with limited thickness. The k value of dielectrics is normally higher than 4 (Table 1.1) and the thickness of sealing layer should be controlled to be less than 1 nm (Figure 1.8). This is quite challenging because the sealing layer thickness should be larger than pore radius in order to pinch off the open pores.

2.1.3 Pore sealing with organics

The research group of Lu et al. investigated the sealing behavior of parylene. They first deposited a parylene polymer film by CVD and claimed that it seals the pores. The mechanism is that the free radical polymerization characterized with a high growth rate after original initiation avoids in-

pore penetration. The selectivity on dielectric over metal is also high. [44] Then they continued this research by depositing the same material on larger pores and testing the sealing against sputtered Ta and Ru. They found that the polymer/Ta stack passed bias temperature stress test while polymer/Ru stack failed. [45] Afterwards they showed sealing with 1 nm parylene against Co and reported a thermal stability of the polymer film up to 400 °C. The possibility to integrate this process and the adhesion of the film is not reported, though.[46]

Goethals et al. spin-coated a self-assembled carbon-bridged organosilica layer followed by a grafting with hexamethyl disilazane. They observed sealing with 3 nm PMO against TaN or TiO_2 and the k value increase caused by the deposition of PMO is only 0.07. However, the sealing on a patterned structure is not shown.[21][47][48][47]

Zhou et al. deposited a carbosiloxane by molecule layer deposition with a target for pore sealing. The film exhibit good chemical and thermal stability. However, the sealing efficiency of this film was not mentioned.[49]

Chung et al. deposited (3-aminopropyl)trimethoxysilane (APTMS) and 3-mercaptopropionic acid between SiO_2 and Cu. They found that both the electrical properties and adhesion are improved. However, the test was not performed on porous material.[50]

Dictus et al. tried to seal low-k with PECVD polymers formed in plasma containing nitrogen and carbon. The polymer layer can act as promoting layer for electroless deposition. But the plasma employed might potentially damage low-k. And the adhesion to metals is not shown.[51]

Kayaba et al. spin coated a polymer film on low-k for a copper dual damascene structure. They first deposited the polymer and then selectively removed it from Cu surface by baking. They claimed the pores are sealed with 2.5 nm polymer film. [52]

Table 2.1 summarized the publications on sealing with add-on layer. From this table, one can see that it is challenging to seal low-k with pore size larger than 3 nm while limiting the sealing layer thickness. There is a trend

of sealing with organic layers instead of inorganic layers.
Whelan et al. was the first who proposed to use self-assembled monolayer (SAM) as Cu diffusion barrier[30]. Caro et al. tested the concept on a SiO_2/Cu structure.[53] Armini et al. deposited CNSAM on plasma and wet pretreated surfaces and compared the sealing efficiency. After that, the same research group deposited SAM by CVD and showed sealing against 3 nm MnN.[54][55] The promising results from those works invite us to explore further the possibility of sealing the low-k material with SAM.

Table 2.1: Summary of publications on low-k pore sealing with add-on layer

Material	Pore size nm	Sealing layer thickness, nm	Year	Reference
PECVD SiC:H	4-5	25	2002	Iacopi, F.[56]
PECVD SiO_2	3.4	5	2003	Mourier, T.[12]
CVD SiO_2	3 and 7	20	2004	Bonitz, J.[35]
SiO_2 by Al catalyzed ALD	5.5	4	2004	de Rouffignac, P.[38]
CVD Parylene	1.5	2.7	2004	Jezewski, C.[44]
PECVD SiC(N)	8.2	10	2005	Chen, X. T.[57]
PECVD SiC and SiO_2	3.4	7.5	2005	Jousseaume, V.[39]
PEALD SiO_2	2	5	2006	Jiang, Y.B.[40]
CVD Parylene	4	5	2006	Juneja, J.S.[45]
ALD SSQ	3	5	2007	Jiang, Y.B.[58]
CVD BCN	1.9	3.9	2007	Ahearn, W. J.[41]
CVD Parylene	3-4	1	2008	Ou, Y.[46]
Spin-on PMO	3	20	2012	Goethals, F.[21]
PEALD SiN	3.3	1-5	2012	Kimura, Y.[42]
PEALD SiN	3.3	1	2013	Ishikawa, D.[43]
Spin-on polymer	3	2.5	2014	Kayaba, Y.[52]

2.2 Pore sealing with self-assembled monolayers (SAM)

2.2.1 Introduction of SAM

After comparing the possible solutions for low-k pore sealing, SAM is identified as a promising one. A self-assembled monolayer (SAM) is a single organized layer of molecules that spontaneously align on a substrate due to intermolecular interactions and affinity between the molecular head-group and the substrate material.[59] The structure of these formations is influenced by Van der Waals forces, hydrogen bonding, and dipole-dipole interactions, each of which depends on the shape, length, functional group, and dipole moment of the assembling species. SAMs have been demonstrated on a variety of substrate materials, including metals and various oxides. There are three key parts of a self-assembling molecule (Figure 2.2). The head group is the functional group that binds to the substrate. In the case of noble metal substrates, this is typically an amine or thiol, while phosphonic acid and siloxane are popular choices for metal oxides. The backbone is the generic name given to everything between the head group and termination. Backbones can range from simple alkanes and paraphenyls to more complex structures such as naphthalene, "cage" molecules such as carboranethiols, and even large, bulky species such as porphyrins. The termination, or functional group, of the molecule is the end facing away from the substrate. This group is sometimes chosen to have some chemical functionality for the purpose of binding another molecule to the surface. Other common terminal groups are methyls, chosen for their hydrophobicity, and hydroxyls, chosen for their chemical functionality or hydrophilicity. Thiols and amines are chosen because they are symmetric with the head group. Depending on the application, the tail groups should have high affinity/reactivity with the next layer of material.
Two different reaction mechanism, hydrolysis followed by condensation or

only condensation can happen.[60] Figure 2.2 shows an example of how organosilane precursors can be attached to dielectrics by hydrolysis. Since the low-k material are generally terminated with CH_3 groups and therefore hydrophobic, a pretreatment step is needed in order to introduce activation sites onto low-k. The SAMs pore sealing strategy consists of three steps: i) pretreatment of the low-k surface in order to introduce hydroxyl groups indispensable for the silanization reaction;[61] ii) deposition of a dense molecular film to seal the low-k surface against the subsequent barrier precursor; iii) formation of a thin metal barrier to avoid the penetration of moisture and copper ions into the dielectric.

As explained in the last chapter (Section 1.4), it is important to limit the thickness of sealing layer. The thickness of SAMs layer is determined by the thickness of the film with activation sites.(Further explained in Chapter 4) Therefore, ideally a surface confined pretreatment which would make only the top few nm of low-k hydrophilic is needed.

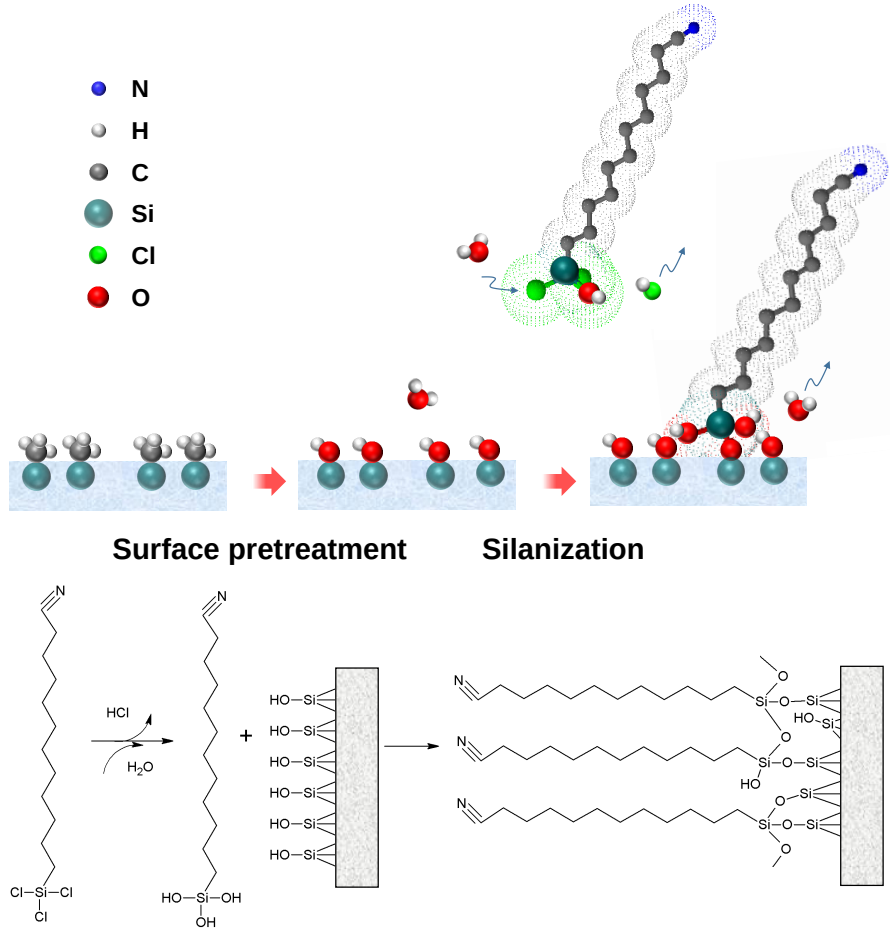

Figure 2.2: Schematic drawing of CNSAM chemisorption on SiO_2 surface.

2.2.2 Surface-confined pretreatment to enable SAM and state-of-the-art

The low surface energy of low-k makes it difficult to deposit selective layer from SAM or ALD precursors.[62][63][64][65][66][67][68] Most of the selective layers deposited chemically from ALD or SAM precursors need activation of the low-k film by a certain treatment which would generate

sufficient hydroxyl groups on, and limited to the surface.
In previous works from our group, successful sealing with SAM against Tetrakis(ethylmethylamino)hafnium (TEMAH) ALD precursor has been demonstrated.[67][55] However, it has also been discovered that when the pore diameter of the etched low-k material is higher than the characteristic dimension of the SAM molecule, diffusion of SAMs into the pores is driven by the reaction between the silane precursors and the silanol groups, generated by the scission of $SiCH_3$ bonds by plasma species during etching (Chapter 4). In this case, the SAMs distribution follows the in-depth profile of the silanol groups in the pores. The deposition of SAMs in the pore causes an additional increase in k-value which correlates directly with the penetration depth of SAMs.[69]
In the field of surface-confined treatment of porous materials, only limited number of works have been reported, including the activation of low-k with wet chemistry, UV/O_3, diffusive or aggressive plasmas.[70][71] Two PhD thesis reviewed the plasma damage of organosilicate glass (OSG) low-k films but they are focusing on the ashing and etching of low-k with less damage.[72][73] The surface-confined pretreatments with the purpose to enable deposition of SAM and ALD precursors have not been studied systematically.

2.3 Objectives and outline of the dissertation

This work is part of a global effort to understand and tackle one of the biggest challenges in low-k integration: the barrier diffusion problem. Sealing the meso-porous material with pore size as big as 3 nm while keeping the deeper layer untouched can be a difficult task. In such conditions, most of the traditional thin film deposition protocols (CVD, PVD and ALD) encounter the obstacle of precursor diffusion. The original research work reported in this dissertation is focused on the

characterization and metrology of surface-confined SAM deposition, which is made possible by surface-confined low-k activation. The major objectives of this thesis can be summarized as follows:

- Study on the feasibility of low-k pore sealing with SAM. Develop a stable and repeatable protocol to activate low-k material and to deposit SAM
- Identify the influencing factors and proper conditions of low-k activation for surface-confined SAM deposition
- Generate fundamental understanding of the interactions between pretreatment species (including wet chemistries, plasmas and silicon) and low-k material

Figure 2.3 shows the structure of this dissertation.

Chapter 3 introduces the methodologies used in this work, including film

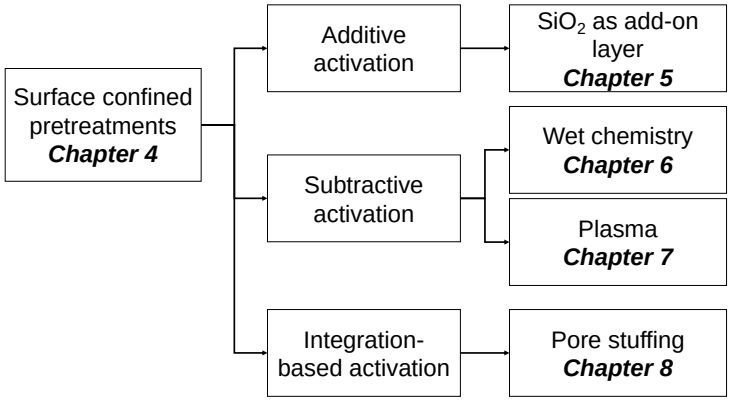

Figure 2.3: Structure of this dissertation

deposition, surface pretreatments, material selection and characterization. In Chapter 4, the influence of plasma induced damage (PID) and pore size

on SAMs sealing and indiffusion is discussed. Surface-confined activation is identified as the crucial factor to limit SAMs diffusion.

Chapter 5-8 is devoted to comparing 4 different pretreatment approaches, each pretreatment is tested by SAMs deposition in order to examine the effectiveness of the specific pretreatment. Chapter 5 is focused on the surface activation with silicon evaporated film. Chapter 6 and 7 describes the subtractive surface activation methods including wet treatment with solutions and dry treatments with plasmas. Chapter 8 introduces the surface activation with pores protector. Finally, Chapter 9 provides a general comparison of the four surface-confined activation methods investigated and the general conclusions of the work, followed by the suggestions on the possible future research.

Chapter 3

Methodology

In this chapter, I briefly describe the most important processing and characterization techniques that were used in this thesis. The first part is devoted to how low-k is prepared. The second part explains the methods of surface activation. The third part focuses on the precursor and solvent selection and the deposition of SAM. Finally we introduce the characterization techniques, including water contact angle (WCA), Fourier transform infrared spectroscopy (FTIR) and equivalent damage layer thickness calculation, spectroscopic ellipsometry (SE) and ellipsometric porosimetry (EP), Rutherford back-scattering spectrometry (RBS) and k value measurement. Only the techniques which are used in a special way in this work are introduced in this Chapter. Details of other techniques and procedures carried out with routine procedure can be found in Appendix B.

3.1 Low-k dielectrics preparation

PECVD low-k film —The porous organo-silicate glass (p-OSG) were deposited on 300 mm Si substrates by plasma-enhanced chemical vapor deposition (PECVD) from alkylsilane precursors followed by UV-assisted thermal curing. [74][9] The low-k films had an initial thickness of approximately 90 nm, a dielectric constant of approximately 2.0, 47% of porosity, with an average pore diameter of 3.4 nm and a water contact angle of 96°. Further details are described in the literature.[18]

Spin-on low-k —Low-k films were deposited from a sol of organosilica precursors and polyethylene oxide containing non-ionic surfactant. The sol was spin-coated on top of 300 mm Si wafers with 1 nm of thermally grown SiO_2. The oxide films were subjected to a 2 minutes soft bake at 150 °C and then hard-baked for 2 hours at 400 °C in N_2 atmosphere. Properties of this material is listed in Table 3.1.

The untreated, as-deposited low-k is referred to as "pristine".

Table 3.1: Properties of low-k material used in this work

	PECVD low-k	Spin-on low-k
Thickness, nm	90	200
k value	2.00	2.26
Porosity, %	47	40
Pore radius, nm	1.7	1.4

3.2 Low-k surface-confined pretreatment

3.2.1 Silicon evaporation and oxidation

Low-k samples are cleaved into 3×3 cm^2 pieces and attached to a carrier wafer for evaporation. Figure 3.1 shows the setup of Si evaporation: samples are fixed to a 200 mm Si carrier wafer and placed upside down in the evaporation chamber from Alcatel. Pure silicon is in a boat-shape container hanging underneath the carrier wafer. The chamber pressure is maintained around 1×10^{-6} mbar (10^{-4} Pa). The temperature of the chuck in the Alcatel evaporation tools is not controlled and it is estimated to be around 80 °C. The temperature of the boat is the evaporation temperature of the material, in this case Si (melting point of 1414 °C). From that point on, the higher the temperature is increased, the higher the rate. The evaporation is controlled by a deposition controller. Quartz crystals are used to measure deposition rates. The quartz crystal mechanically oscillates when alternating current voltage is applied to it. The resonance frequency of oscillations is dependent on the mass of the film deposited onto it. The Si thickness after each run is further confirmed by removing part of evaporated silicon from the carrier wafer and measuring the stage height with a profilometer (This thickness is referred to as ***""nominal Si thickness""*** or $\boldsymbol{d_N}$). Caution must be taken that nominal thickness could be very different from the Si thickness which is deposited onto low-k and it is only meant to identify samples. After silicon evaporation, the samples are annealed in an oven with flowing O_2 under 250 °C for 30 minutes to convert Si to SiO_2.

3.2.2 Wet pretreatments

HF pretreatment: samples are immersed in 0.5% (v/v) HF solution for 1 to 5 minutes. Sulfuric peroxide mixture (SPM) pretreatment: Samples

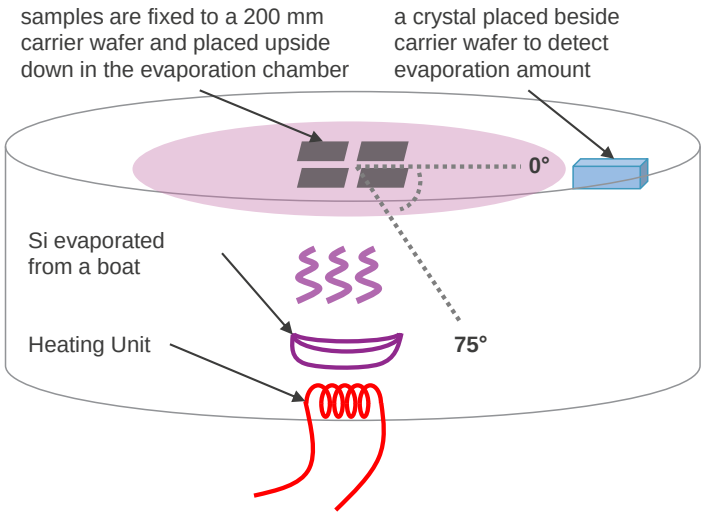

Figure 3.1: Schematic drawing of Si evaporation chamber setup.

are immersed in a 1:4 piranha solution (v:v, H_2SO_4:H_2O_2) at temperatures ranging from 20 °C to 100 °C for 2 to 15 minutes. Tetramethylammonium hydroxide (TMAH) pretreatment: Samples are immersed in a 10 to 20% wt. TMAH solution at 50 to 70 °C for 30 to 120 s. Following all pretreatments, samples are sonicated in water for 2 minutes, rinsed with copious amount of flowing water and blow dried with N_2.

3.2.3 Plasma pretreatments

H_2/Ar plasma —The wafer is processed for 20 s with H_2/Ar plasma ignited at 350 °C under 200 W in EmerALD capacitively coupled plasma (CCP) 300 mm single wafer system with H_2 partial pressure of 0.89.
CF_4 plasma —The wafer is etched for 6 s with CF_4 plasma in a capacitively coupled plasma (CCP) chamber.
CO_2 plasma —The plasma treatment is done in a commercial Capacitive-Coupled Reactive Ion Etching (CCP-RIE) chamber with a dual-frequency

source (13.6 MHz and 40 MHz) coupled to the bottom electrode. Unless otherwise noted, the plasma is ignited and maintained at a chamber pressure of 100 mTorr for 3 s by applying 100W from high-frequency source (40MHz).[75]

3.2.4 Pore stuffing

Frot et al. patented a method to address the problem of low-k degradation during plasma etching.[76][77] The concept is to fill the pores with a sacrificial polymer so that the porous material is temporarily converted into a dense material. They name this process as the "post porosity plasma protection" (P4). In later works of Zhang et al., it is called pore stuffing approach (referred to as "PS" in this chapter).[78]. PMMA is selected as the pore stuffing chemistry because it decomposes thermally without leaving residues behind (no C=C sp2 formation)[79]. The pore stuffing process consists of (i) densification of the porous low-k film by wet stuffing with the sacrificial polymer filling agent (PMMA, Mw 2500 g/mol from Sigma Aldrich); (ii) CF_4 plasma etch; and (iii) a thermal burnout process at 450 °C for 15 minutes in N_2 ambient to remove the PMMA. It has been observed that the plasma-induced Si-CH_3 depletion is significantly reduced via pore stuffing and that the silanol groups can be confined to the top surface of the porous film.[79] Afterwards, a wet cleaning procedure is applied to all samples in order to remove the post-etch polymer residues and to make the surface more hydrophilic (Detailed in Appendix B). The properties of the treated low-k films are presented in Table 8.2.

3.3 Precursor selection and deposition of SAM

3.3.1 Precursor selection

11-cyanoundecyltrichlorosilane (CNSAM) has been reported as a promising candidate to enable ALD of metal barriers.[80] That is why it is the first precursor studied for pore sealing. The cyano terminal groups can be easily converted into reactive carboxylic functionalities[81][82], which have been reported to be promising candidates as copper diffusion barriers.[83] In addition, the unshared electron pair of the cyano group allows for an increased reactivity towards molecular layer deposition.[84] Cyano-terminated SAMs increase the surface energy of the low-k materials as compared with the originally hydrophobic -CH_3 functionality, improving the adhesion between the dielectric and the metal barrier.[64][85]
However, after several experiments, the ellipsometry porosimetry (EP) measurements indicate that CNSAM could not seal the pores. Even when a large amount of SAM is deposited and the diffusion layer is as thick as more than 10 nm, the EP curves show no sealing. CNSAM precursor is deposited in Chapter 4 and Chapter 6 .
Therefore APTMS is selected as a second precursor. It is selected because the amino termination is the same as the functional groups in barrier precursor for the deposition of TiN and MnN. Therefore it can enable subsequent barrier deposition. Hysteresis in EP curves is observed for low-k sealed with APTMS, possibly due to the inter- and intra-molecular hydrogen bonds formed. The sealing of this precursor is better than CNSAM. The k value change is also smaller for this precursor. A comparison of APTMS and CNSAM is included in Chapter 5 and 8.
Although APTMS shows satisfying result, the research performed in Chapter 4 shows that precursors with longer chain length might result in less indiffusion. DETA is a precursor with similar structure while longer chain length. Therefore it is believed to be a better choice than APTMS.

Three amino groups are present in this precursor. Results presented in Chapter 7 shows that this precursor gives nice sealing results. Page *xvii* shows the chemical structures of all the precursors.

3.3.2 SAM deposition

The SAM precursor and analytical-grade toluene solvent are used as supplied by Sigma Aldrich. Wet deposition by dip coating and spin coating is used in this work. Although vapor phase deposition is also interesting and easier to realize for full wafers, wet deposition provides more room of choice for precursors and solvents because some of the SAM precursors can not be vaporized. The temperature and pressure profile in the vapor deposition chamber might cause variance in film homogeneity. Therefore we believe wet deposition is more suitable for fundamental studies.

SAMs dip coating —SAMs are deposited by immersing the pretreated samples in a solution of 5 mM precursor in toluene for various time. The deposition is carried out in a water tank with parafilm protection placed in atmosphere. After deposition, the samples are sequentially sonicated for 2 min in the same solvent and then ethanol, dried under nitrogen stream, and annealed at 120 °C for 15 min in N_2 atmosphere. The results in Chapter 4, 5, 6, 8 are obtained by SAM dip coating.

SAMs spin coating —Immediately before the SAM deposition, the sample is annealed under N_2 atmosphere at 150 °C to remove physically absorbed water. SAMs are spin coated onto the low-k film from a precursor solution in propylene glycol monomethyl ether acetate (PGMEA) at 500 revolutions per minute (RPM) on a small spinner under atmosphere. The precursor solution is dispensed from a dropper onto 4-9 cm^2 pieces. The sample is rinsed using the same solvent right after the application of the precursor solution and annealed at 120 °C for 15 min in N_2 in order to remove solvents residual and to allow for chain reordering. The results in

Chapter 7 are obtained by SAM dip coating.

3.3.3 Solvent selection

For dip coating, toluene and methanol are both tested. Toluene contains little amount of water. Dip coating low-k samples in toluene results in water layer formation on the surface of low-k and SAM precursors are driven to the surface by hydrophilic-hydrophobic forces. Therefore the deposition in toluene can result in multilayer formation. Under strictly controlled conditions and limited deposition times (less than 4 hours), though, a monolayer deposition is still possible. Dip coating in methanol can suppress multilayer formation and is therefore preferred for amino- SAM precursors. The deposition in methanol for CN- terminated SAM is not successful though. For spin coating, the deposition time is much shorter than dip coating. A fast kinetics is preferred and certain degree of precursor pre-condensation results in better sealing. PGMEA is selected for spin coating in our work because deposition in other solvents is not successful.

3.4 Nanoscale characterization

3.4.1 Water contact angle (WCA)

If a small droplet of water is dispensed onto a solid surface, it will be surrounded by its vapor and air. The droplet would try to minimize the free energy by either spreading or shrinking till equilibrium. At the line of contact between the liquid and the solid, under thermodynamic equilibrium state, the forces are balanced. Therefore the contact angle could be determined by the Young equations (Equation 3.1. The contact angle θ reflects the similarity in the nature of the contacting phases. Water contact angle is one of the most simple and fast techniques to decide the

wettability of the surface. In this dissertation, it is used to check the surface hydrophilicity after pretreatment (Section 2.2.2). By comparing the WCA after SAM deposition with the reported WCA of that SAM, we can tell whether the deposition of SAM is successful or not.

$$\gamma_{sv} = \gamma_{sl} + \gamma_{lv} \cdot cos\theta \tag{3.1}$$

, where s, v and l denotes the solid, vapor and liquid phase and γ is the surface tension between the phases as indicated in the subscript, θ is the water contact angle (Figure 3.2). In this work, the static WCA of deionized

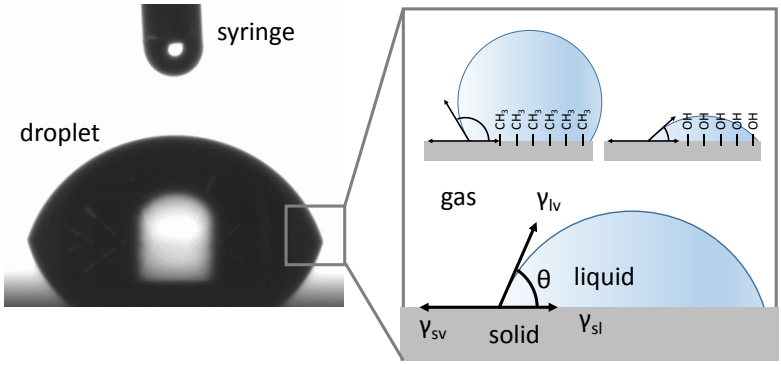

Figure 3.2: Left: picture of a water droplet on a surface. Right: schematic representation of the liquid contact angle θ and the representative interfacial energies

water droplets deposited on the sample surface is measured in the air using a software-controlled Video Contact Angle System. At least 5 droplets of water are measured at distantly located positions on the sample surface and the average is taken as final result.

3.4.2 Fourier transform infrared spectroscopy (FTIR) and equivalent damage layer (EDL) thickness calculation

The chemical bonds in material vibrates with quantized energy states. When the molecules are exposed to electro-magnetic waves, and the energy of the incident light matches with the specific vibration mode of the specific bonds, resonance absorbance occurs. Because $\Delta E = hc_l\bar{v}$ (where E is the energy, h is plank constant, c_l is the speed of light and $\bar{v}$ is the wavenumber), the energy absorbed corresponds to a certain frequency of the light. Therefore, we can deduce the chemical groups in the material by detecting what frequency of IR light is absorbed by thin film.

The abundance of functional groups quantitatively relates to the absorbance of IR light. It is calculated based on Beer's Law: $A = \varepsilon_{absb}lc$, where A is the absorbance, ε_{absb} is molar attenuation coefficient as an intrinsic property of the species, l is the pathlength (film thickness for transmission FTIR) and c is the molar concentration of chemical bonds.

As introduced in Section 2.2.2, the low-k should be pretreated in order to introduce silanol groups indispensable for SAM deposition. After the pretreatment, the -CH_3 groups in low-k are removed from the surface and the surface resembles a SiO_2-like material. The damage is defined as the -CH_3 depletion which is reflected in the reduction of the Si-CH_3 peak intensity around 1275 cm^{-1} in the FTIR spectra. The proposed model for the low-k damage quantification assumes a defined interface between damaged vs. non-damaged film instead of a gradient interface in the real case (Figure 3.3). As one might notice, the damage layer thickness obtained in this model is different than the damage layer thickness in reality, therefore it is called "equivalent damage layer (EDL)" thickness. The details of our calculations are shown in Equation 3.2, where d_{damage} is the equivalent damage layer thickness, d_0 is the thickness of pristine film, d'_0 is the thickness of the pretreated film, $I_{Si\text{-}CH3}$ is the area integration of Si-CH_3 peak of the pristine, $I'_{Si\text{-}CH3}$ is the area integration of Si-CH_3 peak

of the damaged low-k. An example of the FTIR spectra is shown in Figure 3.4.

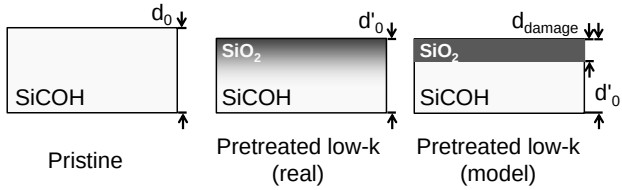

Figure 3.3: Schematic illustration associated with the equivalent damage layer thickness (d_{damage}) calculation model.

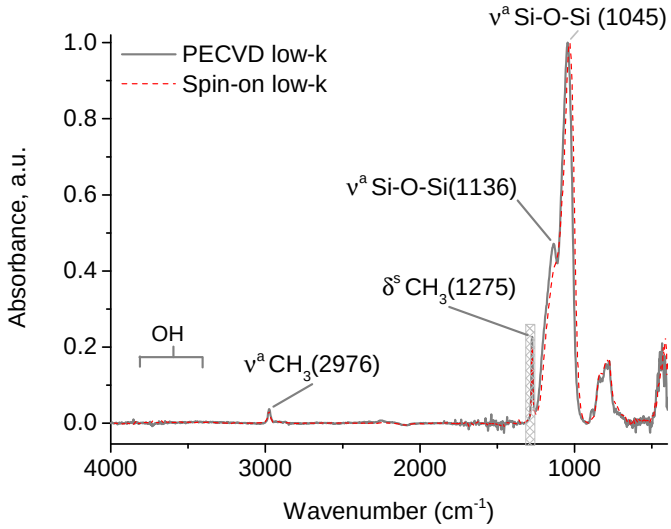

Figure 3.4: An example of the FTIR spectra of low-k material. Grey part denotes the peak area used in the calculation of equivalent damage layer (EDL) thickness

$$d_{\text{damage}} = d'_0 \left(1 - \frac{\left(\frac{I'_{\text{Si-CH3}}}{d'_0} \right)_{\text{damage}}}{\left(\frac{I_{\text{Si-CH3}}}{d_0} \right)_{\text{pristine}}} \right) \tag{3.2}$$

In this work, FTIR measurements are performed in transmission mode using Nicolet 6700 FTIR spectrometer from Thermofisher with a resolution better than 1 cm^{-1}, averaging 100 spectra within the 400-4000 cm^{-1} range. In every measurement performed for the spectra acquisition, the background spectra are subtracted. The spectra of low-k film deposited on silicon substrate are collected. To get the substrate spectra, a piece of sample cleaved from the same wafer is dipped in 50% HF solution for 5 minutes and rinsed with water. Then the FTIR spectra are measured within 10 minutes. The FTIR spectra of low-k film are thus obtained by subtracting the two spectra. Afterwards, the spectra are normalized by the thickness of the low-k film obtained from SE measurements. FTIR peak is assigned according to Grills' paper[86] For samples deposited with SAMs, the FTIR is collected before and after SAM deposition on the same piece. When the measurement on the same piece is not possible, the neighboring piece with distance less than 3 cm is cleaved and used as a reference.

3.4.3 Spectroscopic ellipsometry(SE) and ellipsometric porosimetry (EP)

When a polarized light interacts with dielectrics and gets reflected, the polarization changes and the degree of this change depends on the thickness, density and optical parameters of the thin film or stack. The polarization change in the reflected light is quantified by amplitude ratio (Ψ) and phase difference (Δ). In SE measurements, Ψ and Δ are collected as a function of wavenumbers and a model is built to simulate Ψ and Δ starting from a set of initial values of optical properties and thickness of the film. Eventually, the

thickness and optical parameters (e.g. refractive index (RI)) is deducted from the measured value of Ψ and Δ. In this work, the thickness and RI of the samples are measured by a SENTECH 801 spectroscopic ellipsometer. A model based on the Cauchy approximation is applied to the spectra collected in the wavelength range of 400–800 nm. The model used for SE should be kept as simple as possible. Therefore, depending on the materials to be evaluated, different models are used:

- For the SAM on SiO_2 substrate (as a reference to porous surfaces), a 1 layer Cauchy model with refractive index fixed to 1.46 is used, assuming the RI of SiO_2 and SAM are the same. [87]
- For low-k pristine and plasma treated low-k, a 1 layer Cauchy model with extinction coefficient fixed to 0 is used (Type I in Figure 3.5)
- For the thickness of SAM deposited on low-k, the SE spectra are collected on the same piece before and after SAM deposition. Then two types of models are used. 1). One-layer Cauchy model with thickness and RI values floating. In this case, the RI and thickness before and after SAM deposition are compared (Type I). 2). Two-layer Cauchy model (Type II): After SAM deposition, the thickness of low-k film is less than original because of the diffusion layer. The RI of low-k film is fixed to the same value before SAMs deposition (assuming no penetration into the bulk low-k underneath the diffusion zone). The top layer is the SAM deposited on the surface and the SAM diffused in the top layer of low-k.
- For the thickness of SiO_2 deposited on low-k in Chapter 5, two types of models are used. 1). One-layer Cauchy model with thickness and RI values floating. In this case, the RI and thickness before and after SiO_2 deposition are compared (Type I). 2). Two-layer Cauchy model (Type III): After SiO_2 deposition, the thickness of low-k film is the same as before deposition. The RI of low-k film is left floating

because certain degree of diffusion is expected. The top layer is the SiO_2 deposited on the surface.

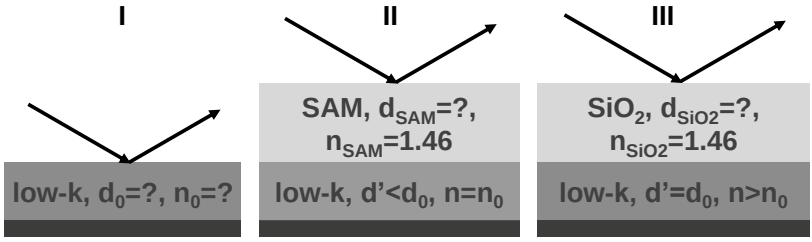

Figure 3.5: SE models used in this thesis: I. One layer Cauchy model; II. Two layer Cauchy model for the stack of SAM/low-k; III. Two layer Cauchy model for the stack of SiO_2/low-k

The relation between the optical constants and properties of a multi component system is described by the Lorentz-Lorenz equation:

$$B_{\text{eff}} = \frac{3}{4\pi} \cdot \frac{{n_{\text{eff}}}^2 - 1}{{n_{\text{eff}}}^2 + 2} \tag{3.3}$$

,where B_{eff} is the effective polarizability of a unit of volume, n_{eff} is the effective refractive index of the multicomponent film. Because the polarizability of a system is a sum up of the polarizability of each components multiplied by its volume fraction, therefore n_{eff} directly correlates with the free volume in the porous film. In this work, we use refractive index measured by SE to estimate the porosity before and after deposition based on Equation 3.3.

Ellipsometric porosimetry is used for measuring porosity and pore size distribution (PSD) of thin porous films. The method is based on the ability of a porous film to adsorb solvent vapor inside the pores. Such adsorption is performed in a vacuum chamber and monitored by ellipsometry. The chamber is firstly pumped down to low vacuum and then slowly filled with toluene vapor (up to the saturated pressure). The toluene adsorption in the porous film is monitored by in-situ ellipsometer. After reaching the

saturated toluene pressure, the chamber is pumped down again to low vacuum while desorption of toluene from the porous film is monitored in situ again. The results of the measurements are dependencies of ellipsometric angles Ψ and Δ on toluene pressure. The pressure is expressed in relative units (P/P_0, where P_0 is the saturated toluene pressure at room temperature) from 0 to 1. The refractive index and thickness of the film are extracted from Ψ and Δ. The refractive index of the film at different toluene pressures is then used to calculate the amount of toluene adsorbed under different pressures. For a perfectly sealed film, Ψ and Δ throughout the adsorption/desorption process should be a constant value. For a partially sealed film, toluene adsorbs at higher pressure and desorbs only partially at lower pressure[88].The free volume (V) and pore radius (R_p) are calculated. The pore size distribution (PSD) is obtained from the desorption by isotherm applying the Barrett-Joyner-Halenda and Dubinin-Radushkevich models within pressure ranges corresponding to mesopores and micropores, respectively.[89] Assuming a monomodal and symmetric PSD, the mean pore radius corresponds to the maximum of the pore radius distribution curve $dV/dR_p = f(R_p)$. This peak value from PSD is interpreted as average pore neck radius. All EP measurements are carried out under conditions when the equilibrium between the gas and adsorption phase has been achieved (steady state regime). [89][90]. If the pores in low-k would be modeled as a cylindrical shape, during adsorption, toluene are then adsorbing to a concave meniscus, therefore the pressure when condensation happen is lower than that below a flat surface (saturated pressure). A hysteresis in Figure 3.6 d can be observed. During desorption, the pores filled with toluene can be considered as hemispherical shape, the mean meniscus radius of hemisphere is smaller than cylinder, therefore the pressure when desorption happen is lower than condensation pressure. As a result of this difference, a typical adsorption-desorption isotherm usually exhibits a hysteresis loop (Figure 3.6). For ultra low-k with large pore size this loop is very small. But when the pores on the surface are partially

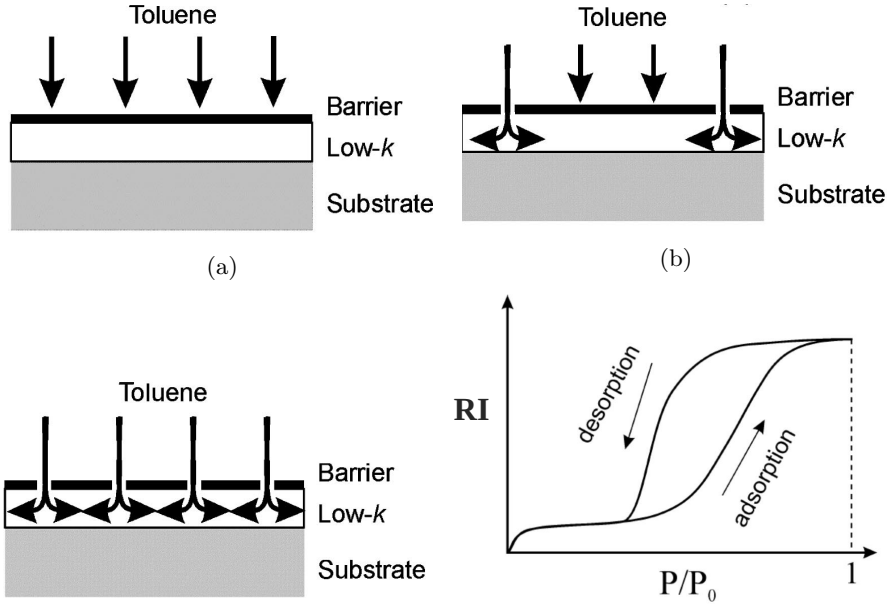

Figure 3.6: Schematic representation of the sealing of low-k in three situations (a) completely sealed, (b) partially sealed and (c) not sealed (d) Adsorption/desorption isotherm in mesoporous solids.[91]

sealed, the pore neck radius reduce and this hysteresis is more obvious. When a serious precursor penetration happens, the pores are fully occupied by the precursor molecules, the RI-P/P_0 curve shows a constant RI through the whole pressure range. Normally in this case the RI is much higher than the pristine film. If pores are bottle-shaped with a neck open to the surface, then pore sizes calculated from desorption measurements reflect neck radii.[92]

3.4.4 Rutherford backscattering spectrometry (RBS)

Rutherford back-scattering spectroscopy (RBS) is an established technique to analyze the composition and elemental depth profile of thin films. A high-energy (MeV) He^{++} ions are directed onto a sample. Because of the Coulomb repulsion with the nuclei in the target, the impinging ions are elastically scattered. The energy distribution and yield of the back-scattered He^{++} ions at a given angle are recorded. The energies of the back-scattered particles depend on the mass of atoms from which they scatter (kinematic factor) as well as the depth at which a collision occurs (energy loss factor). The number of back-scattered ions is directly proportional to the concentration of a given element. Since the likelihood of a backs-catering event is known for all elements (back-scattering cross section), it is possible to derive quantitative depth profiles of a certain element from the RBS spectra for thin films.

In our work, we use RBS to detect the metal distribution in porous film based on the concept of energy-loss straggling, which is the slowing down of the ion accompanied by energy spreading.[93] For long path length of ions, the energy distribution approaches a Gaussian distribution. From the contribution of the energy-loss straggling, the depth of a certain element can be obtained. The yield vs. energy curve collected from RBS measurement is analyzed directly. For a metal film with a well-defined profile, the curve is sharp with a peak corresponding to the metal. When the metal diffuses into the pores of the low-k, a broader peak with a tail extending towards lower energy is observed. The shape of the tail gives an indication of metal distribution profile as a factor of depth (Figure 3.7a).

In order to extract quantitative data from the RBS spectra, a model is built and used to fit the experimental result. The whole stack is divided into three layers: i) the surface metal film ii). the upper half of low-k, and iii). the lower half of low-k. The metal areal density on the surface and in each sub-layer is optimized to best reproduce the experimental spectra.

In this work, RBS measurements are performed using a He^{++} ion beam of 1.523 MeV. The thickness of the layers is deduced from spectra taken with a scattering angle of 170° and a sample tilt of 11°. The amount of penetration of metal atoms into the pores is derived from spectra taken in the glancing exit angle geometry that is optimized for depth resolution. The latter geometry is characterized by a scattering angle of 135° and a sample tilt of 35°, corresponding to a glancing exit angle of 10°.

3.4.5 k value measurement

The k-value is extracted from capacitance measured on a structure formed by evaporating Pt dots in the range from 0.09 to 9 mm^2 on the surface of the sample.(Figure 3.7b) The backside of the samples is first abraded by a diamond pen to remove the native oxide and to create a damaged region, which could act as a diffuse degenerate layer. Then, the damaged area was metalized by applying a gallium–indium (Ga–In) alloy paste.[94] The k value calculation is based on the equation,

$$k = \frac{Cd}{\varepsilon_0 A_{\mathrm{cntct}}} \tag{3.4}$$

Where ε_0 is the permittivity of the free space, A_{cntct} is the area of the deposited circular platinum contact and d is the thickness of the low-k film as measured by SE. C is the measured capacitance in the accumulation region, normally at 100k Hz. It should be mentioned that the accuracy of the k-value calculation depends on the accuracy of the thickness, the metal contact area and the capacitance. The thickness 3σ of low-k measured by ellipsometry on 300 mm wafer is 0.8 nm for 90 nm film. The area error caused by sputtering shadow for a 3 ± 0.09 m^2 is around 6%. This would result in a k value error of 12%. For a low-k film covered with SAM, different SE models (Section 3.4.3) can result in a thickness difference as large as 3 nm. Accordingly, the k value error can be as large as 17%. For our stack

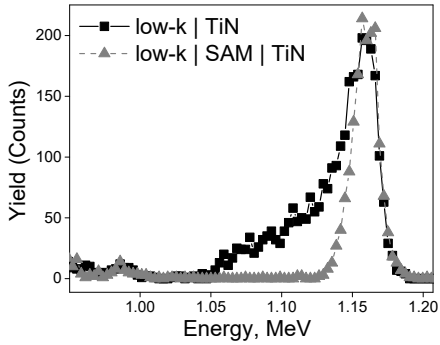

(a)

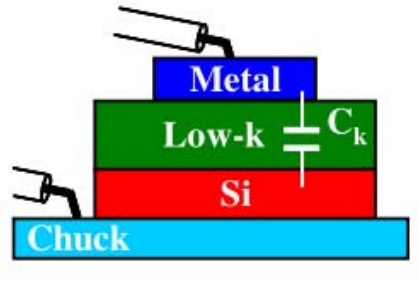

(b)

Figure 3.7: (a)An example of RBS showing TiN ALD on top of a sealed and an unsealed porous low-k dielectric. The Ti RBS peak for the unsealed sample shows a long tail extending to lower energies, indicating the penetration of ALD precursors into the porous network. In contrast, the Ti peak for the sample sealed with SAM is very sharp, proving the confinement of the Ti deposition to the surface region of the porous film.(b) MIS capacitors realized by connecting the Si substrate (bottom electrode) to the metallic chuck of the probe station.

with SAMs and barrier, because of the difficulty finding a good SE model, the highest uncertainty of k value measurement comes from the thickness. The largest capacitance area is used whenever possible to minimize areal error.

Chapter 4

The importance of surface-confined low-k activation

Introduction

In the previous work of our group,[67][55] SAMs were deposited from the liquid and vapor phase on a porous low-k dielectric film activated by Ar/H_2 and Ar/N_2 plasma. Nevertheless, in both cases, despite the successful sealing, the film's dielectric constant increased by 35% and 7% after Ar/N_2 and Ar/H_2 plasma pre-activation followed by CN-SAM deposition. The increase of k value is a consequence of the plasma damage during the pretreatment and resulted diffusion of CN-SAM inside the pores.[55] In order to define specifications for the low-k pretreatment and engineer the organosilane precursors, it is important to have a clear understanding of the critical parameters influencing the plasma damage and SAMs diffusion. In

this chapter, the previously reported Ar/H_2 plasma is replaced with He/H_2 plasma which allows a lower impact from ion bombardment.[33] A shorter plasma exposure time and a higher plasma power are applied to further reduce the damage.[95] Moreover, O_2 plasma in an inductively coupled plasma (ICP) chamber is also investigated as a commonly used etching and striping plasma in order to understand the plasma damage and SAMs diffusion mechanism. Diffusion of CNSAM into low-k with different pore radii and hydrophilic layer thicknesses is investigated. A systematic study on how pore size, curvature and hydrophilicity influence the distribution of SAMs inside the pores would not only be important for the low-k sealing strategy, but also beneficial for several multi-disciplinary fields of interest in functionalized porous materials.

The results presented in this Chapter are based on the following publication: Sun, Y.; Krishtab, M.; Struyf, H.; Verdonck, P.; De Feyter, S.; Baklanov, M. R.; Armini, S. Langmuir 2014, 30 (13), 3832–3844.

This part of work was performed at imec with support from Nano Interconnect program. The task definition, material preparation, plasma treatment and EP measurements were performed by Mikhail Krishtab. Mikhail Baklanov made contribution to the understanding of the mechanism of plasma damage. I developed the SAM deposition protocol, characterized the samples, analyzed the data with guidance from coauthors. I submitted this work to Langmuir, where it was accepted for publication.

Experiment

Three types of porous low-k dielectrics were deposited on Si substrates by plasma enhanced chemical vapor deposition (PECVD) from alkyl silane precursors followed by UV assisted thermal curing.[74][9] The films had

a thickness of approximately 100 nm and dielectric constants of 2.0, 2.5 and 3.0. They are labeled in this chapter as lowk-2.0, lowk-2.5 and lowk-3.0, respectively. The as-deposited films (referred to as ""pristine"") have different pore sizes and porosities (summarized in Table 4.1). Due to the intrinsic hydrophobicity of the pristine dielectric, the low-k surfaces had to be pretreated in order to allow silanization.[61] To this purpose, the low-k films were exposed to O_2 plasma for 20 s in an ICP chamber[96] or to He/H_2 plasma in a capacitively coupled plasma (CCP) chamber. The CCP treatment was performed in an Eagle 12 plasma chamber from ASM, using a radio frequency (RF) of 13.56 MHz and a power of 900 W. The effect of the ion bombardment was minimized by positioning the wafer on a grounded electrode. The wafer was processed at 350 °C for 2 s. The gas flow was 180 sccm for hydrogen and 820 sccm for helium, with a total pressure of 530 Pa. The He/H_2 plasma-treated samples were aged in atmosphere conditions (25 °C, $RH = 34\%$) for a minimum of 30 days for further oxidization. SiO_2 pretreated with UV-Ozone were used as a non-porous reference which experienced the same silanization procedure as the low-k samples. After pretreatment, the samples were cleaved into 3×3 cm^2 coupons. CN-SAM are deposited by dip coating (Section 3.3). Ellipsometry measurements revealed a CN-SAM film thickness of 1.7 nm on SiO_2 which is in agreement with the calculated thickness of 1.6 nm.[97]

4.1 Results of plasma induced damage (PID)

The calculation of the equivalent damage layer thickness is introduced in Chapter 3.4.2. The equivalent damage layer thickness calculated is provided in Table 4.1.

Figure 4.1,4.2,4.3 shows the FTIR spectra of the low-k films as pristine and after plasma processing (O_2 or He/H_2 plasma). The FTIR peaks designation is mentioned in the work of Grill et al.[86] After the He/H_2

Table 4.1: Summary of the refractive index, porosity and pore neck radius before and after SAMs deposition.

Sample	**Damage Layer thickness,nm**	**Bulk Refractive Index**		**Porosity,%**		**Pore Neck Radius,nm**	
	Before SAMs	Before SAMs	After SAMs	Before SAMs	After SAMs	Before SAMs	After SAMs
lowk-2.0							
Pristine	0	1.240±0.002	1.248±0.002	44±2	42±2	1.7	1.7
lowk-2.0 He/H_2	27	1.272±0.002	1.323±0.002	36±2	28±2	1.7	1.4
lowk-2.0 O_2	87	1.303±0.002	1.463±0.002	31±2	1±2	0.8	< 0.5
lowk-2.5							
Pristine	0	1.372±0.002	1.381±0.002	14±2	14±2	0.7	0.8
lowk-2.5 He/H_2	21	1.376±0.002	1.376±0.002	14±2	14±2	0.7	< 0.5
lowk-2.5 O_2	74	1.410±0.002	1.408±0.002	15±2	16±2	< 0.5	< 0.5
lowk-3.0							
Pristine	0	1.440±0.002	1.440±0.002	< 5	< 5	< 0.5	< 0.5
lowk-3.0 He/H_2	18	1.442±0.002	1.442±0.002	< 5	< 5	< 0.5	< 0.5
lowk-3.0 O_2	23	1.448±0.002	1.448±0.002	< 5	< 5	< 0.5	< 0.5

Note: In case of micropores, the toluene adsorption/desorption is diffusion-limited and size quantification of pores having radii below 0.5 nm is not possible with the same approach.[90]

plasma treatment, an increase in the O-H and Si-H peak intensity is accompanied by a decrease in the Si-$(CH_3)_x$ peak intensity. This is an evidence that the plasma is breaking the Si-CH_3 and Si-O-Si bonds, which are converted into Si-O and Si-H bonds.[98] The reaction mechanism between H_2 plasma and the low-k is described as below [19]

$$\equiv\mathrm{Si}-\mathrm{CH_3} + 2\,\mathrm{H} \longrightarrow \equiv\mathrm{Si}-\mathrm{H} + \mathrm{CH_4}\uparrow \tag{4.1}$$

$$\equiv\mathrm{Si}-\mathrm{O}-\mathrm{Si}\equiv + 2\,\mathrm{H} \longrightarrow \mathrm{Si}-\mathrm{H} + \mathrm{Si}-\mathrm{OH} \tag{4.2}$$

At the same time, Si-C bonds also get scissored by vacuum ultraviolet (VUV) as shown below[95]

$$O_xSiCH_3 + h\nu \longrightarrow (O_xSiCH_3)\cdot \longrightarrow SiO_x + CH_3 \tag{4.3}$$

When the samples are exposed to the atmosphere, the Si-H bonds are

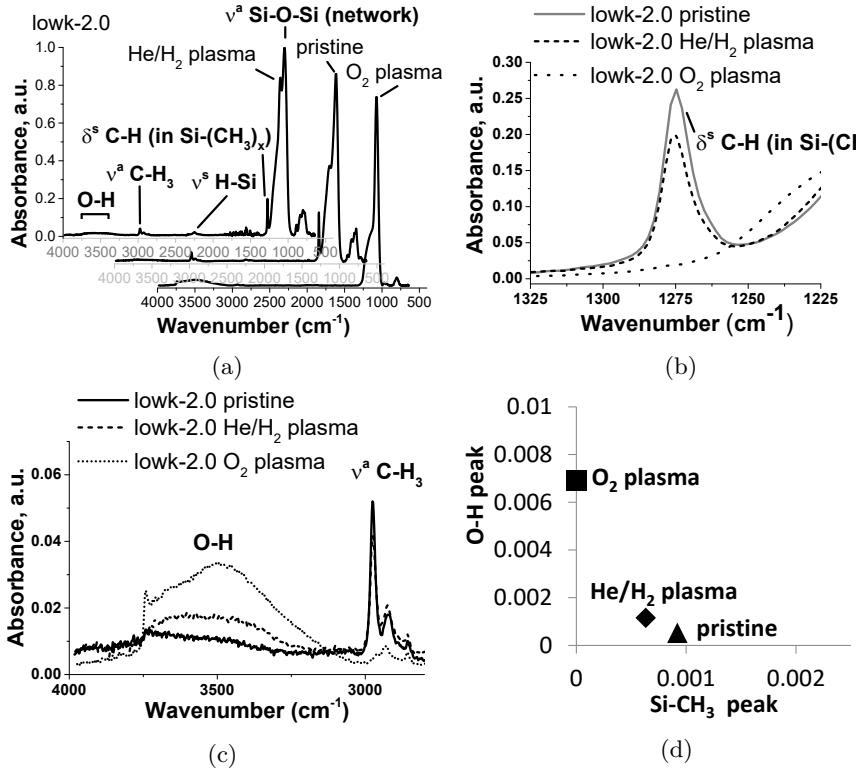

Figure 4.1: (a) Normalized FTIR spectra of lowk-2.0 before and after plasma pretreatment; (b) Zoom-in of the Si-$(CH_3)_x$ stretching and bending peaks; (c) Zoom-in of the O-H and C-H stretching peaks; (d) Integrated O-H peak area vs. Si-CH_3 peak area.

further oxidized to Si-OH bonds. This is manifested by a decrease in the Si-H stretching peak intensity in the range 2100-2300 cm^{-1} accompanied

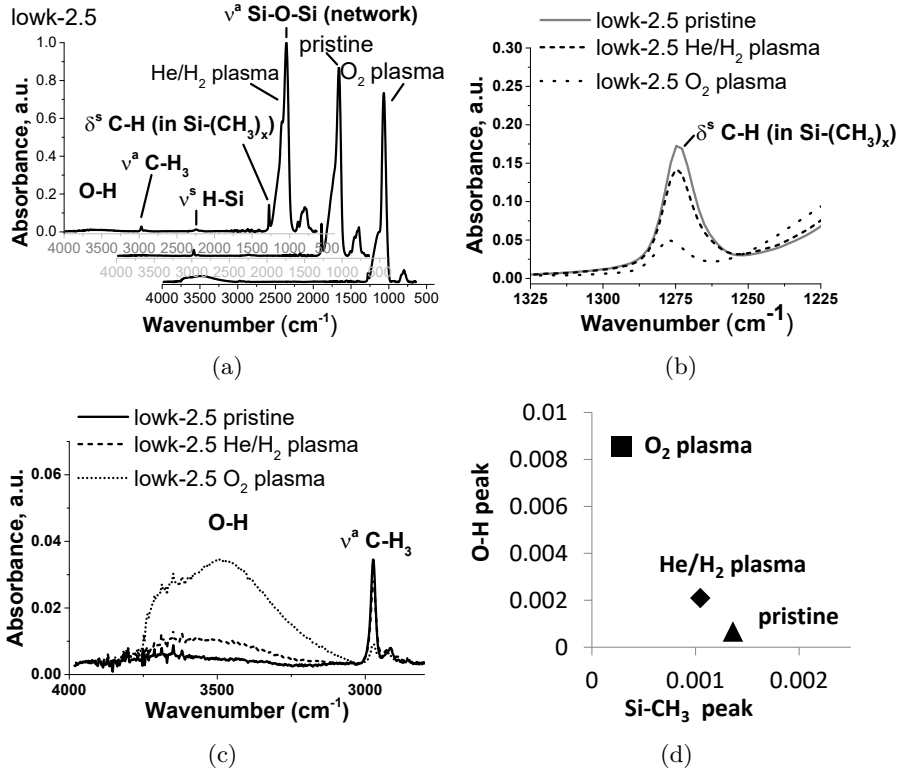

Figure 4.2: (a) Normalized FTIR spectra of lowk-2.5 before and after plasma pretreatment; (b) Zoom-in of the Si-(CH_3)x bending peak; (c) Zoom-in of the O-H and C-H stretching peaks; (d) Integrated O-H peak area vs. Si-CH_3 peak area.

with an increase in the intensity of the peak associated with the Si-OH groups (Figure 4.1a,4.2a,4.3a), indicating a conversion of Si-H to Si-OH, as reported by Niwano et al.[99][100] The amount of scissored Si-CH_3 bonds correlates with the amount of formed O-H bonds (Figure 4.1, 4.2, 4.3). This trend is even more evident in (b) and (c) in Figure 4.1d,4.2d,4.3d, which shows the correlation between integrated O-H and Si-CH_3 peak areas after the pretreatment. In the case of lowk-2.0 pretreated by O_2 plasma, the Si-CH_3 peak disappears (Figure 4.1b): all the Si-CH_3 bonds are removed

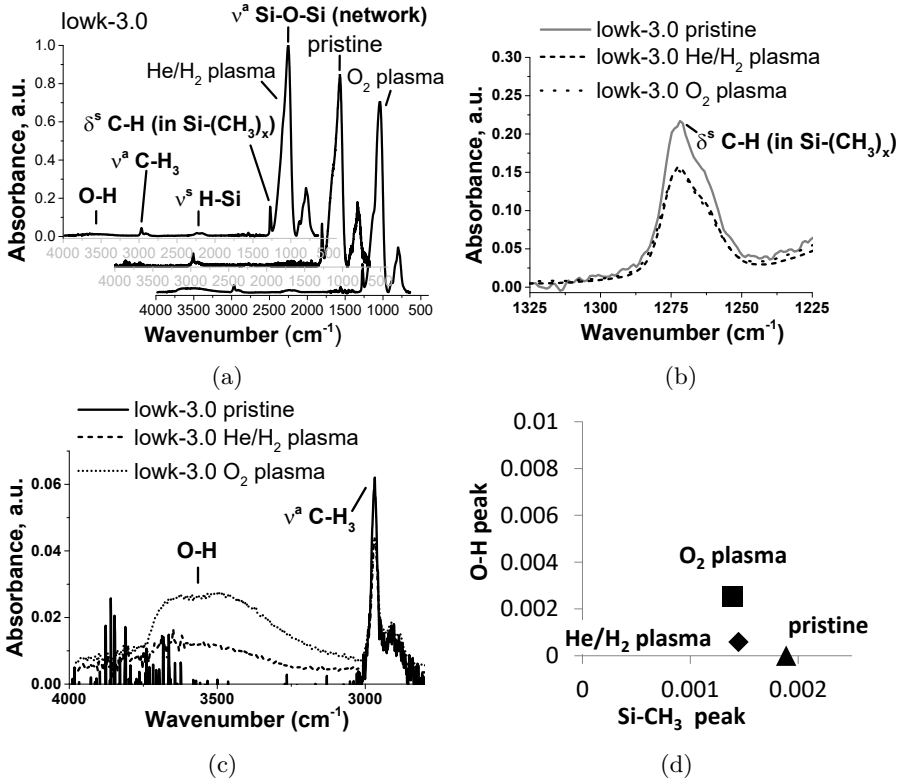

Figure 4.3: (a) Normalized FTIR spectra of lowk-3.0 before and after plasma pretreatment; (b) Zoom-in of the Si-$(CH_3)_x$ bending peak; (c) Zoom-in of the O-H and C-H stretching peaks; (d) Integrated O-H peak area vs. Si-CH_3 peak area.

and the film turned from SiCOH to a SiO_2-like porous material.

The chemical reactions between the oxygen radicals and the Si-CH_3 groups start with the detachment of a H followed by a reaction with the oxygen atoms, leading to a complete loss of the methyl groups.[101][102][103][104]

$$\equiv Si-CH_3 + O \longrightarrow \equiv Si-CH_2 \cdot + OH \tag{4.4}$$

$$\equiv Si-CH_2 \cdot + O \longrightarrow CH_2O \cdot + \equiv Si \cdot \tag{4.5}$$

$$\equiv Si\cdot + H(OH) \longrightarrow \equiv SiH(\equiv SiOH) \tag{4.6}$$

Similar trends are observed in lowk-2.5 and lowk-3.0, although the extent of plasma damage is lower than in lowk-2.0. The smaller pore size limits the diffusion of the plasma species into the bulk of the film, reducing the extent of damage (Figure 4.2,4.3). It is worth noting that, while the degree of damage in the O_2 plasma strongly depends on the pore size, the damage associated with the He/H_2 plasma is found to be almost independent of the pore size (Figure 4.1, 4.2, 4.3 and Table 4.1). The degree of Si-CH_3 depletion in lowk-3.0 is comparable after O_2 and He/H_2 plasmas, although the amount of adsorbed moisture after O_2 plasma is still larger than after He/H_2 plasma, as evidenced by the fact that the O-H peak after O_2 plasma is much higher than the one after He/H_2 plasma (Figure 4.3a,4.3c). These findings point to two different damage mechanisms induced by the two plasmas.

4.2 Pore size, PID and their influences on SAM's indiffusion

A clear correlation between the water contact angle values and the integrated O-H peak areas is observed after the plasma pretreatments: the larger the O-H peak area, the lower the WCA. When comparing Figure 4.4 and Figure 4.5a, we conclude that the as-deposited hydrophobic low-k films have a water contact angle above 90° which corresponds to a relatively small integrated O-H peak area. After the plasma pretreatments, an increased number of O-H functionalities accompanies a decrease in WCA. Nevertheless, this correlation is not quantitative since the water contact angle reflects the surface hydrophilicity while the FTIR peak quantification reflects the combination of surface and bulk hydrophilicity. The plasma treated low-k films show WCA lower than 40° and this value increases to

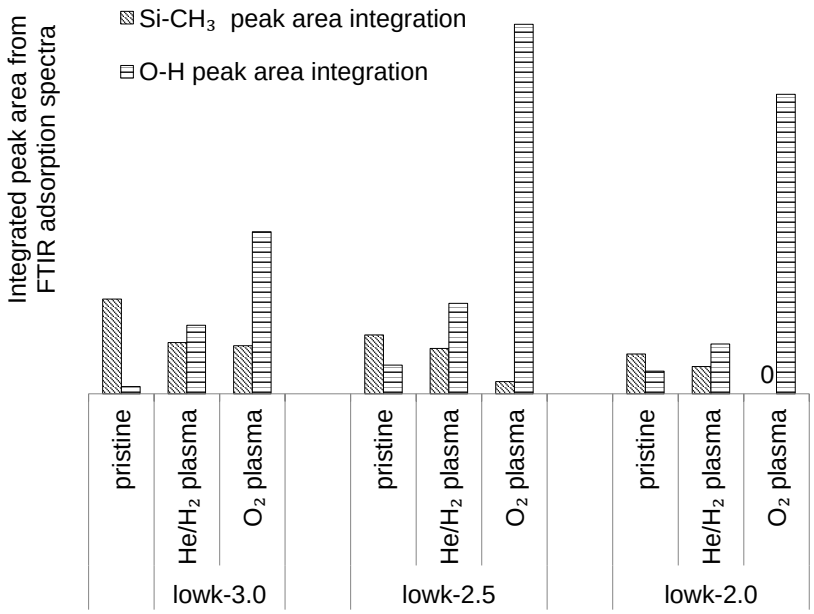

Figure 4.4: Integrated IR absorbance of the Si-$(CH_3)_x$ (2926 cm^{-1}) and O-H (3100-3900 cm^{-1}) peaks of the low-k films before and after the plasma pretreatments.

76.5 ± 2° after CNSAM deposition (Figure 4.5b). This is in agreement with the typical water contact angle values reported in literature for a CN-SAM grown on SiO_2 surface, suggesting a reasonable surface coverage.[105] On the hydrophobic pristine low-k surface, there are no reaction sites available for silanization. Therefore, the water contact angle remains unchanged after exposing the substrates to the SAMs precursors. The WCA measured on the O_2 plasma treated lowk-2.5 material is lower than that of the low-k 2.0 material. In addition, the OH peak area measured on the O_2 plasma treated lowk-2.5 is larger than that associated with lowk-2.0 (Figure 4.1d,4.2d). This phenomenon can be attributed to the microporous nature of lowk-2.5 which might promote condensation of water in the film either during sample storage in air or during the water contact

angle measurements.

The amount of SAMs deposited on the plasma pretreated microporous

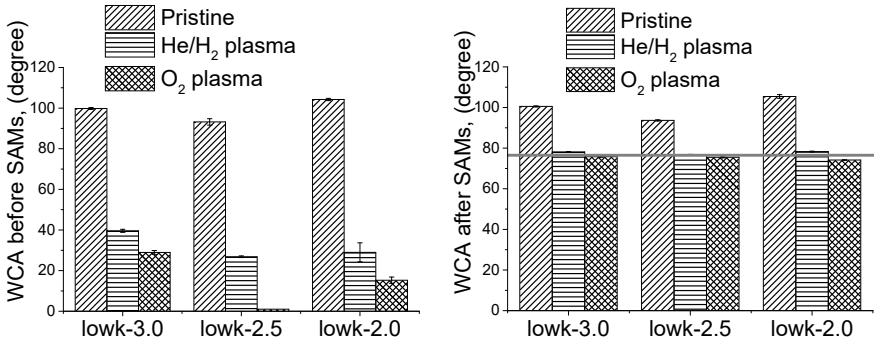

Figure 4.5: Water contact angle (WCA) (a) before and (b) after SAMs deposition. The horizontal line denotes the WCA of CN-SAM deposited on SiO_2 reference.

lowk-2.5 and lowk-3.0 films is approximately 30% lower than the amount of SAMs deposited on top of the SiO_2 surface (Figure 4.6a,4.6b). The reduced CN-SAM intensity can be explained by the lower density of the porous low-k films with respect to a SiO_2 surface. Since the CN-SAM molecules ($\sim$1.6 nm) are large if compared to the microporous structure, the possibility of a close-packed assembly of the SAMs precursors in the concave curvature of the porous surface is ruled out, resulting in a lower SAMs density. In the case of the plasma-treated lowk-2.0 (Figure 4.6c), the amounts of SAMs deposited after O_2 plasma and He/H_2 plasma are five and three times larger than the amount of SAMs deposited on the SiO_2 reference. The higher amount of SAMs deposited on lowk-2.0 pretreated by O_2 plasma with respect to He/H_2 plasma is justified by the larger number of generated -OH binding sites. Nevertheless, the density of the surface Si atoms is lower in lowk-2.0 than in lowk-2.5 and lowk-3.0, due to the highest porosity and/or pore size. Taking into account the significant bulk modification observed in lowk-2.0, the observed increase in the amount of

deposited CN-SAM can be attributed to the presence of SAMs at the inner pore sidewalls. The increase in the O-H peak area observed after SAMs deposition can be attributed to the presence of unreacted Si-OH groups in the hydrolyzed SAMs precursor (Figure 4.8).

The relatively high CH_2 peak intensity (2926 cm^{-1}) and low OH band

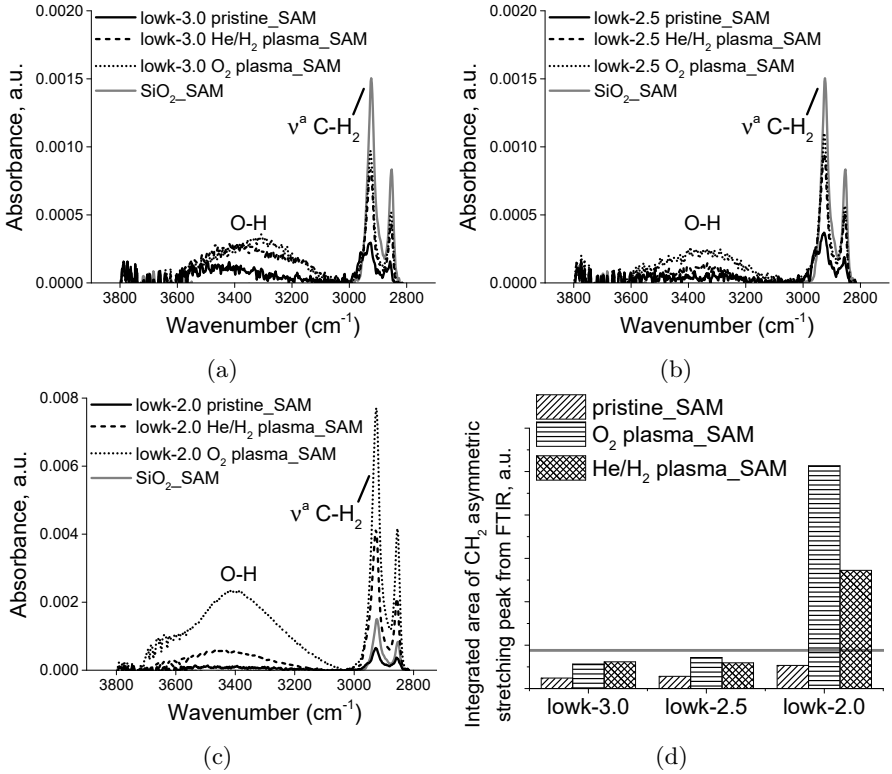

Figure 4.6: Differential FTIR spectra obtained by subtracting the spectra recorded before SAMs deposition from the spectra recorded after SAMs deposition. (a) lowk-3.0; (b) lowk-2.5; (c) lowk-2.0; (d) integrated area of the CH_2 asymmetric stretching peak centered at 2926 cm^{-1} obtained after peak deconvolution. The CH_2 peak area corresponding to the SAMs deposited on SiO_2 is taken as a reference and indicated by a horizontal line.

intensity (4000-3000 cm^{-1}) observed after SAMs grown on SiO_2 surface is an indication that dense layers were deposited. The ellipsometric

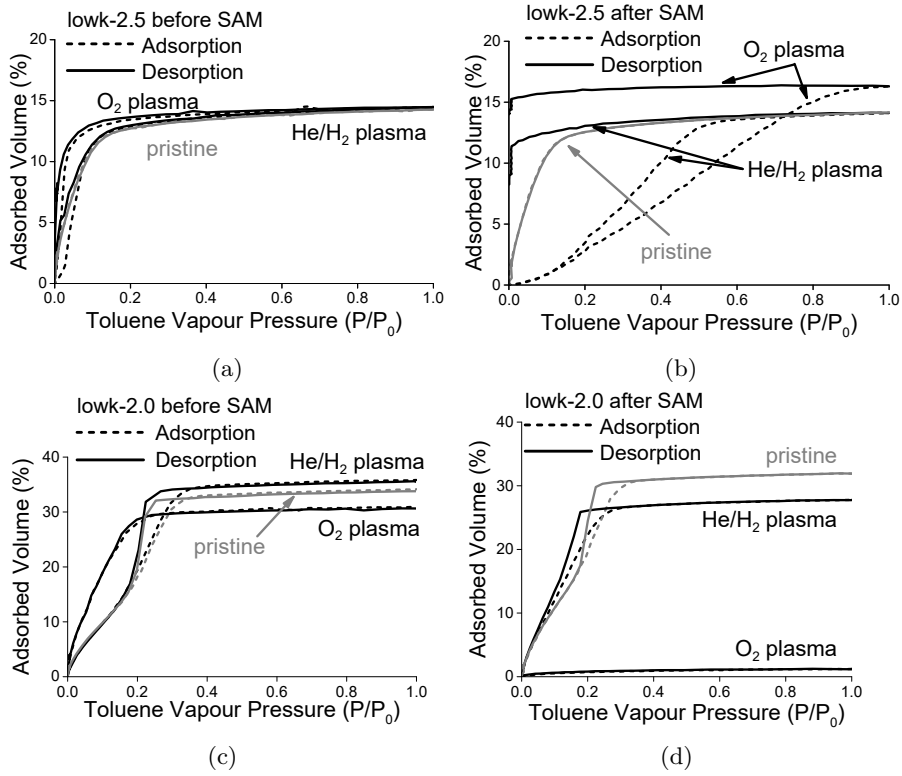

Figure 4.7: Adsorption/desorption isotherms, illustrating the pore volume occupied by the toluene molecules as a function of the toluene vapor pressure: (a) lowk-2.5 before SAMs deposition; (b) lowk-2.5 after SAMs deposition; (c) lowk-2.0 before SAMs deposition; (d) lowk-2.0 after SAMs deposition.

measurements of the SAMs thickness point to the formation of a monolayer (1.6 nm). It is reported in literature that lateral cross-linking via silanol groups condensation takes place between adjacent SAM molecules to form a densely packed monolayer.[106] Nevertheless, a more recent study showed that cross-linking should be avoided to achieve a dense film.[107] The main conclusion of aforementioned work is that, for a dense monolayer to form, all the three silanol groups of the silane precursor should be bonded to

the substrate. It has been reported that the density of -OH on silica is approximately 5-6 groups/nm^2.[108] The length of the Si-O bond of the silane molecules is about 1.68 Å. Assuming tetrahedral geometry (in the molecule, each Si atom is bonded to three oxygen atoms and one carbon with an angle of 109.47°), that makes a distance between two silicon atoms of 3.26 Å. All of these values are approximations only. The actual distances depend on the –OH groups density on the surface, the precursor chain length and terminal group and how the SAM is assembled (solvent, temperature, concentration, etc.).[106] Therefore, no conclusion can be drawn whether the SAM molecules anchor on hydroxyl-terminated substrate with one silanol end group or three end groups. In addition, the porous geometry of the low-k materials disrupts the packing of the SAMs, resulting in a reduced molecular density and the presence of unreacted dangling hydroxyl groups in the concave pore curvature, as compared with SAMs deposited on SiO_2 reference. This observation is in line with the findings reported by Bernardoni et al. Their results suggest that concave surfaces hinder, while convex surfaces assist the formation of closely packed and highly ordered SAMs. In particular, for SAMs of intermediate and long alkyl chains (more than 8 methylene groups in the backbone), the grafting density increases (by ∼20–40%), the molecular ordering improves, and the energy of adsorption interactions decreases in the following range of substrates: concave surface-flat surface-convex surface.[109] On the other hand, the presence of unreacted hydroxyl groups should be avoided since those groups might adsorb water molecules which have a k value as high as 80. Therefore, SAM precursors with a mono-anchoring group could be the preferred choice. On the other hand, the thermal stability of a mono-dentate SAMs might be lower than that of a tri-dentate SAMs. The chosen SAMs should be tested in terms of compatibility with the ULSI integration scheme and thermal budget.

Figure 4.7 shows the toluene adsorption isotherms before and after SAMs deposition on lowk-2.5 and lowk-2.0. The pristine lowk-2.5 film is

microporous and, therefore, no hysteresis loop is observed between the adsorption and desorption isotherms.[90] Exposure to He/H_2 plasma does not change the isotherms, which is an indication that the pore size remains unaltered. On the contrary, the exposure to O_2 plasma shifts the desorption isotherm to lower relative pressures, suggesting pore size reduction. Such densification of the low-k films after exposure to O_2 plasmas is already well-known and has already been described in literature.[19][110][111] The large hysteresis loop observed during the toluene adsorption and desorption cycles on O_2 plasma pretreated lowk-2.5 samples after silanization is related to the diffusion limitation of the toluene molecules in the small pores present in the densified surface area (partial sealing effect). [90] Despite a comparable amount of SAMs was deposited after the two plasma treatments, the SAMs sealing efficiency after O_2 plasma treatment is higher than the sealing efficiency observed after He/H_2 plasma, as can be concluded based on the wider hysteresis observed in the former case. This phenomenon has been attributed to the surface densification induced by the O_2 plasma (Figure 4.7a and Table 4.1). In the case of lowk-2.0, the molecular size of the CN-SAM precursor is smaller than the pore diameter and therefore the SAMs can penetrate into the pores. The amount of CN-SAM, deposited inside the pores was estimated from the change of refractive indices using Lorenz-Lorentz equation 4.7.[90]

In this equation, $n_{\mathrm{SAM}} = 1.42 - 1.45$ [112][113] and $n_{\mathrm{s}} = 1.45$ are the refractive indices of condensed SAMs and the low-k film skeleton, respectively. $\mathrm{n_{meas}}$ is the measured refractive index and $n_{\mathrm{air}} = 1$ is the refractive index of air in the empty pores. $\mathrm{V_{air}}$ and $\mathrm{V_{SAM}}$ are the relative volume of the empty pores and the volume occupied by the SAMs, respectively. The condensed SAMs molecules have refractive index close to the refractive index of the low-k matrix which can be approximated to

$\sim$1.45. The simplified equation 4.8 is obtained when assuming $n_{\mathrm{air}} = 1$:

$$\begin{aligned}\left(\frac{n^2{}_{\mathrm{meas}}-1}{n^2{}_{\mathrm{meas}}+2}\right) &= V_{\mathrm{air}}\left(\frac{n^2{}_{\mathrm{air}}-1}{n^2{}_{\mathrm{air}}+2}\right)\\ &+ V_{\mathrm{SAM}}\left(\frac{n^2{}_{\mathrm{SAM}}-1}{n^2{}_{\mathrm{SAM}}+2}\right)\\ &+ (1-V_{\mathrm{air}}-V_{\mathrm{SAM}})\times\left(\frac{n^2{}_{\mathrm{s}}-1}{n^2{}_{\mathrm{s}}+2}\right)\end{aligned} \tag{4.7}$$

The Equation 4.8 allows estimating the degree of pore occupation by SAMs. For instance, the lowk-2.0 treated by O_2 plasma has a refractive index of 1.46 after SAMs deposition (Table 4.1). It corresponds to zero-remaining porosity: all the pores in the low-k film are completely filled by SAMs. The He/H_2 treated samples show a refractive index of 1.32 after SAMs deposition. In this case, the empty pore volume is 26%, which is smaller than the porosity of the film before SAMs deposition (36%). These findings point to a possible localization of the deposited SAMs near the film surface (within $\sim 1/3$ of the film thickness). Our calculations are in good agreement with our porosity measurements (Table 4.1).

$$\left(\frac{n^2{}_{\mathrm{meas}}-1}{n^2{}_{\mathrm{meas}}+2}\right) = 0.27\times(1-V_{\mathrm{air}}) \tag{4.8}$$

The plasma treated microporous lowk-2.5 material has a pore radius below 0.7 nm and, therefore, the 1.6 nm SAMs precursor molecules cannot penetrate inside the pores, which results in a partial sealing behavior (Figure 4.7b). Nevertheless, the toluene vapor molecules are still able to penetrate through the already deposited CN-SAM molecules because of their intrinsically high miscibility. Once inside the pores, the toluene molecules are trapped in the pores and could not be easily desorbed when decreasing the toluene vapor pressure. After SAMs deposition, the refractive index of the mesoporous lowk-2.0 material increases from 1.30 to 1.46. According to the same calculation based on Equation 4.8, it

could be concluded that the free volume after SAMs deposition is zero. Therefore, even though the SAMs initially grow on the surface of the film, the subsequent incoming precursors are still capable of diffusing through the top layer into the whole dielectric thickness (Figure 4.8). The additive SAMs coating on the pore walls decreases the free volume of the mesoporous film and is not effective in preventing the diffusion of the incoming SAMs precursors or toluene molecules into the bulk of the film (Figure 4.7c,4.7d). In this case, the amount of SAMs deposited and their penetration depth purely depends on the extent of the plasma hydrophilization and on the availability of binding sites. It is worth pointing out that, although the toluene absorption experiments indicate that no sealing against toluene is achieved after SAMs deposition on mesoporous films, Rutherford backscattering spectroscopy (RBS) characterization indicates that CN-functionalized SAMs formed on lowk-2.0 can stop ALD precursors (tetrakis(dimethylamido)titanium (TDMAT) or tetrakis(ethylmethylamino)hafnium (TEMAH)) from penetrating into the bulk of the low-k film.[114][55]

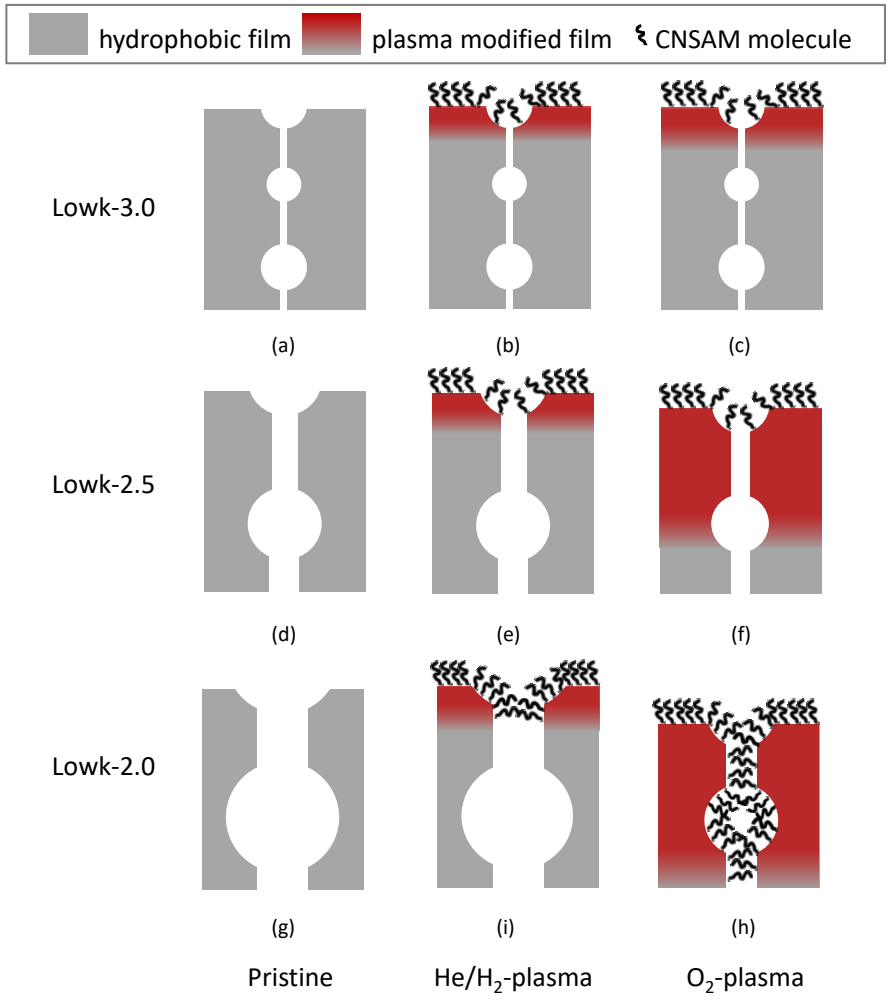

Figure 4.8: Schematic drawing of SAMs diffusion on (a-c) lowk-3.0; (d-f) lowk-2.5; (g-h) lowk-2.0. The plasma damaged layer is denoted by the reddish color. Pore size and hydrophilicity play a determining role in the distribution of SAMs molecules inside the porous film. On microporous low-k, the SAMs distribution is confined to the surface. When the pore size of the pretreated low-k material is larger than the threshold value, deposition of SAMs is driven by their reaction with the silanol groups. In this case, the SAMs distribution follows the profile of the silanol groups defined by the pretreatment conditions

4.3 Mechanism of PID

The as-deposited SiCOH low-k materials are hydrophobic and their pore walls are covered by CH_3 terminations in order to avoid the adsorption of moisture. Nevertheless, the SAMs density depends on the surface concentration of the binding sites. Therefore, surface should be pretreated in order to convert the surface Si-CH_3 groups to Si-OH functionalities. In this case, the main challenge is to achieve a surface-confined modification avoiding bulk low-k damage. The plasma treatments are considered relevant because the low-k films are exposed to etch and strip plasmas during the integration flow (patterning, resist strip and cleaning, barrier deposition etc.).

Two different resist strip plasmas have been evaluated in this research, namely O_2 and He/H_2 plasmas. They are normally used to remove organic photoresists. Therefore, they should be efficient in transforming the Si-CH_3 groups into Si-OH functionalities. The oxygen radicals in the O_2 plasma efficiently react with the Si-CH_3 groups and after a series of elementary stages related to the detachment of the hydrogen atoms, the Si-CH_3 groups are completely transformed to Si-OH functionalities.[115][116] The modification depth is dictated by the extent of radical penetration (L_{pen}) into the pores and this can be described by the diffusion-recombination theory of low-k plasma damage.[101] When the pore size is smaller than the free path length of the oxygen radicals, L_{pen} is described by the equation based on random walk theory:[104]

$$L_{\mathrm{pen}} \sim k(d) \times R_{\mathrm{p}} \left(\frac{1}{\gamma_{\mathrm{rcmb}}} \right)^{0.5} \tag{4.9}$$

where R_p is the pore radius, k(d) is the mean depth of the radical penetration into the low-k between two consequent collisions with the pore wall, which depends on pore diameter, tortuosity and is normally close to 1.5d. $\gamma_{\mathrm{rcmb}} = \gamma_{\mathrm{rcmb0}} + k_{\mathrm{r}}$, is the sum of the recombination coefficient of the

oxygen radicals on the pore walls (γ_{rcmb0}) and the reaction rate constant (k_r) of the radicals consumption in their reactions with carbon-containing surface groups. This equation predicts that the penetration depth of the oxygen radicals into the pores is proportional to the pore diameter, which is in agreement with our experimental findings (Figures 4.1b,4.2b,4.3b). In particular, the degree of O_2 plasma damage can be ranked as: lowk-2.0 > lowk-2.5 > lowk-3.0, where lowk-2.0 has the largest pore size and highest porosity.

The low-k modification with the He/H_2 plasma[117][118] has a different mechanism. Recombination coefficients of $(5.7 \pm 0.3) \times 10^{-3}$ and $(1.4 \pm 0.4) \times 10^{-3}$ have been reported for the oxygen and hydrogen radicals in the pores of lowk-2.5,[115] which means that the recombination coefficient of the hydrogen radicals is three to five times smaller than the recombination coefficient of the oxygen radicals. Therefore, the penetration depth is expected to be larger for the hydrogen radicals than for the oxygen radicals. If the hydrogen atoms are able to damage the low-k materials, complete degradation must have always been observed. The independence of the damage depth from the pore size suggests that the diffusion-recombination model discussed above is not applicable to the damage caused by the hydrogen atoms. Therefore, one can conclude that hydrogen atoms do not damage the bulk of the low-k material. This conclusion is in agreement with the results of a previous work published by Urbanowicz et al.[115], where a downstream hydrogen plasma is proposed as a damage-free porogen removal process for PECVD low-k materials. Therefore, the factor most likely responsible for the low-k damage is the VUV light generated in the He/H_2 plasma. Generally, the low-k damage from VUV light is dictated by two fundamental parameters: the photo absorption cross section and the effective quantum yield of the Si-CH_3 photo dissociation. According to the data published by Woodworth et al.,[119] the absorption coefficient of the amorphous silica increases when decreasing the wavelength of the VUV light from 160 nm to $\approx$ 120 nm and it is relatively constant in the

range between 122 and 85 nm. Moreover, it has been shown [95][116] that the degree of VUV damage is comparable in the emissions from He plasmas (58.4 nm) and Ar plasmas (106 nm). Therefore, the range of constant absorption coefficient of amorphous silica, most probably, is extended to 58.4 nm. In He/H_2 plasma, the VUV mainly comes from the resonant emission of atomic He at 58.4 nm and Lyman-alpha line of atomic hydrogen at 121.6 nm. Therefore, the VUV light emission of both helium and hydrogen atoms are located in the range of high and almost constant absorption coefficients of amorphous silica. Assuming that the VUV optical properties of the OSG low-k materials are similar to the amorphous silica, we can conclude that the degree of low-k damage should be similar in the lights emitted by helium and hydrogen atoms. Moreover, the depth of damage is limited to the thin top layer because of the large absorption coefficient. In a recent work,[95] it was also shown that the quantum yield of the VUV damage of the OSG low-k materials is almost independent of the porosity up to 40%, then a sharp increase of plasma damage is observed. This is the reason why in this work all three low-k materials have similar depth of damage when exposed to He/H_2 plasma.

Conclusion

We investigated the correlation between the extent of the plasma damage and SAMs pore sealing mechanism in porous dielectrics with k values of 2.0, 2.5 and 3.0, which correspond to 1.7, 0.7 and < 0.5 nm pore radius, respectively. O_2 and He/H_2 plasmas were evaluated. Due to the intrinsic hydrophobic nature of the low-k dielectrics, only a negligible amount of silane precursors is chemically grafted on the as-deposited materials. Both available surface binding sites and low-k pore radius dictate the distribution of the silane molecules in the porous films. The threshold pore diameter for SAMs' indiffusion is 1.4 nm, which is comparable to the chain length

of the CN-SAMs precursor. In order to seal mesoporous material with CN-terminated SAM, SAM precursors with longer chains are preferred. When the pore diameter of the pretreated low-k material is higher than this value, the SAMs' indiffusion into the pores is driven by the reaction between the silane precursors and the silanol groups. In this case, the SAMs distribution follows the in-depth profile of the silanol groups in the pores. For the O_2 plasma treatments, the extent of low-k damage is dictated by the diffusion of the oxygen radicals into the pores, while the plasma-generated VUV light plays a critical role in the low-k modification induced by He/H_2 plasma.
Our observations lead to technologically-relevant conclusions as to the enabling of a surface-limited pore sealing solution. The application of O_2 plasma is the preferred surface-modification route for microporous materials, because the micropores limit the depth of radical penetration. On the other hand, He/H_2 plasma can generate VUV light and is more suitable for mesoporous materials due to its largest photo absorption cross section. This conclusion is in agreement with some recent findings related to the modification of ultra low-k films by He/H_2 plasma for ALD deposition of TiO_2.[120]

Chapter 5

Evaporated Si as add-on layer for low-k surface activation

Introduction

As discussed in Chapter 4, most of the selective layers deposited chemically from SAM precursors need activation of the low-k film by a certain treatment which would generate sufficient hydroxyl groups on, and limited to the surface. Deductive activation methods like wet chemistry or plasma treatments would remove terminating -CH_3 groups and replace them with hydrophilic silanols. Without proper control, the low-k modification by those methods extends into the bulk and results in bulk deposition of SAM, which degrades the low-k properties.

An alternative to dry/wet subtractive method, is to add an extra hydrophilic layer. Silicon dioxide is a good candidate as an additive

overlayer because its chemical composition is not very different from the ones of the low-k films.
In this chapter, we propose to make the low-k surface hydrophilic with a 2-step method: first to cover the low-k surface with thin silicon, then oxidize the silicon to SiO_2. After the surface is covered with hydrophilic SiO_2, the pore sealing could be finalized by either metal barrier or a combination of SAMs and metal barrier. The SiO_2 also shrinks the pores on the surface, thus helps on sealing.
With the target of achieving minimal pore size, minimal thickness increase and minimal Si diffusion into the pores, several parameters in the silicon evaporation process are optimized including evaporation rate, evaporation angle, initial surface hydrophilicity, and add-on layer thickness. Based on the optimized conditions, the sealing of SAM on this type of activation is benchmarked with plasma pretreatment. Two different SAMs, CNSAM and APTMS are deposited and the amount of SAM, the thickness and electron density in the bulk is studied by SE, XRR, FTIR and EP.

In this work, Dr. Baumans performed the silicon evaporation. My contribution to this work includes task definition, material preparation, characterization, data analysis.

5.1 Understanding silicon evaporation behavior

Experiment

In this chapter, PECVD low-k samples are cleaved into 3×3 cm^2 pieces and attached to a carrier wafer for evaporation. Experimental details of silicon evaporation is introduced in Chapter 3. The following evaporation parameters are evaluated in order to optimize the process with a goal of

maximizing hydrophilicity, minimizing silicon thickness and shrinking the pores:

- Evaporation angles (the angle between the plane of carrier wafer and the boat): 0° and 75° (Figure 3.1).
- Deposition rates (measured by quartz crystal microbalance): 1 Å/s (referred to as *""low rate""* in this chapter) and 6 Å/s (referred to as *""high rate""* in this chapter).
- Low-k surface hydrophilicity: hydrophobic low-k pristine and hydrophilic low-k with plasma treatment. The samples are referred to as "pristine" and "plasma", respectively. The plasma pretreatment was performed in a capacitively-coupled plasma (CCP) 300 mm single wafer system at 150 °C for 20 s under H_2/Ar plasma ignited at 200 W.
- Nominal Si thickness after evaporation (d_N): The thickness measured on silica reference with profilometer. 1-8 nm of nominal thickness are evaluated.

WCA, FTIR, k value and porosity measurements are performed after evaporation. Two different models are used to fit the spectroscopic ellipsometry (SE) measurement results: A 1-layer Cauchy model with the refractive index and thickness floating. A 2-layer model with a bottom low-k layer where the thickness is equal to the thickness before Si evaporation, the refractive index (RI) floating, and a top SiO_2 layer where the thickness is floating and the RI equals that of pure SiO_2 (Figure 3.5, type I and III). The thickness obtained by fitting SE result with 2 layer model is referred to as d_S, which should be differentiated from the nominal thickness d_N.

Results and discussion

5 nm Si is evaporated onto bare Si substrate and oxidized to SiO_2 by annealing under O_2 flow at 250 °C for 30 mins. FTIR is measured before the evaporation and after the oxidation. The spectra before evaporation are subtracted from the spectra after evaporation and shown as dotted curve in Figure 5.1, which reflects the chemical modification of the evaporation process. FTIR spectra for bare silicon substrate (cleaned with diluted HF to remove oxide layer) are shown as reference (spectra in solid line). In the silicon substrate the most abundant bond is Si-Si bonds located at 609 cm^{-1}. In the samples with evaporated silicon, the peak at 1037 cm^{-1} indicates Si-O bond formation with some Si-Si bond. The peak height of Si-O bond is around 3 times that of Si-Si peak. For a rough estimation, around 60% of Si-Si bonds are converted to Si-O bonds. Si-H bond is also observed at 2116 cm^{-1}. Peaks around 2920-2970 cm^{-1} indicate organic inclusion in the evaporated film. OH/water peak observed at 3000-4000 cm^{-1} due to the formation of Si-O. The influence of evaporation angle is studied by rotating the carrier wafer in the chamber (Figure 3.1). Porosity measurements are performed to understand the influence of this parameter and the result is shown in Figure 5.2. Sample processed at 0° shows better sealing than that at 75° as indicated by a larger hysteresis between adsorption and desorption curves. 0° sample shows a higher thickness increase while the 75° sample shows relatively smaller thickness increase but much higher RI increase. The high RI increase is an indication of densification of the pores. For 75° sample the Si is mostly distributed inside the pores while for 0° sample the Si is mostly on the surface. Under oblique angle, it is easier for the Si atoms to diffuse into the pores[121]. Since silicon diffusion should be avoided, a 0° angle of evaporation is preferred over a tilted angle. This condition is selected for the remaining part of this research.

If Si evaporation is to be considered as a measure of surface pretreatment, it would be important that the surface is hydrophilic enough for SAM/barrier

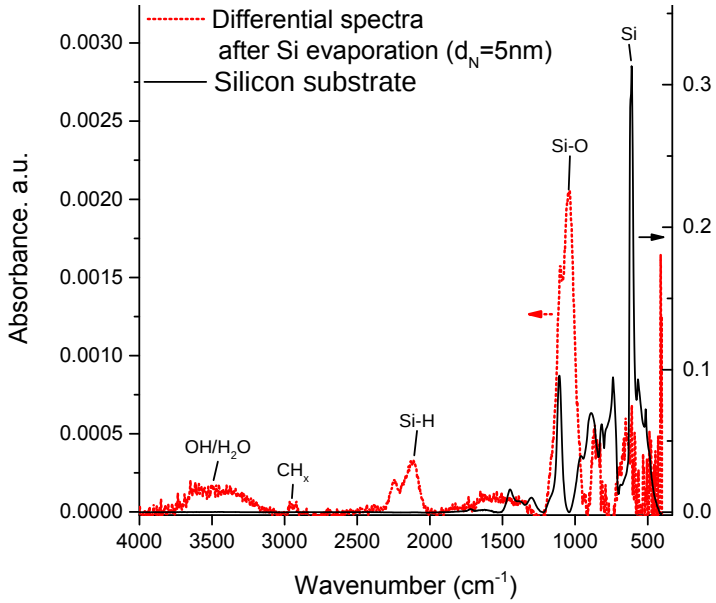

Figure 5.1: Comparing FTIR spectra from evaporated Si with the spectra of a Si wafer

precursors to deposit. The WCA after Si evaporation under different conditions are shown in Figure 5.3. Two types of sample with different initial surface hydrophilicity (low-k pristine and low-k after plasma treatment) are put in the same chamber side by side for each run. The low rate and high rate samples witness evaporation in two different runs. After Si evaporation and oxidation, the WCA values between pristine and plasma treated samples are very similar so the initial hydrophilicity has little or no influence on the WCA after Si evaporation. The difference in WCA between low rate and high rate samples are also small but high rate samples show slightly lower WCA, which might be because for high rate samples the roughness is higher. Figure 5.4 shows the actual thickness of Si evaporated for various d_N measured by 2-layer Cauchy model in SE (Figure 3.5, type III). One might notice the actual thickness is much higher than the nominal

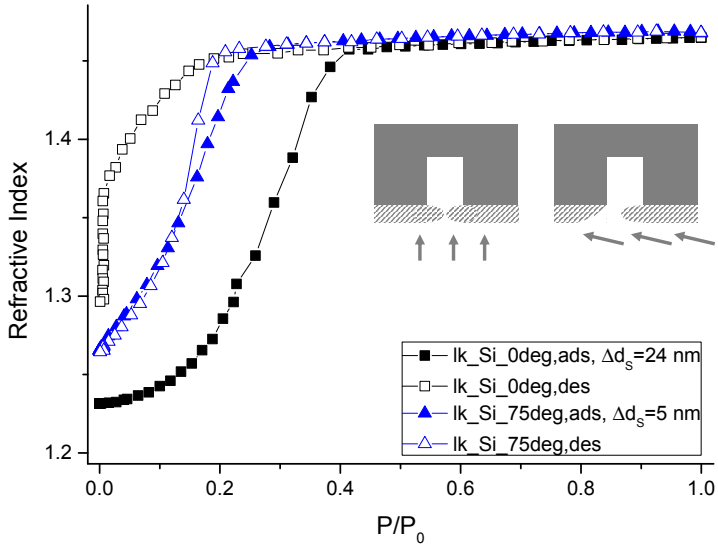

Figure 5.2: Influence of evaporation angle: adsorption/desorption isotherms, illustrating the RI change as a function of the toluene vapor pressure. Thickness increase after evaporation is shown in the legend. Inset: schematic drawing explaining the difference on EP results between the two angles

thickness measured on silicon carrier wafer. The higher thickness is due to two reasons: first, when silicon is oxidized to SiO_2, the thickness normally increases. Second, in our model the RI of SiO_2 layer is fixed to 1.46. But as indicated by FTIR measurement there is still 25% of silicon. Therefore the RI is underestimated which results in an overestimation of SiO_2 thickness. Although the silicon on pristine and plasma treated samples are deposited in the same run, the amount of SiO_2 is very different (Figure 5.4): On pristine samples, almost double or triple amount of silicon is deposited as compared with their hydrophilic counterparts. The reason behind this is unclear. Possibly because the chemical composition of pristine facilitates the adsorption of silicon atom. On the other hand, the deposition rate does not seem to have a consistent influence on the amount of SiO_2. The

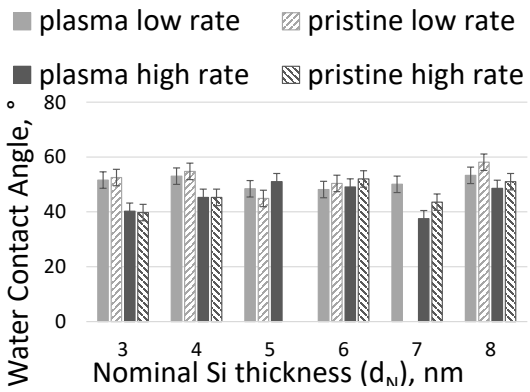

Figure 5.3: WCA after Si evaporation and oxidation

thickness measured by SE is correlated with FTIR measurements (Figure 5.5). The peak height increase at 2120 cm^{-1} (Si-H peak) is used to correlate with SiO_2 thickness because there are Si-O bonds in low-k so Si-O peak height increase is not suitable to represent amount of silicon deposited. Figure 5.5 shows that there is a correlation between SiO_2 thickness and Si-H peak increase, verifying the validity of the two techniques. It also shows that the effect of sealing is mostly dependent on the amount of SiO_2 formed on top of the surface, implying there is little (if any) density difference between high rate and low rate, or between hydrophilic and hydrophobic surface. The sealing efficiency of evaporated silicon is evaluated by ellipsometry porosimetry. The theory of this technique has been introduced in Section 3.4.3. For a perfectly sealed film, Ψ and Δ throughout the adsorption/desorption process should be a constant value. For a partially sealed film, toluene adsorbs at higher pressure and desorbs only partially at lower pressure.[88][122]

Figure 5.6 shows the Psi-pressure change during toluene desorption. After the EP measurements, a visual check is done on each sample and the results are shown as *visual inspection* in Table 5.1. For the films which are not sealed or completely sealed, the films are homogeneous without

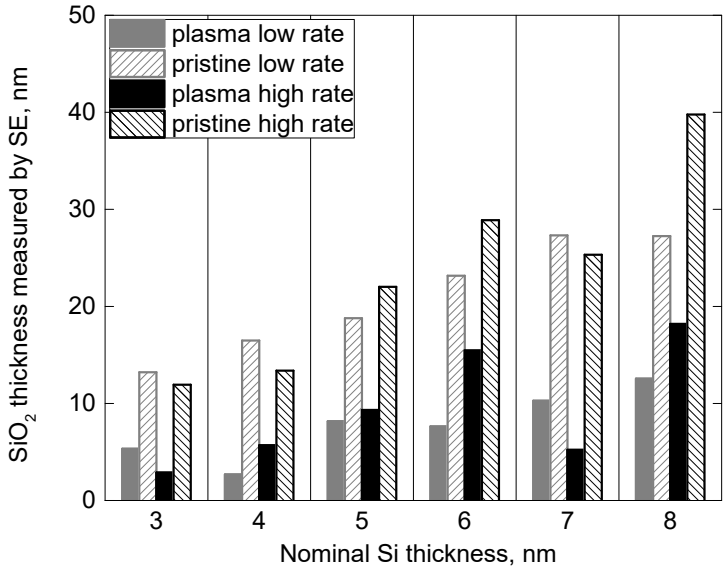

Figure 5.4: SiO_2 thickness for different nominal Si thickness under different deposition rate for hydrophilic and hydrophobic surfaces. The thickness is achieved by fitting SE measurement result with two layer Cauchy model described in Chapter 3, Figure 3.5, type III.

any visible toluene entrapment. For the films which are partially sealed, visual inspection shows darkened area where toluene residual decreases the RI difference between pore walls and therefore reduces light reflection at pore walls. Since Psi-pressure curve is an un-processed measurement result, it is more reliable than fitted data (RI and pore radius) because fitted data rely heavily on the model used and the goodness of fitting.[123] Tables 5.1 lists other parameters measured for the samples corresponding to Figure 5.6, where d_N is the thickness increase measured on carrier wafer (nominal Si thickness); $f(n) = \left[({n_{\mathrm{aft}}}^2 - 1)/({n_{\mathrm{aft}}}^2 + 2) - ({n_{\mathrm{bfr}}}^2 - 1)/({n_{\mathrm{bfr}}}^2 + 2)\right]$ is calculated from refractive index (n) of the whole stack with 1-layer Cauchy model measured before ($\mathrm{n_{bfr}}$) and after ($\mathrm{n_{aft}}$) silicon evaporation. This

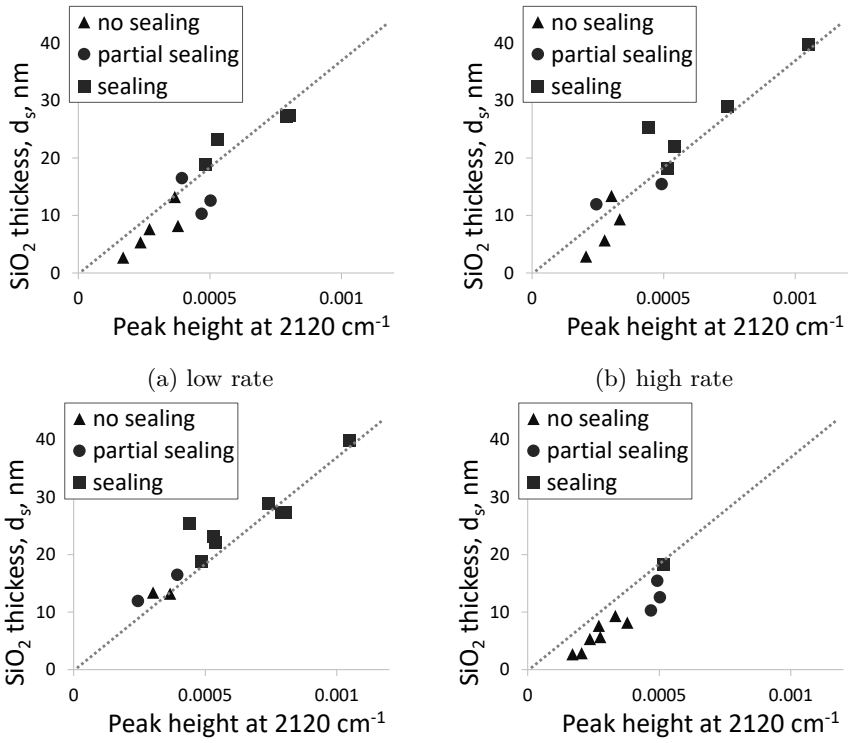

(a) low rate

(b) high rate

(c) on pristine surfaces

(d) on plasma treated surfaces

Figure 5.5: Correlation between SiO_2 thickness and Si-H peak height increase. Legend: *no sealing means little change in pore radius; partial sealing means measure pore radius is between 1.7-1.0 nm; sealing means measured pore radius is below 1.0 nm. Dotted line is a reference line. For the same SiO_2 thickness, a lower peak height with regard to the reference line is perferred because less difussion is indicated.*

parameter is interesting because of the equation below[124]:

$$P = 1 - \frac{\frac{{n_{\mathrm{meas}}}^2 - 1}{{n_{\mathrm{meas}}}^2 + 2}}{\frac{{n_{\mathrm{s}}}^2 - 1}{{n_{\mathrm{s}}}^2 + 2}} \tag{5.1}$$

,where P is the film porosity, $n_{meas}$is the measured refractive index and n_s is

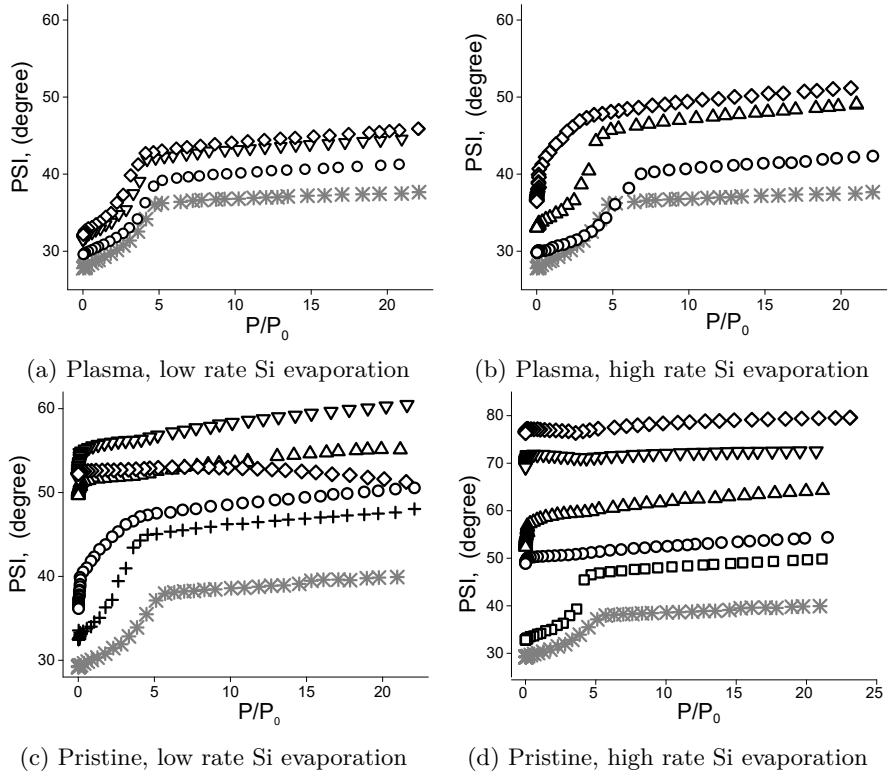

(a) Plasma, low rate Si evaporation

(b) Plasma, high rate Si evaporation

(c) Pristine, low rate Si evaporation

(d) Pristine, high rate Si evaporation

Figure 5.6: Psi evolution with pressure change for samples with evaporated silicon at desorption stage (thickness shown in the legend is nominal thickness). Symbols in legend: $*$ w/o Si, $\square$ 3nm Si, $+$ 4nm Si, $\bigcirc$ 5nm Si, $\triangle$ 6nm Si, $\triangledown$ 7nm Si, $\diamondsuit$ 8nm Si.

the refractive index of the skeleton. Therefore the change ($f(n) = \left[({n_{\text{aft}}}^2 - 1)/({n_{\text{aft}}}^2 + 2) - ({n_{\text{bfr}}}^2 - 1)/({n_{\text{bfr}}}^2 + 2)\right]$) before and after silicon evaporation is proportional to the porosity change because of silicon diffusion. d_S is the SiO_2 thickness measured by 2 layer Cauchy model under vacuum; *visual inspection* is the appearance of the sample after porosimetry measurement; R_p is the pore radius calculated from porosity measurement.

Figure 5.6a shows that for the samples of low rate evaporation on hydrophilic surface, Psi change is comparable to the samples before

Table 5.1: Table listing the numerical data from EP measurement d_N,nm: the thickness increase measured on carrier wafer (nominal thickness); *f(n)*: a parameter calculated from refractive index showing the change of porosity; d_S,nm: the SiO_2 thickness measured by 2-layer Cauchy model; *visual inspection*: the appearance of the sample after porosimetry measurement; R_p,nm: the pore radius

low-k plasma + low rate Si evaporation				
d_N	f(n)	d_S	visual inspection	R_p
5	0	8	no sealing	1.7
7	1	10	inhomogeneous, edge partial sealing	1.5
8	0	13	inhomogeneous, edge partial sealing	1.3
low-k plasma + high rate Si evaporation				
5	0	9	no sealing	1.7
6	1	5	inhomogeneous, edge partial sealing	1.5
8	3	18	inhomogeneous, partial sealing	0.7
low-k pristine + low rate Si evaporation				
4	0	16	–	1.4
5	1	19	inhomogeneous, partial sealing	0.6
6	2	23	partial sealing	0.7
7	3	27	partial sealing	0.5
8	14	27	partial sealing	0.5
low-k pristine + high rate Si evaporation				
3	3	12	no sealing	1.5
5	2	22	partial sealing	0.5
6	3	29	partial sealing	0.6
7	14	25	partial sealing	0.5
8	7	40	partial sealing	0.5

deposition. The sealing assessment is based on the principle that if the surface is sealed, or partially sealed, due to the presence of a dense layer, Delta and Psi will remain unchanged or only show a limited change during the exposure to toluene vapor. On the contrary, if the surface is porous,

the solvent adsorbs into the porous network of the dielectric stack leading to significant changes in Delta and Psi. What is interesting for this curve is the scale of Psi change from vacuum to saturated pressure. And also the pressure where the Psi curve starts to drop (the start of desorption from the pores). For the samples with higher d_N, Psi starts to drop at slightly lower pressure because smaller pores would make it more difficult for toluene to desorb, but the shapes of the curves are similar to the curves before deposition. The result matches with Table 5.1 where the f(n) value is low for all samples, the d_S is also low, the pore radius is above 1 nm for all samples. Visual inspection shows that there is only some toluene trapped at one edge of the sample, indicating the homogeneity is not ideal and the amount of silicon also depends on the positioning of the samples on the carrier wafer.

Figure 5.6b shows that for the samples of high rate evaporation on hydrophilic surface, the range of Psi change is comparable to the samples before deposition, indicating all the pores are still accessible to toluene. For $d_N = 8nm$ sample, the shape of the curve differs from that of other samples and toluene gets desorbed at much lower pressure. As shown in Table 5.1, f(n) value is 3 for this sample and the d_S value is also high, the pore radius is below 1 nm and visually the sample is partially sealed after EP measurement. For $d_N = 8nm$ samples, high rate results in more silicon both on top of the surface and inside the pores than the low rate counterpart.

Figure 5.6c shows that for the samples of low rate evaporation on hydrophobic surface, the pressure when desorption starts is already much lower than pristine samples on sample $d_N = 4nm$. For $d_N = 6nm$ or thicker d_N samples, the Psi change through the whole pressure range is small. For sample $d_N = 4nm$, Si is mostly distributed on the top surface since f(n) is low while d_S is high. The pore radius is below 1 nm for most samples (Table 5.1).

Figure 5.6d shows that for the samples of high rate evaporation on

hydrophobic surface, the pressure when desorption pressure starts is already much lower than pristine samples on sample $d_N = 3nm$. For higher thickness, the Psi change between saturation and vacuum is very little. However the f(n) value is high for this group of samples, indicating the silicon is mostly distributed inside the pores therefore this condition is not preferable as compared with low rate.
To conclude, more silicon is deposited on hydrophobic surfaces than hydrophilic surfaces therefore low rate evaporation is preferred.

5.2 Understanding the influence of the silicon pretreatment on SAM deposition, sealing and indiffusion

Experiment

Three different pretreatments are carried out on PECVD low-k films: H_2/Ar plasma, 1 nm Si evaporation (referred to as "Si(1nm)") and 5 nm Si evaporation(referred to as "Si(5nm)"). APTMS and CNSAM are deposited by dip coating. A 2 nm native SiO_2 film were used as a nonporous reference which experienced the same silanization procedure as the low-k samples. EP, SE, WCA, FTIR, k value, XRR, RBS and XRF measurements are performed on the samples after each processing step as detailed in the Chapter 3.

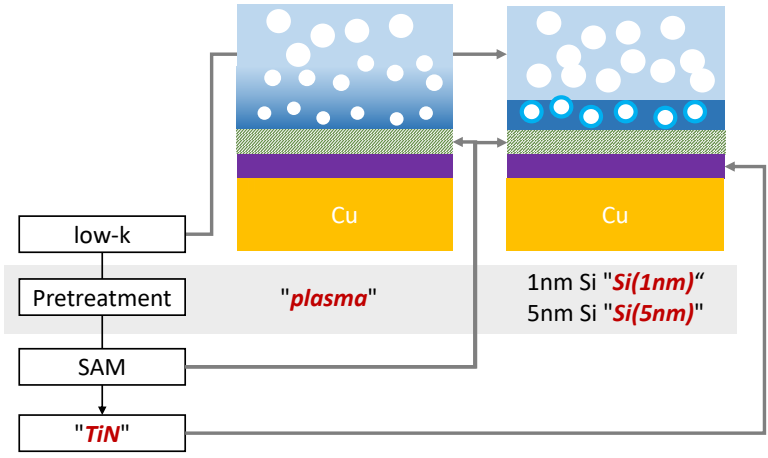

Figure 5.7: Processing flow of the experiment and legend nomenclature. After plasma pretreatment, pores on the surface are shrunk due to pore wall collapsing; After silicon evaporation and oxidation treatment, silicon oxide layer is formed on top of low-k with certain degree of silicon diffusion inside the pores. Long chain or short chain SAMs are deposited after pretreatments, followed by TiN ALD. This stack is meant to be a barrier for copper. Nomenclatures are shown as bold italic.

Results and discussion: SiO_2 formation, SAM deposition and TiN ALD

Figure 5.8 shows the FTIR spectra before and after pretreatment. The plasma treatment is etching low-k and damaging Si-CH_3 groups. In comparison, Si evaporation seems not modifying the Si-CH_3 groups but the SiO peak increases. If we normalize the Si-CH_3 by the height of SiO peak, it shows the two pretreatments have similar effect: in plasma pretreatment, the top layer of low-k is depleted with Si-CH_3 groups and transformed into a SiO_2 like layer. In Si evaporation, an add-on SiO_2 layer is formed. The two pretreatments are similar in a sense that, in both cases, for a given thickness of low-k film, the k value increases. In plasma treatment, the ion species cause the pore wall to collapse under bombardment, forming

a dense film. A more clear-cut and defined profile between hydrophilic and hydrophobic part of low-k is expected for Si evaporation pretreatment. WCA is performed as a preliminary check for SAM deposition and the

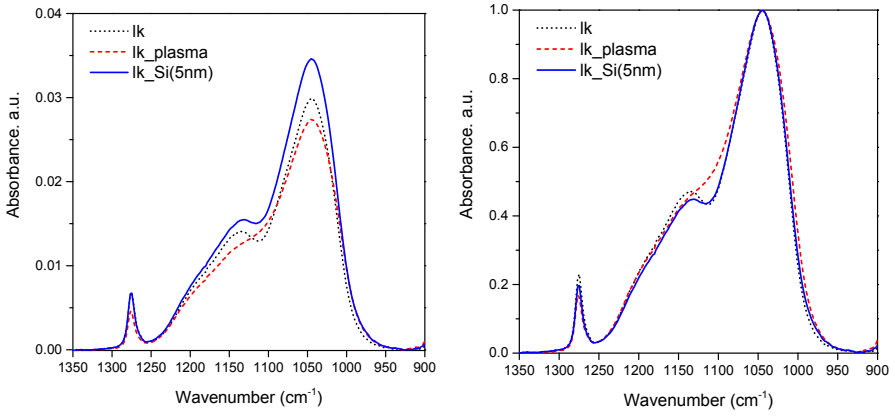

(a) Not normalized (b) Normalized

Figure 5.8: FTIR spectra after pretreatments: (a) not normalized; (b) normalized. The two pretreatments are similar in a sense that in both cases, for a given thickness of low-k film, the k value increases.

results are shown in Table 5.2. Contact angle of CNSAM is in line with previous results ($76.5 \pm 2°$).[69] After the deposition of APTMS, more than $10°$ of difference in WCA is observed between SiO_2 and low-k samples. The reason is that, the WCA of APTMS is very sensitive to surface roughness. On smooth SiO_2 surfaces, WCA as high as $65°$ is measured while this value decreases to $52°$ on plasma treated low-k surface.

SAM thickness is measured on plasma-pretreated surface by SE with a 2 layer Cauchy model: Psi and Delta spectra are collected before and after SAM deposition on the same sample. After SAM deposition, the low-k layer thickness is fixed to the original thickness before SAMs deposition. The RI of low-k layer is set to float allowing for SAMs diffusion. The thickness of top SAM layer is set to float and the RI of SAM layer is fixed to 1.46 (assuming the SAM layer has the same electron density as SiO_2). The

Table 5.2: Water contact angle before and after SAM deposition

Substrate	no SAM, °	CNSAM, °	APTMS, °
SiO_2-UVO_3	5 ± 10	77 ± 2	65 ± 5
low-k-plasma	42 ± 2	75 ± 2	52 ± 5
low-k-SiO_2	45 ± 10	75 ± 2	57 ± 5

results are shown in Figure 5.9. The theoretical molecule length is 1.6 nm for CNSAM and 0.6 nm for APTMS. On both flat and porous surface, the thickness is higher than chain length of monolayer, therefore most probably a double or even triple layer is formed. The f(n) is a parameter explained in Equation 5.1 which indicates the amount of SAM diffused into low-k. Comparing APTMS-sealed and CNSAM-sealed samples, we can see that there are more precursor molecules diffused into low-k in the former case. Due to the difficulty of finding a reliable model, SE measurement results on silicon-pretreated low-k material is not shown.

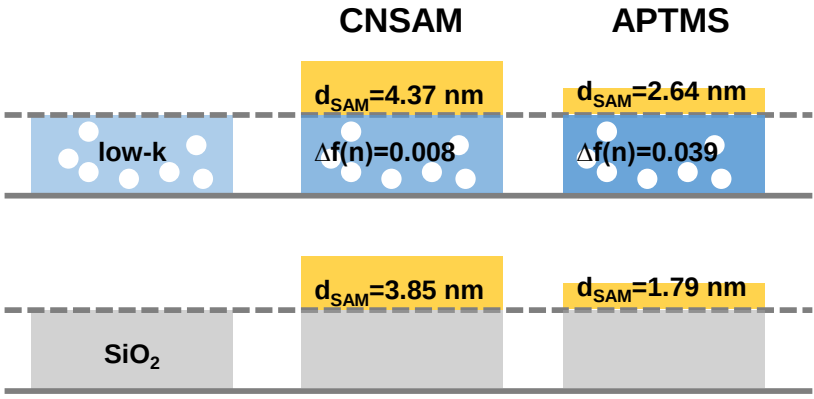

Figure 5.9: SAM thickness deposited on plasma treated low-k and SiO_2 surfaces as measured by SE

FTIR measurements are performed on the same sample before and after SAM deposition. The two spectra are subtracted from each other and

the results are shown in Figure 5.10. Since there are no CH_2 groups in the region of 2800-3000 cm^{-1} in the original low-k, therefore the change in this region could only be caused by SAMs. The peak around 2923 cm^{-1} is assigned to CH_2 group and this peak is narrow for CNSAM as compared with APTMS, indicating the CH_2 in CNSAM has less structural variations. The CNSAM on SiO_2 is used as a reference of the amount of SAMs grown on smooth surfaces. The CNSAM on 5 nm Si is even lower than this peak, indicating the SAMs density is lower for this surface due to fewer silanol groups. For 1 nm Si-pretreated surface, more SAM is detected compared to bare SiO_2 reference, indicating certain degree of diffusion into the pores. Plasma-pretreated low-k gets the biggest amount of CNSAM because the damage layer is thicker for this sample. There is also a blue shift of CH_2 peaks for low-k samples as compared with SiO_2 because the alignment of SAM backbone is more difficult on rough and porous surface. Therefore it is difficult for SAM to form a 2D crystalline layer under Van der Waals forces. As compared with CNSAM, APTMS shows CH_2 peaks broadened, possibly because inter- and intra-molecule hydrogen bonds change the orientation of backbones.

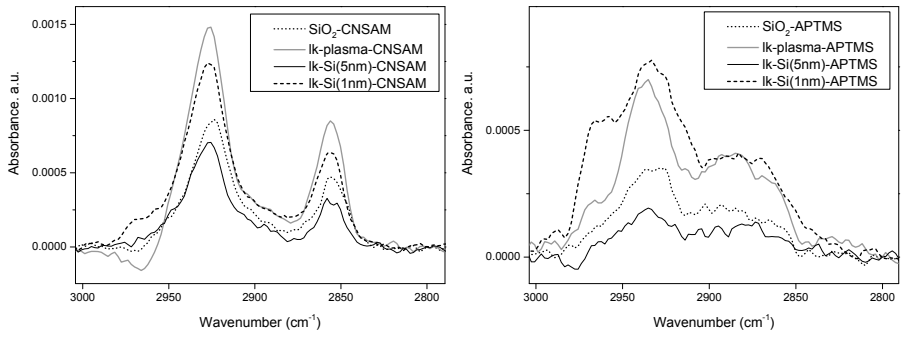

Figure 5.10: Differential FTIR spectra obtained by subtracting the spectra recorded before SAMs deposition from the spectra recorded after SAMs deposition: (a) CNSAM; (b) APTMS.

Figure 5.11 shows the critical angles of the film and the substrate ($\theta_{c,film}$ and $\theta_{c,Si}$). Oscillations between the two critical angles are the waveguide modes for X-rays confined in the film. Qualitatively the critical angle indicates the electron density in the film. Therefore it is concluded that for plasma-pretreated surface, the samples with SAM has higher θ_c and therefore higher electron density. The APTMS causes higher electron density as compared with CNSAM. On Si evaporated surface, the trend is opposite: CNSAM causes higher electron density, this phenomena will be discussed later.

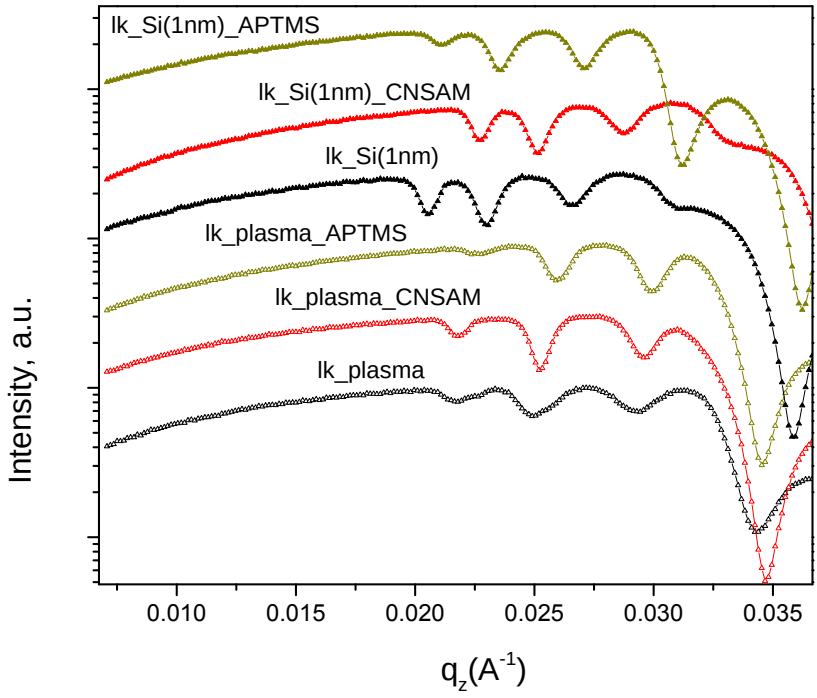

Figure 5.11: Electron density is indicated by critical angle (θ_c) measured by XRR, curves are offset by $10^{0.5}$

Figure 5.12 shows the EP measurement results on different surfaces. For the group of plasma-pretreated surfaces, APTMS causes higher RI under

vacuum without visible hysteresis, indicating the SAMs are mainly stuffing inside low-k without modifying the pore structures. For Si evaporated surfaces, APTMS causes moderate increase of RI and a big hysteresis is observed, indicating that APTMS modifies the pore structure on the surface and achieves almost complete sealing. For all CNSAM modified samples, no hysteresis is observed. This might be because toluene can penetrate through the hydrophobic chains of CNSAM and shows a pore structure of no sealing, while APTMS forms inter- and intra-molecule hydrogen bonds and stops the penetration of toluene. From Figure 5.12, the sample of *"lk-Si(1nm)-APTMS"* shows the best sealing with APTMS thickness of 2.6 nm.

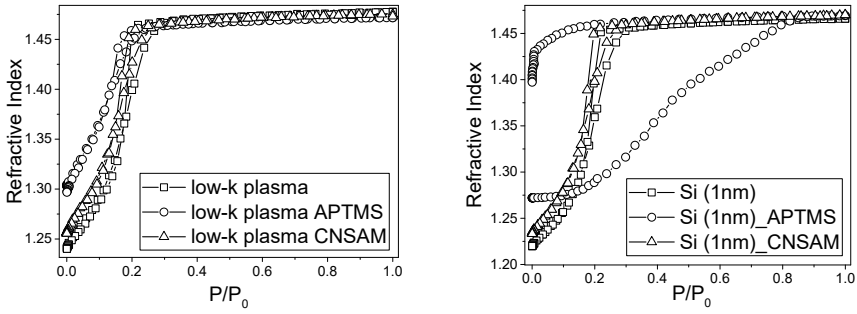

(a) plasma-pretreated surfaces (b) Si evaporated surfaces

Figure 5.12: Pore sealing of SAMs on different surfaces as measured by EP.

To test if evaporated silicon could seal the pores against ALD metal barriers, TiN was deposited by ALD on samples with 5nm and 1nm nominal Si thickness on pristine samples. RBS measurements are done subsequently and Ti distribution at different depths is calculated and the results are shown in Figure 5.13. For the sample $d_{\mathrm{N}} = 5nm$, no Ti is detected inside low-k, similar to reference samples where TiN is deposited on nonporous SiO_2 surface. For the sample $d_{\mathrm{N}} = 1nm$, Ti is still detected inside low-k film though the intensity is lower than that of low-k pristine. Therefore, $d_{\mathrm{N}} = 5nm$ is good for pore sealing together with metal barrier and $d_{\mathrm{N}} =$

1nm could be considered for pore sealing together with SAM and metal barrier.

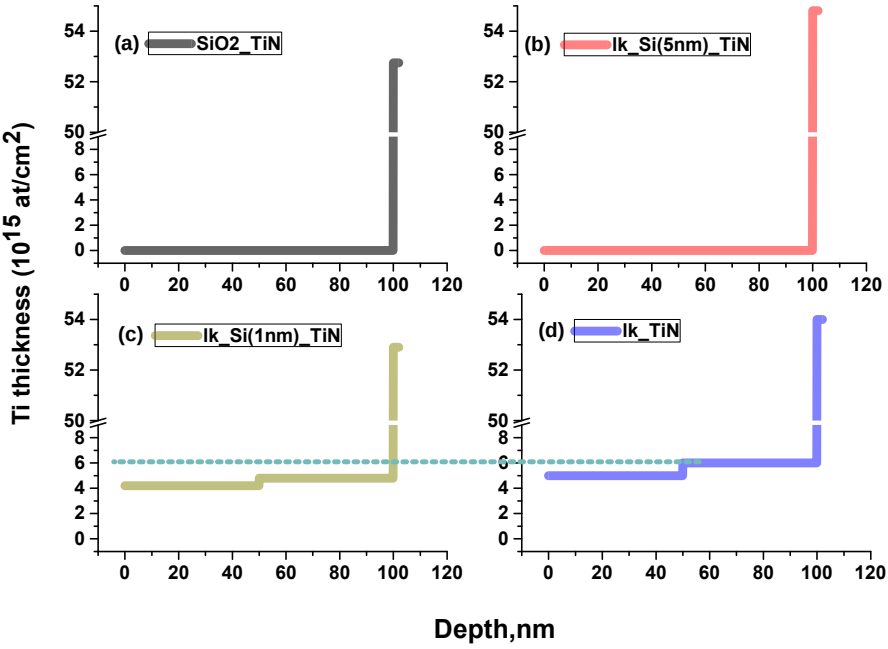

Figure 5.13: Ti diffusion for samples after Si evaporation as measured by RBS. x-axis is the depth of low-k where x=100 is the bottom and x=0 is the surface. Samples with SAMs also seal but results not shown here.

Conclusion

In the first part of this chapter, the silicon evaporation behavior on low-k surface is studied. The influence of evaporation angle, initial surface hydrophilicity, evaporation rate, nominal evaporation thickness are examined. The target is to have minimal water contact angle, minimal silicon diffusion and maximal shrinkage of low-k pores. 0 °evaporation angle, low rate evaporation on pristine surface gives better result than other conditions. EP results show that the 3 nm silicon can partially shrink

the pores. In the second part of this chapter, the pretreatment of 1 nm silicon evaporation on low-k 2.0 material are studied. H_2/Ar plasma is used as a reference. Afterwards, two different SAMs, CNSAM and APTMS are deposited and the amount of SAM, the thickness and electron density in the bulk is studied by SE, XRR, FTIR and EP. The silicon evaporation process does not cause Si-CH_3 depletion in low-k material. SAMs thickness on plasma treated low-k measured by SE and fitted by 2-layer Cauchy indicates a double- or triple-layer formation for both SAM precursors. For SAMs on plasma treated surface, SE measurement shows an increase of electron density of plasma treated low-k film after SAMs deposition, indicating SAMs diffusion in H_2/Ar plasma pretreatment. XRR shows an increase of electron density on 1 nm silicon-pretreated samples after SAM deposition. Therefore silicon evaporation pretreatment can not totally eliminates SAMs diffusion. The possible reason is the silicon atoms can still diffuse into low-k and introduce silanol groups inside. On 1nm Si pretreated sample, higher electron density after CNSAM is observed as compared with APTMS. It might be because APTMS forms inter- and intra-molecule hydrogen bond and generates a good sealing layer, blocking the further self-diffusion of SAM precursors. While the sealing of CNSAM is not as good as APTMS and precursors can still penetrate even though there are already a layer of SAM on the surface. FTIR measurements show that more CNSAM molecules are deposited on 1 nm Si evaporated low-k than SiO_2 reference, possibly due to diffusion, which is in agreement with XRR results. For a PECVD low-k material fabricated with pretreatment, self-assembled monolayer (SAM) sealing and TiN ALD process, RBS measurement is performed to detect Ti distribution in the low-k bulk. For the sample without the SAM sealing process, Ti atoms diffused from the top layer into the OSG film for pretreatments of plasma and Si(1nm) but not for Si(5nm).

Chapter 6

Wet pretreatment for surface-confined low-k activation

Introduction

In last chapter, the approach of additive layer low-k activation is discussed. Although the additive activation does not cause methyl depletion, the thickness of the low-k film is increased and therefore the "concentration" of methyl groups is lowered. Eventually the k value is affected. What's more, it is dubious that the evaporation can form a conformal and homogeneous film. Therefore it is also interesting to study the subtractive activation, which can be further categorized into pretreatment by dry chemistry (plasmas) and wet chemistry.

Wet chemistry is interesting because it takes advantages of the hydrophobic nature of low-k pore wall. Due to the existence of hydrophobic Si-CH_3

groups in low-k, the diffusion of water based solution inside low-k pores is much slower than radicals, ions or photos. Therefore a surface confined activation might be easier to realized as compared with plasma or UV based approaches. Armini et al. has successfully demonstrated the feasibility of low-k pore sealing by combining wet pretreatment, vapour phase SAM and HfO_2.[70] Nonetheless, the dip coating of SAM on wet activated low-k surface has not been studied yet.

For a successful wet pretreatment, the chemical solutions should meet several standards. i). it should be compatible with BEOL processing and not introduce unwanted contamination. Therefore solution containing metal ions should be avoided. ii) it should be able to stripe organics. In this chapter, we compared three different wet pretreaments for the purpose of low-k surface confined activation: Tetramethylammonium hydroxide (TMAH), Hydrogen fluoride (HF) and Sulfuric Peroxide Mixture (SPM). The reason why those chemistries are selected are summarized in a previous publication [70] Diluted HF is selected because it is used to remove or etch SiO_2 and the low-k is mainly SiO_2 based. SPM is a highly oxidizing acid and it is very efficient in creating OH sites. TMAH is selected because the ammonium hydroxide ion pairs adsorb on the hydrophobic low-k surface, which results in local pH increasing on the surface and enhancement of the Si-O-Si hydrolysis reactions.

With a target of maximizing surface hydrophilicity and minimizing low-k damage, their advantages and drawbacks are analyzed. We then studied the growth kinetics of SAM formation by dip coating the samples in SAM precursor solution. The deposition of SAMs on surfaces exposed to different chemical pretreatments is characterized and discussed.

The wet pretreatments and corresponding characterizations were performed by Jana Prado for her master thesis. My contribution to this work includes deposition of SAMs, characterization on SAM covered samples, and data analysis.

Experiment

PECVD k=2.0 samples are cleaved into 3×3 cm^2 pieces and exposed to the three different types of pretreatment introduced in Section 3.2.2. Based on the characterization results, optimal pretreatment conditions are defined for each chemistry: 0.5% for 4 minutes in HF; 100 °C for 5 minutes in SPM; 10% for 30 s under 60 °C in TMAH. Subsequently, CNSAM are deposited by dip coating with the protocol mentioned in Section 3.2.2. FTIR, WCA, XPS and SE measurements are performed before and after SAM deposition. A one layer Cauchy model is used to fit the data. Thickness before and after SAMs deposition is deducted and the difference is reported as SAMs thickness. In XRR measurement, a two-layer model composing SAMs and low-k is used to fit the data.

6.1 Development of wet pretreatment for low-k activation

TMAH

The etching of low-k in TMAH solution was studied by Want et al. and they found that the similar polarity between low-k and alkyl-substituted ammonium ions is helpful in the dissolution of the organic component in these Spin-on-glass (SOG) and the hydrolysis reactions of SOG are enhanced by adding TMAH.[125] Owing to the weak bonding of the $OH(CH_3)_4N^+$ cation and the associated OH^- ion, the OH^- ions are separated and can be supplied to the basic organo-silica dissolution reaction. Also in this case, a larger number of -CH_3 groups are replaced by hydroxyl functionalities. In our study, three different concentrations under three temperatures are tested for various etching times. Table 6.1 shows the etch rate of TMAH for low-k 2.0: higher concentration and higher temperature

results in higher etch rate, which is different than SiO_2 surface.[126] For temperature as high as 70 °C, the etch rate is so high that the whole 90 nm of low-k film is fully etched. Figure 6.1 shows the WCA of low-k after

Table 6.1: Etch rate of TMAH for PECVD low-k 2.0. "–" means etch rate is too high that the whole low-k film is etched off instantly.

Etch rate, nm/s	50 °C	60 °C	70 °C
10%	0.051	0.227	–
15%	0.202	0.487	–
20%	0.235	–	–

etching. For the extremely high concentration and long etching time, the low-k film is fully etched therefore the WCA is not reflecting the low-k surface and they are shown as solid grey. The etching rate at 70 °C is too fast and the low-k film is etched away almost instantly. At 50 °C, even the highest TMAH concentration with the longest treatment time results in a WCA of 60°. Therefore only 60 °C should be considered. The WCA does not have a linear dependence on concentration. This might be because the TMAH treatment is a synergistic reaction of hydrolysis and acid-base reaction. For 50% concentration, 30 s treatment time results in a more hydrophilic surface than all other conditions. Since longer treatment time results in higher thickness loss, potential delamination between low-k and substrate interface, therefore the shortest treatment time and lowest concentration are selected as the optimal conditions.

SPM

The application of an SPM solution on SiO_2 surface decreases the amount of organics on the surface and reduces the surface micro-roughness.[127] On low-k surface, the SPM would oxidize the Si-CH_3 groups and convert

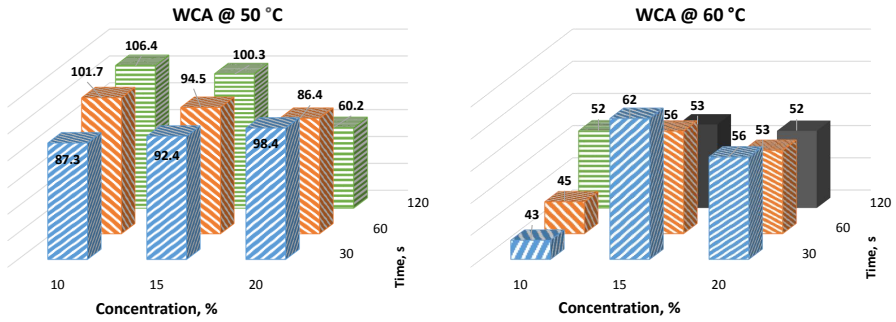

(a) (b)

Figure 6.1: WCA after TMAH pretreatment of low-k 2.0 under different concentration, temperature and time: the contact angle change is sensitive to temperature. Under extreme conditions, the low-k film is fully etched therefore the WCA is not reflecting the low-k surface and they are denoted by a solid grey color

them into silanol groups. Different temperatures and pretreatment times are evaluated and the results are shown in Figure 6.2. Similar to TMAH,

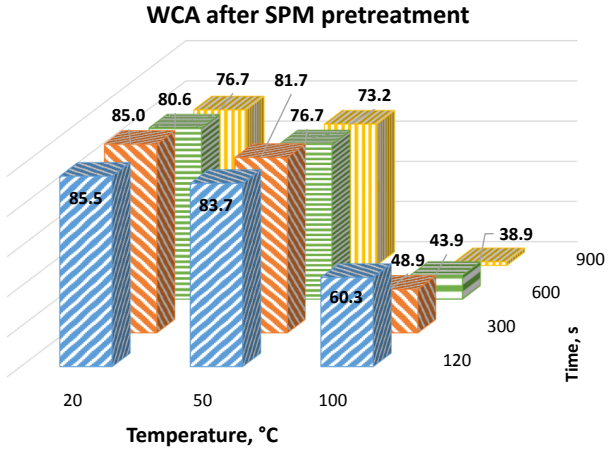

Figure 6.2: WCA after SPM pretreatment of low-k 2.0 under different temperature and time: higher temperature and longer immersion time results in lower contact angle.

the final surface contact angle is sensitive to temperature: Only when temperature is as high as 100 °C, the WCA is lower than 50 °. Under 100 °C, the WCA decreases with longer pretreatment time. The condition of 5 minutes under 100 °C is selected since this gives a WCA below 50° and is less damaging as compared with longer treatment time (based on the equivalent damage layer thickness generated from FTIR measurement).

HF

HF is mostly used to dissolve SiO_2.[128] It converts Si-O to Si-F bonds which are not stable and immediately convert to Si-H bonds. In the rinsing step after pretreatment and during storage in atmosphere, the Si-H bonds are further oxidized into Si-OH bonds. the existence of Si-CH_3 groups in low-k would make the surface hydrophobic and therefore the steric effect would make the Si-O bond less accessible to H_2F_2 and $HF_2{}^+$ ions. Therefore the efficiency of making low-k surface activated depends on how the Si-H bonds could be converted to Si-OH bonds. In this sense, HF pretreatment is less interesting as compared with SPM and TMAH. Higher concentration and longer treatment time would result in slightly lower WCA but even for the most aggressive conditions tested (5% concentration for 5 minutes), the WCA is still higher than 50°. Eventually we select the condition of 0.5% HF for 4 mins, which shows a WCA of 69 °.

Wet pretreatment summary

Figure 6.3 shows the carbon atom percentage after pretreatment measured by XPS. In angle-resolved XPS measurement, the spectra were recorded at exit angles of 21° and 78°, as measured from the normal of the sample. Results measured at 21° from normal are sensitive to the bulk of the low-k at a depth of 10 nm from the surface, which is a relevant low-k thickness

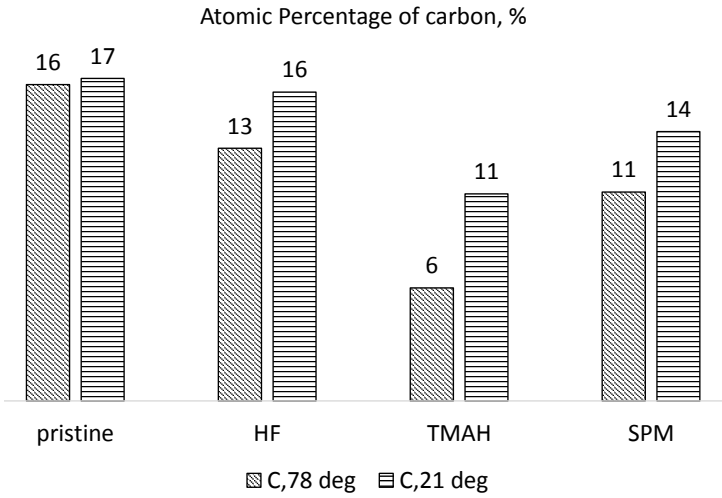

Figure 6.3: XPS measurement result comparing carbon percentage after different pretreatments on surface and in the bulk: TMAH is the most damaging pretreatment while also remove most Si-CH_3 groups from the surface. 78 deg is the surface and 21 deg is the bulk.

when considering narrow pitch interconnects and results measured at 78° are sensitive to the top low-k surface. Our target is to have minimal carbon atom percentage in the surface and preserve maximal carbon content in the bulk. After HF pretreatment, the carbon content is almost the same as pristine. SPM removed 30% carbon from the surface while TMAH removes 63%. But TMAH also removes 35% carbon from the top 10 nm near the surface. XPS measurements indicate that aside from transforming Si-CH_3 groups to Si-OH or Si-H groups, no other chemical modification happened to low-k after the wet pretreatments. This is also shown in FTIR spectra (Figure 6.4): no extra peaks from new bonds appearing after pretreatment, only a decrease of CH_x peak and an increase in OH/H_2O peaks. Among all pretreatments, the highest OH/H_2O peaks are observed after TMAH pretreatment.

The comparison of the three different chemistries is summarized in 6.4

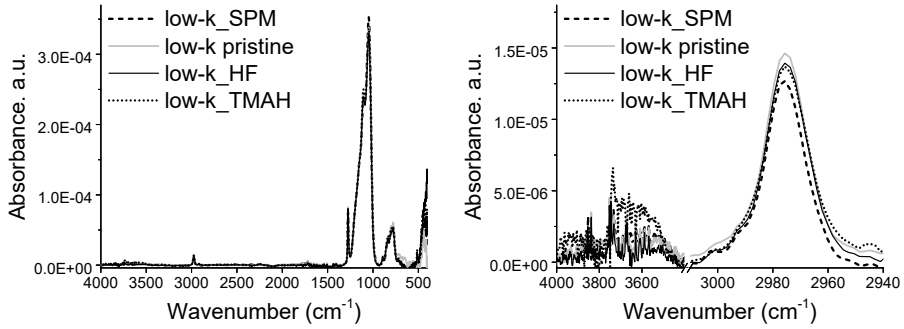

Figure 6.4: Comparison of chemical modifications after pretreatments: no additional chemical modification except for carbon depletion; TMAH shows higher water peak at 3500-4000 cm^{-1}(FTIR spectra of lowk-2.0 before and after wet pretreatment normalized by thickness)

Table 6.2: Summary of low-k 2.0 before and after various wet pretreatment

	pristine	HF	TMAH	SPM
Thickness loss, nm		<1	∼2	<1
RI increase		<0.001	<0.006	<0.005
WCA, °	103±5	69±5	43±5	46±5
k value	2.01	2.10	2.37	2.29

and Table 6.2. Certain pore densification is observed for TMAH and SPM treated samples by increased Refractive Index (RI). HF results in very high WCA therefore is not very interesting for low-k surface activation purpose. TMAH causes Si-O bonds to hydrolyze and therefore has very high etch rate and thickness loss. k value and XPS measurements indicate that TMAH is the most damaging pretreatment among the three tested. SPM is relatively more promising because it results in a WCA of 46° and thickness loss less than 1 nm.

6.2 Understanding the influence of the wet pretreatment on SAM deposition, sealing and indiffusion.

SAM growth with deposition time on SPM treated surface

SAMs are deposited on SPM pretreated surfaces and XPS measurement results indicate that there is no chlorine detected in the samples as a by-product of precursor hydrolysis or condensation. Chemically a difference in the C1s signal due to the deposition of SAM is not detected.
Figure 6.5a shows the differential FTIR spectra of SAM on SPM pretreated surface. It is obtained by subtracting the spectra after and before SAMs deposition, therefore it would reflect the chemical change in the film coming from SAMs deposition. From the spectra, the SAM layer contains OH/H_2O (3000-4000cm^{-1}), CH_2 (2925,2856,1457-1467 cm^{-1}), C≡N(2246 cm^{-1}), SiO (1015-1122 cm^{-1}) bonds. No COOH groups are formed at 1780 - 1710 cm^{-1}, indicating that nitrile groups are not hydrolysed or decomposed to carboxylic acids. From Figure 6.5b we can see a clear trend how the amount of SAMs increases with deposition time. After 5 minutes of deposition, there is already an evident increase in CH_2 peak and this is why the WCA is already 71 ° for this sample. Water entrapment is observed after 5 minutes of deposition with peak from isolated water at 3200 cm^{-1}. For this short time of deposition, the condensation of Si-OH groups is not completed and this is why there is entrapped OH/H_2O detected. While for the samples deposited at 15 minutes, the OH peak already decreased and then increased again at 24 hours because the formation of multilayer SAMs brings in some isolated SiOH groups which could not condense to Si-O groups due to lack of silanol neighbors. Normally the blue or red shift of CH_2 peak indicates the molecular arrangement of carbon backbone in SAMs. It is observed that when films are assembled on curved surfaces,

the CH_2 symmetric and asymmetric stretches are seen to broaden and shift to higher wavenumber.[129] In our experiment, CH_2 peak is located at 2925.5 cm^{-1} for all deposition samples, indicating there is little molecule arrangement difference for different deposition times.

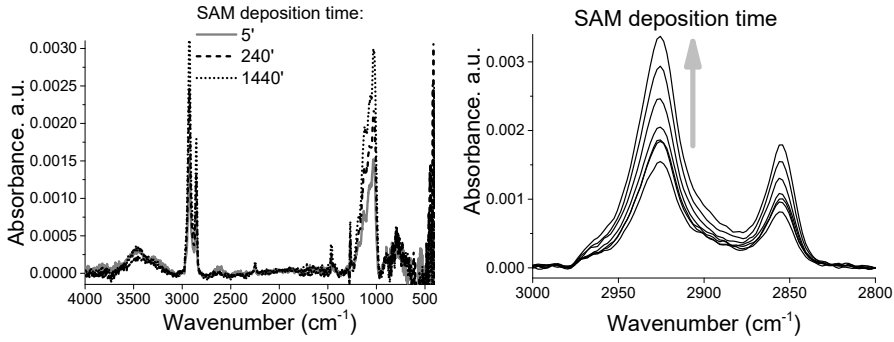

(a) (b)

Figure 6.5: On SPM pretreated surface: differential FTIR spectra obtained by subtracting the spectra recorded before SAMs deposition from the spectra recorded after SAMs deposition: (a) whole spectra; (b) details showing peaks from CH_2 bonds.

Comparing SAMs growth after different wet pretreatment

Figure 6.6a shows the thickness change for different deposition times. Thickness before and after SAMs are measured by ellipsometry (SE) and then the data is fitted with 1 layer Cauchy model. The thickness before and after deposition is subtracted and the difference is interpreted as SAM layer thickness. The negative value is because the samples are covered with water layer after pretreatment, and this water layer is not removed before SE measurement. Although the water is removed by pre-SAMs annealing, in the measurement result when the SAM thickness is lower than this water layer thickness, the thickness change is negative. The same group of samples is characterized by XRR and fitted with a 2-layers model (low-k

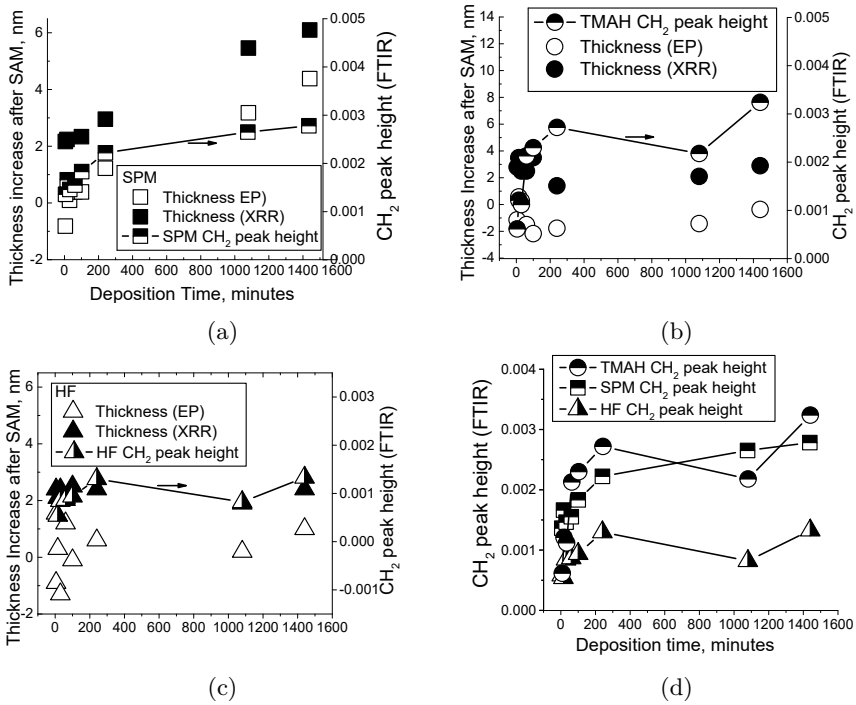

Figure 6.6: Evolution of SAMs deposited with time: SAM thickness from SE and XRR and CH_2 peak height increase from FTIR

layer and SAMs layer). There is a 2 nm difference between SE and XRR but the trend is matching. The CH_2 peak height from SAMs deposition is also given. The CH_2 peak height increase origins not only from the surface but it is a sum up of all SAMs deposited: SAMs deposited in the top surface layer, SAMs diffused into the pores (which is not reflected by SE measurements) and SAMs deposited on the backside of the Si substrate. In this section we compare the SAMs deposition kinetics for all three pretreatments. FTIR spectra (Figure 6.7) shows that SAMs on TMAH treated surface and SPM treated surface is almost twice the amount of SAMs deposited on bare SiO_2 and HF-treated surface. On TMAH treated surface, SAMs entrap more water around 3500 cm^{-1} than other pretreatments, but still have

around 6° higher contact angle than SPM pretreated sample. This might be because the entrapped water is mostly buried underneath SAMs layer, inside the pores. The surface SAMs are highly tilted so more hydrophobic carbon backbones are exposed. The FTIR spectra also indicate that the SAM layers deposited on the four surfaces are chemically not very different. Figure 6.6 compares the thickness change and CH_2 peak height of SAMs

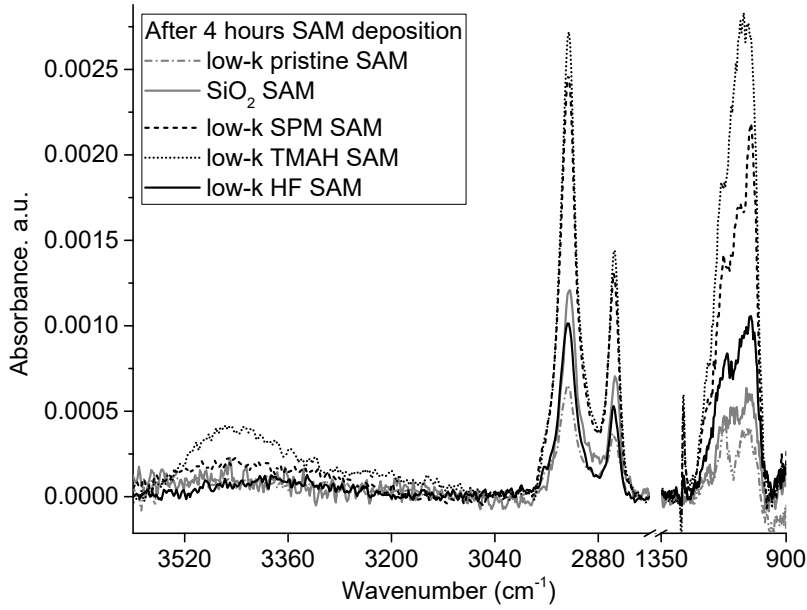

Figure 6.7: Differential FTIR spectra obtained by subtracting the spectra recorded before SAMs deposition from the spectra recorded after SAMs deposition, comparing after 4 hours of SAMs deposition on differently pretreated surfaces

deposition for all pretreated surfaces. The SAMs growth is different for the three pretreated surfaces. If SAMs are growing on a perfectly smooth SiO_2 surface, there would be 2 stages of SAMs deposition: 1. monolayer forms and density increases. In this stage, one observes an increase in CH_2 peak height while constant thickness; 2. after monolayer is formed, physisorbed multilayer starts to form by hydrogen bonds between C≡N

groups in the first layer and SiOH groups in precursor solution. On SPM pretreated surface, we see a matching between the thickness increase and CH_2 peak increase, indicating that the SAMs are growing with constant density. Unlike SPM pretreated surface, the SAMs growth on TMAH surface is with a very small thickness increase, even for 1440 mins of deposition time. But the CH_2 peak height increases fast in the first 100 minutes and then reaches a plateau. There might be two possibilities behind the limited thickness increase and fast CH_2 peak increase in the case of TMAH pretreatment: either the density of SAMs are constantly increasing within monolayer or SAMs are mostly deposited in the pores instead of top surfaces. In our case the second possibility is more probable because TMAH treatment makes a big modification to the pore walls and creates thicker damage layer than SPM as discussed in Section 6.1. On HF surface, we also see a matching between the thickness increase and the CH_2 peak increase. The initial density of silanol groups is low on the surface. In this case, SAMs are deposited with limited amount and neither thickness nor density increases as a function of deposition time.(Figure 6.6c) Figure 6.8 shows the carbon and nitrogen atom percentage measured by XPS for TMAH and HF pretreated surfaces. The 78° reflects the atoms distributed on the surface and 21° reflects the atoms distributed within top 10 nm from the surface. Assuming the concentration of Si is constant (though SAM contains 1 atom of Si), the C/Si ratio could, therefore, reflect the amount of C in the low-k and SAMs. First, we see comparable amount of carbon detected at 21° and 78° in low-k pristine (Figure 6.8). After HF pretreatment, the C/Si ratio barely changes. But after TMAH treatment, both the carbon on the surface and in the bulk is lower, more depleted on the surface and less in the bulk. For HF pretreated samples, we see a carbon increase on the surface as deposition time goes on but only little increase in the case of 21° which comes from the contribution from the bulk. For TMAH pretreated surface, at 15', both the carbon from the surface and in the bulk are almost doubled, so the SAMs are growing on both the surface

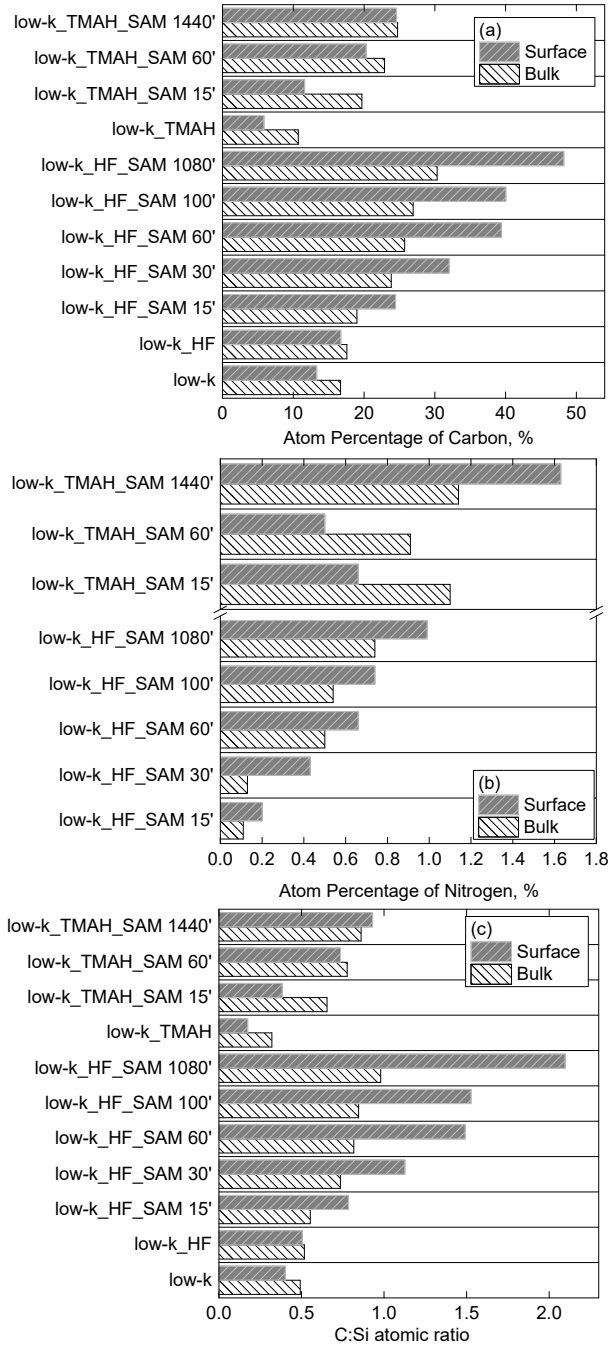

Figure 6.8: Compare atom percentage of carbon, nitrogen and C:Si ratio at 78° (Surface) and 21° (Bulk) for TMAH and HF pretreatment

and the bulk at this stage. Comparing 15' sample with 1 hr sample, we see that the for 1 hr sample, SAMs are mostly deposited on the surface. After 24 hours, the amount of SAMs deposited is not much higher than that for a 1-hour sample, which matches the trend shown in Figure 6.6b. Therefore on TMAH treated surface, the SAM deposits in a self-limiting manner. After around 4 hours, the surface is saturated with SAMs and the WCA is 75° and no more SAMs are deposited even for longer time. The trend of CH_2 group increase and thickness increase matches, therefore SAMs are not diffusing into the pores. While on SPM treated surface, after 4 hours of deposition, the surface WCA is around 69° and SAMs continuously deposit via hydrogen bonds, leading to multilayer formation. Figure 6.9 shows a

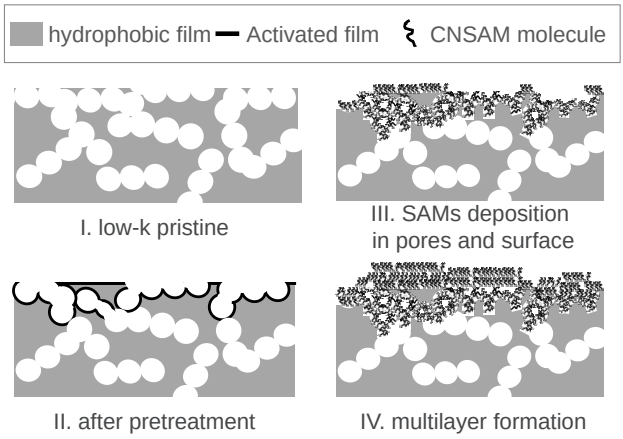

Figure 6.9: Schematic drawing of SAMs deposition kinetics on porous surface: I. low-k pristine with hydrophobic pore walls; II. after pretreatment, pore walls at the top low-k film become hydrophilic, hydrophilic layer thickness depends on the pretreatment chemistry; III. the first stage of deposition, SAMs deposit on the surface of low-k and also into the pores; IV. the second stage of deposition, SAMs is so dense on surface that diffusion into pores is blocked, or silanol groups are depleted, SAMs start to form multilayers.

summary of SAMs growth on porous and hydrophilic surfaces: I. Pore wall of low-k pristine is hydrophobic; II. After pretreatment, pore walls at the

surface and the top several nanometers become hydrophilic, hydrophilic layer thickness depends on the pretreatment for SPM treated samples, this layer is thinner than that of TMAH treated samples; III. the first stage of deposition, SAMs deposit on the surface of low-k and also into the pores; IV. the second stage of deposition, SAMs is so dense on surface that diffusion into pores is blocked, SAMs start to form multilayers. When the top surface is covered with tilted SAMs with mostly carbon backbones exposed, the SAM deposition stops. One can see that SPM is causing multi-layer formation while TMAH is not. The reason is unclear. Possibly the surface chemical composition is different after the two wet treatments which influences the overturning of SAM.

Conclusion

Three different wet pretreatments (SPM, TMAH, HF) for mesoporous low-k are studied with a target to enable SAMs deposition on the surface. With criteria of maximizing surface hydrophilicity and minimizing low-k bulk damage, pretreatment conditions for each chemistry are optimized. HF only partially converts surface functional groups to Si-OH bonds, therefore, the hydrophilicity is not ideal. TMAH etches low-k, causes thickness loss and creates thick damage layer. SPM is more promising in the sense that it shows a WCA of 46° and is less damaging than TMAH but the deposition time should be controlled to avoid multilayer formation.

Based on the pretreatment conditions optimized in the first part, low-k deposition kinetics are studied. On HF pretreated surface, the silanol groups are scarcely distributed. Monolayers are formed with increasing density but could not cover the whole surface of low-k. On TMAH pretreated surface, SAMs first deposit both on the surface and in the pores. When the density of SAM on the surface reaches certain threshold that diffusion into the pores are blocked, or the available silanols are depleted, the surface SAMs density starts to increase and then SAMs deposition

stopped because the carbon backbone is covering the surface, making it CN terminated. On SPM pretreated surface, SAMs deposited on the surface with thickness and CH_2 groups increasing simultaneously, indicate that SAMs are depositing on the surface, not in the pores and SAMs density is more constant.

Chapter 7

Plasma pretreatment for surface-confined low-k activation

Introduction

Nearly all plasma components (active radicals, UV photons, energetic ions) are able to remove terminating -CH_3 groups in low-k and replace them with hydrophilic silanols. The low-k pretreatment by aggressive and diffusive plasmas always extends into the bulk and results in bulk deposition of ALD or SAM, which dramatically degrades the low-k properties. This is not acceptable for future generation technology nodes where the highly porous and limited thickness low-k dielectrics are required. Therefore a thoughtful selection of the plasma chemistry and parameters, plus a good understanding of its interaction with porous low-k dielectrics, is needed.
In this chapter we are trying to find on conditions when CO_2 plasma

can make only the top low-k surface very hydrophilic without bulk modification. It is demonstrated that by applying positive ions one can modify the top low-k surface with limited bulk degradation. The requested conditions depend on pressure, source power and exposure time (Table 7.1). The comparative study of different plasmas shows that under optimized conditions the CO_2 plasma generating high concentration of $CO_2{}^+$ ions gives the highest surface hydrophilicity and lowest bulk damage. The possibility of surface-confined SAMs deposition by spin coating is also demonstrated.

The results presented in this Chapter are based on the following publication:
Sun, Y.; Krishtab, M.; Mankelevich, Y.; Zhang, L.; De Feyter, S.; Baklanov, M.; Armini, S. Applied Physics Letters 2016, 108 (26), 262902.
This part of work was performed at imec with support from Nano Interconnect program. The material preparation, plasma treatment were performed by Mikhail Krishtab. Dr. Mankelevich from Moscow State University and Dr. Mikhail Baklanov performed the simulation and made contributions to the understanding of the mechanism of plasma damage.My contribution includes task definition, characterization and data analysis with guidance from coauthors. I submitted this work to Applied Physics Letters, where it was accepted for publication.

7.1 Development of plasma pretreatment for low-k activation

Several plasmas were evaluated and compared on the basis of hydrophilicity and bulk modification. Figure 7.1 clearly shows that the degree of surface hydrophilization (WCA) and bulk damage (decrease of CH_3 groups concentration calculated from FTIR spectra) depends very much on the type of plasma.

The area integration of Si-CH_3 absorption peaks are normalized to film

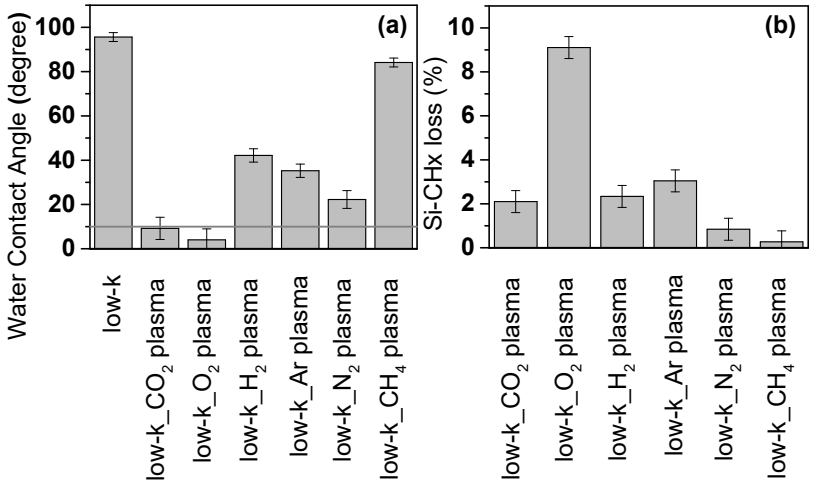

Figure 7.1: Effect of the plasma treatments from various chemistry: (a). WCA of low-k film: only O_2 and CO_2 plasmas reduce the WCA to below 10°; (b). -CH_x groups concentration loss % (calculated by the area integration from 1255 till 1375 cm^{-1} from FTIR).

thickness and therefore quantitatively reflect the relative reduction of Si-CH_3 groups in OSG films. As expected, the most hydrophilic surface with WCA $< 10°$ is obtained after O_2 plasma (Figure 7.1a), but the degree of bulk degradation (CH_3 groups loss) is also the highest in this case (Figure 7.1b). In the case of H_2 plasma, hydrogen atoms cause protonation which leads to bond rearrangement but the degree of damage is generally small.[101][130] In the case of N_2 plasma, N atom forms a CN passivation layer which protects the low-k film from further damage.[131] CH_4 plasma is used for post plasma recovery and therefore it could not provide surface hydrophilization.[132] The Ar plasma is known to cause low-k damage by ion bombardment and VUV radiation. The most interesting result comes from the CO_2 plasma: the surface hydrophilization is as efficient as the O_2 plasma (Figure 7.1a) but the degree of plasma damage is comparable to

the reducing plasmas (Figure 7.1b). Adsorption isotherm of water vapor obtained using EP shows an indication of bulk hydrophilicity after the plasma treatments (Figure 7.3).[133][134] O_2 plasma results in high bulk hydrophilicity and the water occupies 18% of the film volume at saturated vapor pressure. N_2 plasma causes the refractive index (RI) of the low-k film to slightly increase by 0.007 due to the formation of CN passivation layer while the RI change during the water adsorption test is not evident. After Ar and CO_2 plasma, only 2.5% volume of the low-k films is occupied by water at saturated vapor pressure (Figure 7.3). At the same time, no surface sealing is observed from EP measurement with toluene vapors (Figure 7.2) and therefore the water adsorption reflects bulk hydrophilicity of the studied films. It is necessary to mention that water molecules are twice smaller than toluene molecules.

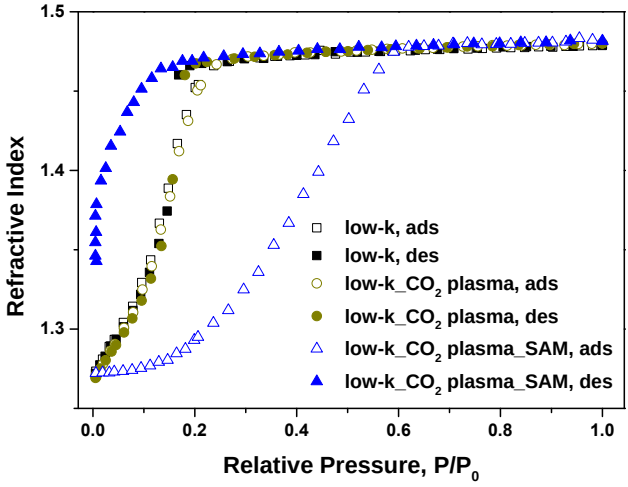

Figure 7.2: Adsorption-desorption isotherms of toluene vapors in the low-k films before and after SAM deposition. No change of porosity (initial refractive index under vacuum) after CO_2 plasma treatment and SAM deposition. It suggests that no surface sealing occurred during the exposure in CO_2 plasma and the active sites were formed only on the top surface.

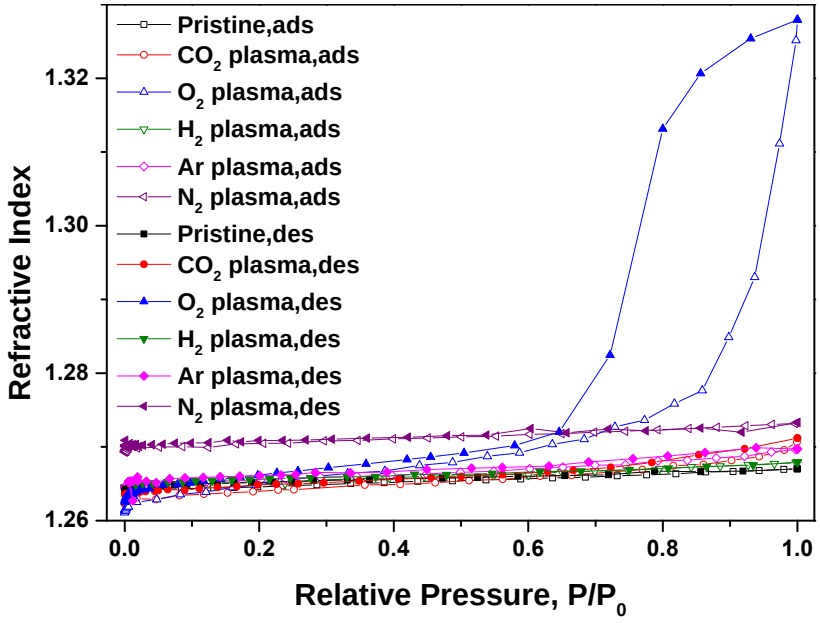

Figure 7.3: Adsorption-desorption isotherms of water vapors in the low-k film after various plasma chemistry

7.2 Understanding plasma induced low-k modifications

The efficiency of surface modification by active species and their penetration depth into the low-k bulk are mutually correlated. The surface modifying species must have the ability to remove methyl groups. However, these species could also penetrate into the bulk of low-k materials and generate internal active sites. The penetration depth of species depends on their loss probabilities, which in the case of OSG low-k materials depends on bi-molecular surface recombination and probability of their reaction with methyl groups located on the pore walls. Previously, the oxidizing (oxygen based) and reducing (hydrogen based) plasmas have been extensively analyzed for the low-k damage. It was shown that hydrogen

atoms are less reactive with CH_3 groups in comparison with oxygen radicals and the recombination coefficients of hydrogen atoms in various low-k materials are 2 - 4 times smaller than that of oxygen radicals.[104] This is the reason why the degree of surface hydrophilization in H_2 based plasma is lower than in O_2 based plasma but significantly deeper bulk modification is observed in H_2 plasma.[135] Therefore, H_2 based plasmas are not the best candidates for surface confined hydrophilization. Detailed study of low-k modification in O_2 plasma[136] shows that the initial interaction of oxygen atom with the low-k film involves multi-step extraction of carbon from Si-CH_3 groups. The successive modification of Si-O-Si structure is accompanied by occupying Si bond vacancies by O atoms and further water adsorption on the created absorption sites. To analyze the carbon extraction mechanism, the one-dimensional model based on Monte-Carlo simulation of O atoms behavior in nanoporous material was developed. This model allowed self-consistently reproducing the experimental data on the damage of CH_3-groups in the studied SiOCH films as well as O atoms loss. It was shown that the evolution of Si-CH_3 groups concentration with time under O atom flux can be described as

$$\frac{S_{\mathrm{CH3}}(t,z)}{dt} = -\beta \times F(z) \times S_{\mathrm{CH3}}(t,z)/S_{\mathrm{tot}} \tag{7.1}$$

Here S_{CH3}(t,z) is surface density of CH_3 groups at given depth z and time t of the treatment, Stot is the total surface atom density ($\sim 10^{15}$ cm^{-2}), β is reactive loss probability of O atoms and F(z)($cm^{-2}s^{-1}$) is their collision frequency per unit surface area. F(z) is proportional to the incident O atoms flux and, according to Monte-Carlo simulation,[136] it drops with z as $F(z) = F(0 < z < 2R_{\mathrm{p}}) \times exp(-1.6{\gamma_{\mathrm{loss}}}^{0.5} z/q)$, approximately. R_p is the pore radius, $q < 2R_p$ is the pore interconnectivity parameter and γ_{loss} is the total loss probability of oxygen radicals. It was shown that for recombination coefficient typical for oxygen radicals in low-k film, the depth of radicals penetration in the experimental conditions is exceeding a

few tens of nanometers.

The remaining surface concentration of CH_3 groups can be described by a first order kinetic Equation 7.1 and therefore, depends on the concentration of oxygen radicals in plasma and exposure time (Figure 7.4).

The curves presented in Figure 7.4 were calculated by using Equation 7.1 and the coefficients measured and calculated in the reference.[104] Ideally, we need to have a certain balance between the surface and bulk modification. For instance, if we need to transform 99% of surface methyl groups to silanol using initial concentration of oxygen radicals 2×10^{13} cm^{-3} (Figure 7.4 bottom), 100 s exposure to O_2 plasma is needed. However, the bulk modification is too significant. If the bulk of low-k is to be kept hydrophobic, at least 10^{14} cm^{-2} of CH_3 density in the bulk is needed. the bulk modification will be expanded up to 50 nm. Such deep modification is certainly not acceptable for modern microelectronics because SAM and ALD barrier chemistry will almost completely fill the pores.[69] If the exposure time is reduced to half (50 s), the surface density of active sites is too low to allow for the deposition of sealing layers and conformal nucleation.

These results demonstrate that even the O_2 plasma, which has been considered as the most promising for surface modification does not provide the necessary proportion between the top surface and bulk modifications suitable for modern microelectronic technology. It is necessary to find a way to increase the top surface hydrophilicity and/or to reduce bulk modification. CO_2 plasma is an example of such approach. It is known that CO_2 plasma generates CO_2^+ ions which have extremely high oxidation potential.[137][138] Susa et al.[137] have argued that CO_2^+ ions can ash equivalent amounts of carbon film with less low-k damage than that induced by oxygen radicals. On the other hand, discharging of CO_2^+ ions happens very easily after few collisions with pore wall. Ratio of CO_2^+ and oxygen radicals concentration depends on plasma characteristics (source power, pressure and treatment time) and our experimental conditions were

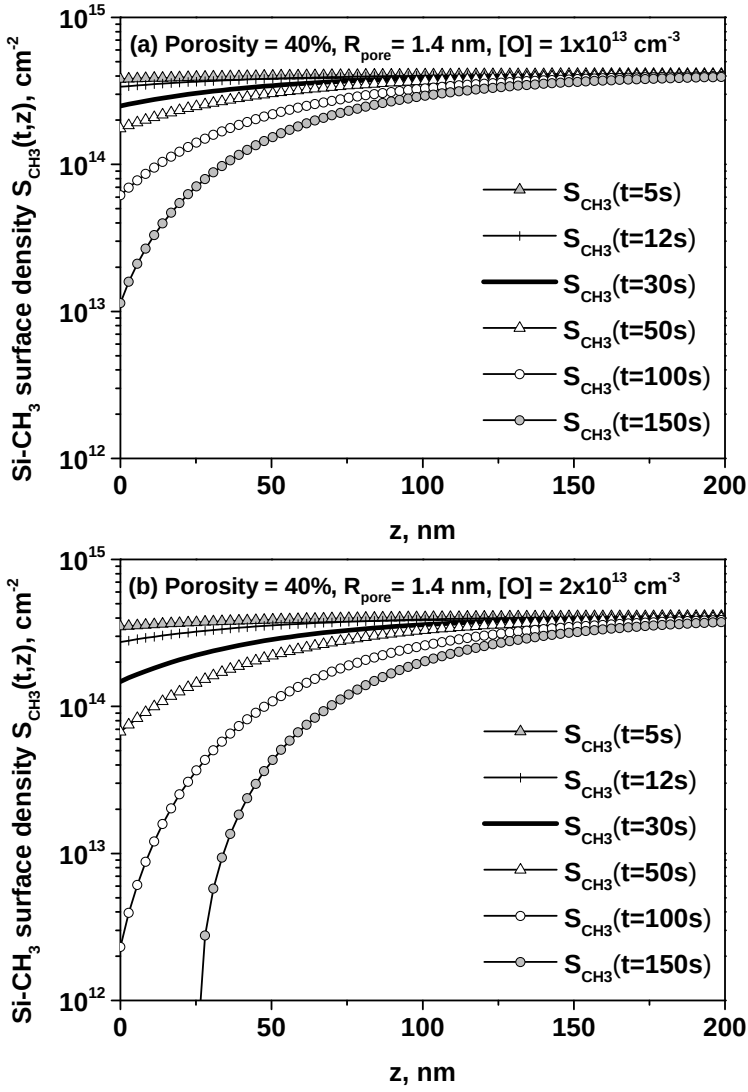

Figure 7.4: Si-CH_3 damage dynamics under O atoms flux for OSG 2.2 film, 40% porosity, pore radius R_{pore}=1.4 nm, interconnectivity hole diameter d=1.4 nm. (Top). O atoms concentration above the film $[O] = 1 \times 10^{13}$ cm^{-3}; (Bottom). O atoms concentration above the film $[O] = 2 \times 10^{13}$ cm^{-3}.

optimized to achieve the highest ratio of $[CO_2^+]/[O]$ and lowest WCA (Table 7.1). The optical emission spectra of CO_2 plasma in the optimized condition is shown in Figure 7.5.[101][139]The various peaks present in the spectra were identified.[140]

Dissociation of CO_2 and O_2 by electron impact is the main source of

Table 7.1: Water contact angle of the low-k film after various CO_2 plasma treatment conditions.

Time (s)	Source power (W)	Pressure (mTorr)	Water contact angle (°)
2	100	100	12.0 ± 5.0
3	100	100	<10.0
2	100	150	40.2 ± 4.0

O atoms in our CO_2 and O_2 plasmas, respectively, but CO_2 dissociation is less efficient, resulting in limited formation of O atoms. CO_2^+ ions could enhance the top surface modification but the depth of their bulk modification remains limited because of efficient non-dissociative neutralization of CO_2^+ ions. From gas-phase analogue reactions we can propose the following gas-surface mechanism with CO_2^+ ions and H abstraction Reaction 7.2 as one or two-step process:

$$\equiv SiCH_3 + CO_2^+ \longrightarrow (SiCH_3^+ + CO_2) \longrightarrow \equiv SiCH_2 \cdot + HCO_2^+ \quad (7.2)$$

$$\equiv SiCH_3 + HCO_2^+ \longrightarrow \equiv SiCH_4^+ + CO_2 \quad (7.3)$$

$$\equiv SiCH_4^+ + e^- \longrightarrow \equiv SiCH_3 + H \quad (7.4)$$

This reactive stage provides conditions for carbon removal with volatile formaldehyde production:[136]

$$\equiv SiCH_2 \cdot + O \longrightarrow \equiv Si \cdot + H_2C{=}O \quad (7.5)$$

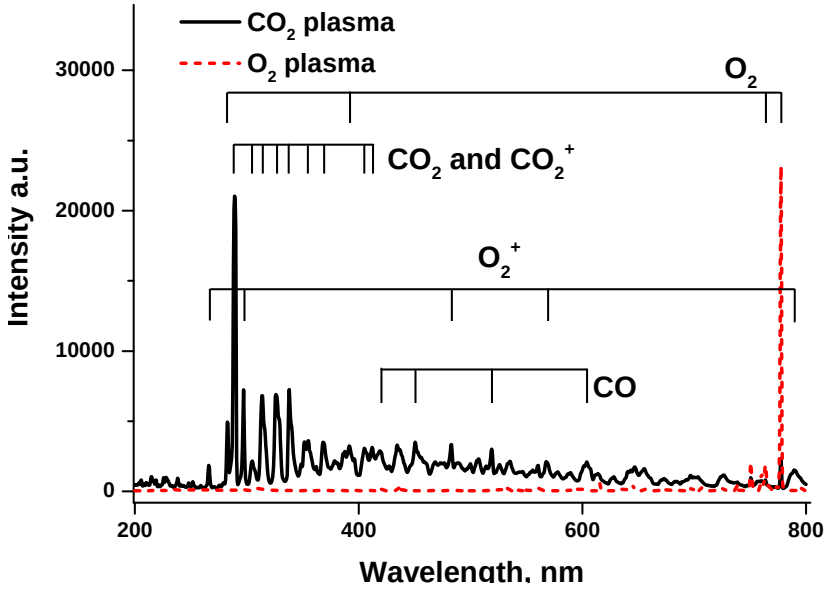

Figure 7.5: The OES spectra measured after 3 seconds of ignition shows that the major species formed in CO_2 plasma are CO_2^+ ions. The concentration of O^* radicals in CO_2 plasma is 9 times lower than the concentration in O_2 plasma. Those species react with Si-CH_3 groups and create SiOH, resulting in an increase of surface hydrophilicity.

$H_2C{=}O$ can further be oxidized and form water, CO and CO_2. The unsaturated silicon bonds in ($\equiv Si^*$) easily form silanols during the reactions with etch byproducts and during the storage in air.

When the exposure time is short, most of formed O radicals are consumed in the reactions with activated carbon compounds such as $SiCH_2$ and $SiCH_x^+$. The situation is becoming different when the exposure time is elongated. The low-k surface is becoming carbon free and the released O radicals have chance to diffuse into the bulk of low-k films and the difference between O_2 and CO_2 plasmas become smaller.[141] This is the reason why short plasma exposure in CO_2 plasma is a key for surface limited low-k modification.

To further check the efficiency of plasma surface activation, the density of silanol groups at the surface and probability of their formation in the

low-k bulk is qualitatively examined by SAM deposition. The short CO_2 plasma treatment does not change the pore size or porosity in the bulk of the low-k layer (Figure 7.2). The refractive index before and after CO_2 plasma stays the same, which also indicates that there is no observable film densification. After SAM deposition, a hysteresis between adsorption and desorption curve indicates a partial sealing of the porous dielectrics by SAM layer although the measured effective refractive index suggest that no SAM deposition inside of low-k films occurred.[69] In our experiment, the effective refractive index of the low-k film increased from 1.261 before SAM to 1.263 after SAM. The RI change is in agreement with the results of k-value measurements: a Δk as low as 0.03 is measured after SAMs deposition, which indicates that SAMs did not deposit inside the low-k film. Compared to the reference sample before SAM deposition, the film after SAM deposition showed a 2 nm thickness increase based on the ellipsometry measurements, undetectable CH_x increase according to FTIR, 0.03 k value change and an increase of water contact angle from less than 10° to 56°. These observations suggest that a SAM monolayer, dense enough to provide the partial sealing of the pores at the surface, was formed on the mesoporous low-k material.

Conclusion

In summary an approach enabling the surface-limited activation of low-k dielectrics was explored. It is demonstrated that CO_2 plasma is the most effective plasma in creating hydrophilic surface without deep low-k damage. Such observation was attributed to high oxidation potential of CO_2^+ ions predominantly formed in the plasma. The high concentration of silanol groups and their localization at the very surface of the porous low-k layer was showcased by deposition of SAMs. We believe that the proposed idea and approach can play a substantial role in enabling selective deposition

on top of low-k films for future technology nodes.

Chapter 8

Pore stuffing for surface-confined low-k activation

Introduction

The patterning process by plasma etching would cause electronic degradation on low-k material and increase k value. Frot et al. patented a method to address this issue.[76][77] The concept is to fill the pores with a sacrificial polymer so that the porous material is temporarily converted into a dense material. They name this process as the "post porosity plasma protection" (P4). In later works of Zhang et al., it is called pore stuffing approach (referred to as "PS" in this chapter).[78] The details of this approach are introduced in chapter 3.

For low-k material with pore diameter larger than 3 nm, the SAM precursors might diffuse into the pores if the plasma is too damaging.

Therefore we see this pore stuffing method as a potential way to introduce silanol groups during etching without degrading low-k. By protecting the low-k material with polymer during plasma etching, the reaction sites (-OH) groups for SAMs deposition can be confined to the top surface. Consequently, the confinement of SAMs can be realized. In this chapter, the pore stuffing approach during plasma etching helps to limit the hydrophilic layer thickness.[79] With this approach, the SAMs distribution inside the pores is confined to the surface and the sealing ability against tetrakis(dimethylamino)titanium (TDMAT) ALD precursor has been demonstrated. Table 8.1 lists the abbreviations used in all figure legends.

Table 8.1: Surface Treatment Codes and Descriptions

Treatment code	Treatment description
PS	Pore stuffing with PMMA
CF_4	CF_4 plasma etching
US	Thermal annealing to remove PMMA
CL	Wet cleaning to remove post-etch residues
APTMS	Depositing of APTMS
CNSAM	Depositing of CNSAM
TiN	Depositing TiN via ALD

The results presented in this Chapter are based on the following publication:

Sun, Y.; Levrau, E.; Zhang, L.; Geypen, J.; Meersschaut, J.; Franquet, A.; Le, Q. T.; de Marneffe, J.-F.; Bender, H.; Struyf, H.; Detavernier, C.; Baklanov, M.; De Feyter, S.; Armini, S. Microelectronic Engineering 2015, 137, 70–74.

This part of work was performed at imec with support from Nano

Interconnect program. Dr. Levrau deposited the metal barrier and measured XRF. Dr. Zhang did the pore stuffing processing. Dr. Geypen measured TEM. I developed the SAM deposition protocol, performed the characterizations, analyzed the data with guidance from coauthors. I submitted this work to Microelectronic Engineering, where it was accepted for publication.

Experiment

PECVD low-k with a k value of 2.0 is used in this chapter. The samples were split into two groups: samples from the first group (referred to as "Reference" group) were etched with CF_4 plasma in a capacitively coupled plasma (CCP) chamber; samples in the second group (referred to as "PS" group) were treated with pore stuffing (Section 3.2). Patterned samples were prepared by depositing a dense SiC hard-mask on top for the p-OSG low-k, followed by the deposition of spin-on carbon (SOC) and spin-on glass (SOG). After conventional lithography targeting 180 nm pitch line/space structures, SOG-SOC hard-mask opening and trim followed by SiC etch allowed to reach pre-patterned structures of approximately 30nm/150nm line/space. Low-k etch was then performed using a CF_4 plasma. For all samples, a wet cleaning is performed after CF_4 plasma to remove etching residuals (Detailed in Appendix B). CNSAM and APTMS are deposited by dip coating. TiN metal barrier is deposited by plasma enhanced ALD. Figure 8.1 shows detailed processing procedures for the two groups.

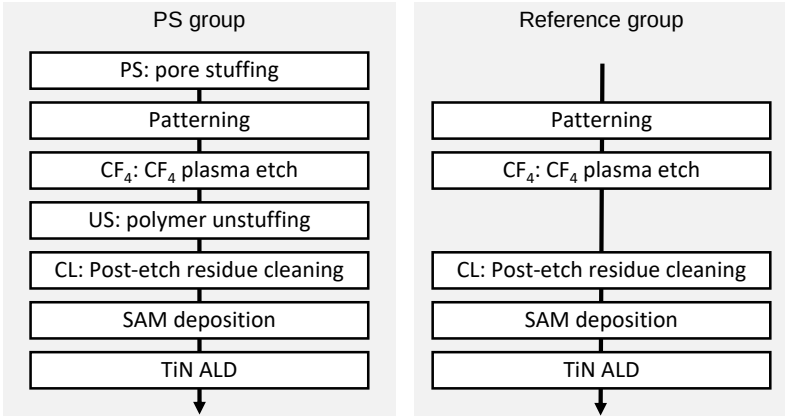

Figure 8.1: Processing procedures of processing steps. TOF-SIMS, FTIR, WCA, k-value, thickness were measured on blanket samples; TEM image were recorded on patterned samples.

8.1 Pore stuffing approach and damage mitigation

After CF_4 plasma treatment, the CH_3 groups are removed by highly reactive plasma species from the surface and the plasma induced damage is quantified as the loss of CH_3 groups, which is reflected in the reduction of the $SiCH_3$ peak intensity in the FTIR spectra as compared to low-k pristine (Figure 8.2a).[142] In order to mitigate the plasma induced damage, the PS approach was implemented by applying a "polymer stuffing" treatment to the porous material before its exposure to CF_4 plasma: A sacrificial polymer fills the pores and stops most of the plasma species from diffusing into the pores. After the plasma etching, the polymer was removed. Therefore, after the treatment, only the unprotected top surface is hydrophilic while in the bulk low-k the pore walls are still hydrophobic. Via this approach, Si-CH_3 depletion has been alleviated by 7% with respect to standard etching by CF_4 plasma (Table 8.2). This

result agrees well with the k-value measurement: the PS group shows 0.62 lower k-values as compared with the Reference group. One might notice that the WCA on PS groups are higher (34°than the Reference group (10°). There might be more carbon on the surface of PS samples than Reference group. Though our current ToF-SIMS data could not verify this because the carbon fluorides from etching residuals also contribute to carbon content. Another possible reason is, during thermal unstuffing procedure, some fragments from PMMA polymer might chemically absorb on low-k surface and blocked silanol groups.

Time-of-flight secondary ion mass spectrometry (ToF-SIMS) elemental depth profiling indicates that the PS samples show a low fluorine content after etch, which is an indication of lowered diffusion of fluorine radicals into the bulk.[143] In the Reference group, the fluorine signal is high throughout the whole depth of the low-k film (above the saturation level of the detector) while in the PS group, the fluorine signal is close to the background level (i.e. detected in the pristine low-k layer) with only slightly higher intensity confined to the top 10nm of the etched film (Figure 8.2b). High-energy photons generated in plasma are damaging to low-k material as well. The photons under vacuum or low pressure environment can propagate, while they are normally blocked by the air. They can dissociate chemical bonds like Si-C, therefore it is damaging for low-k. Although the pore stuffing approach can avoid the diffusion of radicals and blocking ion bombardments, it is less efficient in blocking the VUV damage. A recent study by El Otell et al. ([144]) showed that CF_4 emits VUV mainly in the wavelength of 156,164 and 204 nm. Jinnai et al. studied the VUV from etching plasma ([145]) and they found that VUV damage from the photons in CF_4 plasma can cause low-k damage. Zhang et al. studied the possibility of avoiding VUV damage by pore stuffing approach. They found that pore stuffing polymers can alleviate the VUV damage from Ar/CF_4 plasma by around 50% but can not totally avoid this damage.[146] Therefore the pore stuffing approach has certain limitations in terms of

surface confined-activation.

Table 8.2: Properties of low-k films: pristine film, Reference group after plasma treatment and cleaning, PS group after un-stuffing and cleaning

	Low-k pristine	Reference	PS
Water contact angle, °	96.60	10.90	34.93
Refractive index	1.2285	1.2492	1.2457
k-value	2.02	2.82	2.20
Si-CH_3 peak height*	6.7E-5	5.8E-5	6.3E-5

* normalized by thickness

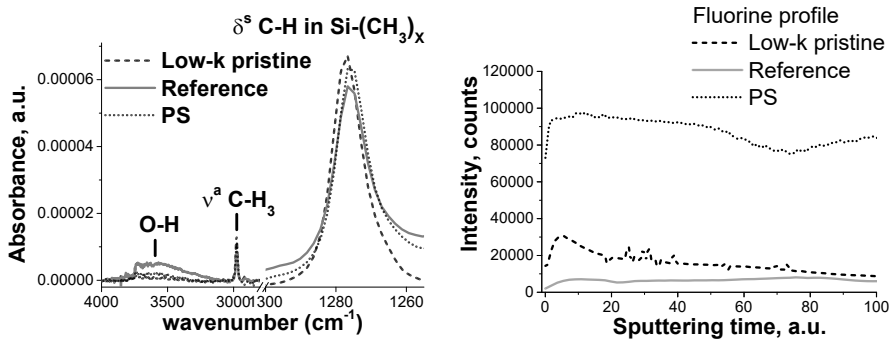

(a) (b)

Figure 8.2: Effects of pore stuffing treatment: (a) FTIR spectra of low-k before and after plasma and cleaning treatment. All the spectra are normalized to the thickness of the low-k film. The PS treatment allows reduction of the Si-CH_3 groups depletion (peak located at 1276 cm^{-1}) and reduced water content evidenced by the lower peak height of the -OH band in the region from 3010 to 3900 cm^{-1}). (b) TOF-SIMS profile of fluorine as a function of sputtering time (depth profile).

8.2 SAM pore sealing evaluation in combination with metal barrier precursor

After SAMs deposition, the water contact angle increased from below 35° (as given in Table 8.2) to 50±2° and 70±2° for APTMS and CNSAM, respectively. The contact angles are close to the previously reported values, indicating successful SAM deposition in both groups.[114] The amount of SAMs deposited is characterized by the intensity of the CH_2 peak increase in the FTIR spectra. For the Reference group, the amount of SAMs deposited is 2-3 times larger than that of the PS group, which is an evidence that the PS treatment results in thinner hydrophilic layer and accordingly lower depth of SAM penetration (Figure 8.3). k-value measurements indicate that the APTMS showed only 3% increase of k-value in the PS group. However, CNSAM caused 16% increase of k-value for the same group (Figure 8.4). This difference could be attributed to the fact that the cyano-group has a higher dipole moment than the amino-group. [147] This is why APTMS SAM is selected for further pore sealing study over CNSAM.

After TiN deposition, the diffusion of TDMAT precursor inside the pores was characterized by RBS (Figure 8.5). For samples sealed with SAMs, RBS spectra collected at 135° showed a sharp peak between 1.12 and 1.2 MeV, which is assigned to Ti atoms. At the same time for the samples without SAMs, a broad peak at 1.12 MeV with a tail extending towards lower energy implies the presence of Ti atoms inside the low-k.[29] Transmission electron microscopy (TEM) images of patterned samples confirmed that the selected APTMS-SAMs stopped the penetration of TDMAT precursor (Figure 8.6a). For the samples without sealing, Ti atoms penetrate for 10 nm into the low-k film. This barrier precursor penetration depth is the same as found on PS and Reference samples, indicating for this barrier deposition, the precursor diffusion does not depend on the low-

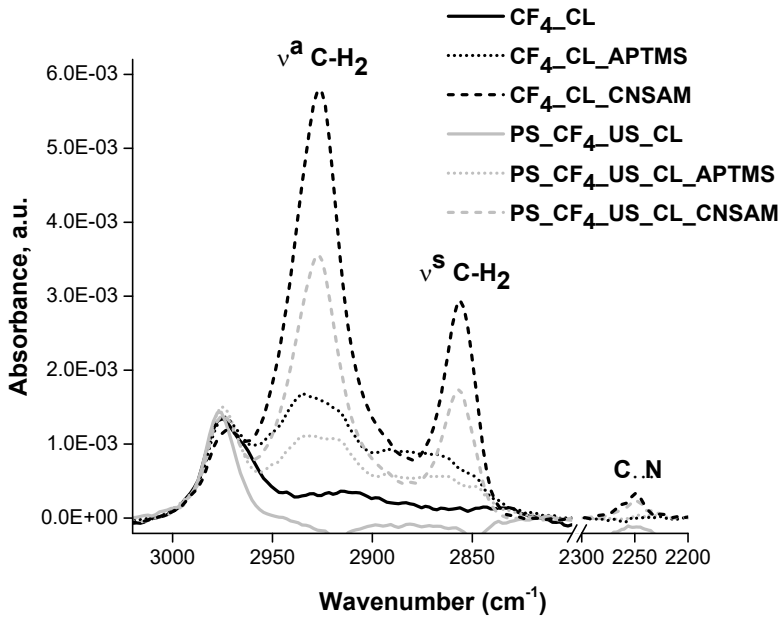

Figure 8.3: Differential FTIR spectra obtained by subtracting the spectra recorded before SAMs deposition from the spectra recorded after SAM deposition.

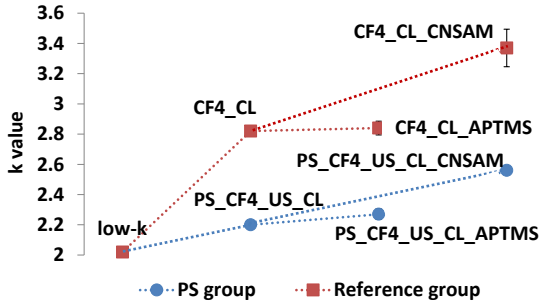

Figure 8.4: k-value after various treatments

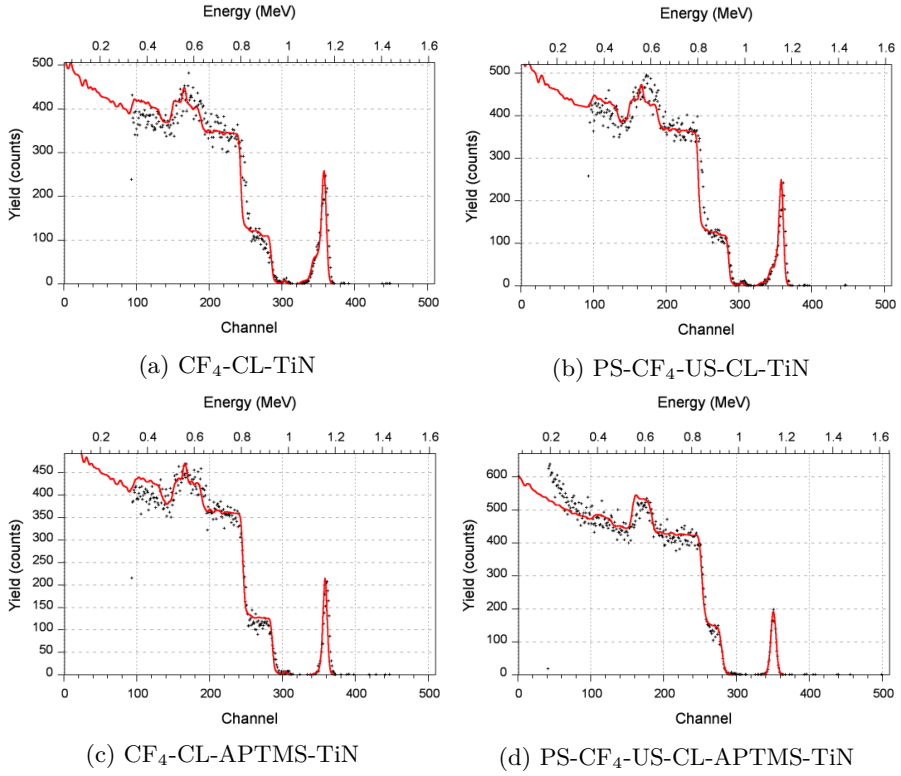

(a) CF_4-CL-TiN

(b) PS-CF_4-US-CL-TiN

(c) CF_4-CL-APTMS-TiN

(d) PS-CF_4-US-CL-APTMS-TiN

Figure 8.5: RBS spectra of Ti diffusion in porous low-k

k bulk hydrophilicity. Ti map obtained by energy-filtered transmission electron microscopy (EFTEM) measurement confirmed the reduction of Ti penetration in the low-k film after the SAMs sealing treatment.

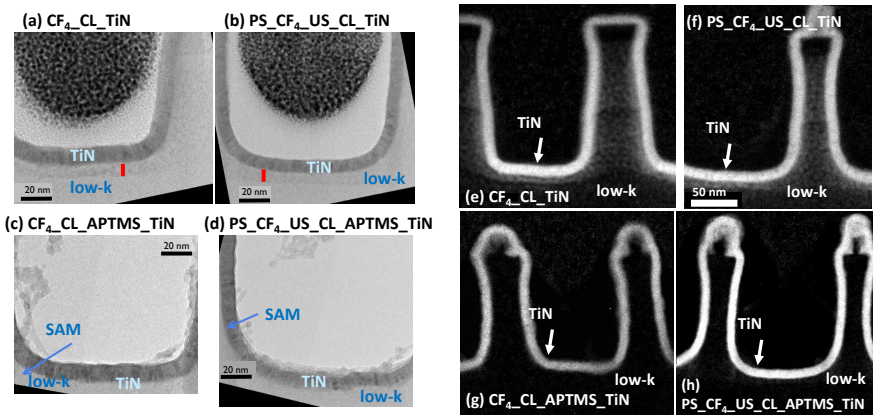

cross-section TEM

EFTEM elemental maps

Figure 8.6: Left: TEM images on the cross-section of patterned samples after various processing sequences and TiN deposition. Ti speckles are observed for the samples (a) and (b) while they are below the TEM detection limit for samples sealed by SAMs ((c) and (d)); Right: EFTEM elemental maps for Ti.

Conclusion

In order to integrate k=2.0 p-OSG dielectric materials with pore diameter larger than 3 nm, the combination of pore stuffing, SAMs pore sealing and ALD metal barrier was engineered to achieve sealing with minimal plasma induced damage. Firstly, a PS integration approach was implemented using PMMA as a sacrificial polymer (pore stuffing). Pore sealing efficiencies on PS samples were benchmarked against a conventional interconnected patterning flow (no stuffing). FTIR and k-value measurements indicate that the pore stuffing step effectively confined the hydrophilic layer to the top surface and reduced diffusion of SAMs into the pores. APTMS outperforms CNSAM by showing lower k-value. TEM and RBS results showed that after a 10 nm metal barrier is grown on the APTMS, the low-k surface is sealed and metal penetration is below detectable limit.

Chapter 9

Conclusions and outlook

The research on low-k pore sealing has been attracting attention for several years. However, with the downscaling of the feature size and the increase in pore size, the sealing becomes more and more challenging. In comparison to the traditional way of pore sealing with inorganics and plasma, this dissertation aims to leverage the chemical selectivity of self-assembled monolayers (SAM) and to achieve surface-confined deposition, which is made possible by surface-confined activation. With a target of maximizing surface hydrophilicity and minimizing low-k bulk damage, four different pretreatment conditions are studied and benchmarked. For each pretreatment, SAMs and metal barriers are deposited to evaluate the effectiveness of the activation.

9.1 Conclusions

Conclusions on the study of the relevance of surface confined pretreatment
We investigated the correlation between the extent of the plasma damage, the pore size and SAMs pore sealing and diffusion in porous dielectrics

with k values of 2.0, 2.5 and 3.0, which correspond to 1.7, 0.7 and <0.5 nm pore radius, respectively. O_2 and He/H_2 plasmas were evaluated. Due to the intrinsic hydrophobic nature of the low-k dielectrics, only a negligible amount of silane precursors is chemically grafted on the as-deposited materials. Both available surface binding sites and low-k pore radius dictate the distribution of the silane molecules in the porous films. The threshold pore diameter for SAMs' indiffusion is 1.4 nm, which is comparable to the chain length of the CNSAMs precursor. When the pore diameter of the pretreated low-k material is higher than this value, the SAMs' indiffusion into the pores is driven by the reaction between the silane precursors and the silanol groups. In this case, the SAMs distribution follows the in-depth profile of the silanol groups in the pores. For the O_2 plasma treatments, the extent of low-k damage is dictated by the diffusion of the oxygen radicals into the pores, while the plasma-generated vacuum ultraviolet (VUV) light plays a critical role in the low-k modification induced by He/H_2 plasma. Our observations lead to technologically-relevant conclusions as to the enabling of a surface-limited pore sealing solution. The application of O_2 plasma is the preferred surface-modification route for microporous materials, because the micropores limit the depth of radical penetration. On the other hand, He/H_2 plasma can generate VUV light and is more suitable for mesoporous materials due to its largest photo absorption cross section. This conclusion is in agreement with some recent findings related to the modification of ultra low-k films by He/H_2 plasma for atomic layer deposition (ALD) deposition of TiO_2.[120]

Conclusions on surface activation with evaporated Si

The silicon evaporation process does not cause $Si\text{-}CH_3$ depletion in low-k material. Although the increase of thickness brings up k value of the whole stack. XRR measurements show an increase of electron density on 1 nm silicon-pretreated samples after SAM deposition. Therefore this pretreatment mitigates but not totally eliminates SAMs diffusion. The

possible reason is the silicon atoms diffusion into low-k and the introduction of silanol groups inside. On 1nm Si pretreated sample, higher electron density after CNSAM is observed as compared with APTMS. It might be because APTMS forms inter- and intra-molecule hydrogen bond and form a good sealing layer, blocking the self-diffusion of SAM precursors. While the sealing of CNSAM is not as good and SAM precursors can still penetrate even though there is already a layer of SAM on the surface. FTIR measurements show that more SAM molecules are deposited on 1 nm Si evaporated low-k than on SiO_2 reference, possibly due to diffusion, which is in agreement with the XRR measurement results. For the low-k 2.0 material fabricated with pretreatment, self-assembled monolayer (SAM) sealing and TiN ALD process, RBS measurement is performed to detect Ti distribution in the low-k bulk. For the sample without the SAM sealing process, Ti atoms diffused from the top layer into the OSG film for all pretreatments tested. While no Ti atom diffusion is detected for the samples with SAM sealing treatment.

Conclusions on surface activation with wet pretreatment

Three different wet pretreatments (SPM, TMAH, HF) for mesoporous low-k are studied with a target to enable SAMs deposition. HF only partially converts surface functional groups to Si-OH bonds therefore the hydrophilicity is not ideal. TMAH etches low-k, causes thickness loss and creates thick damage layer. SPM is more promising in the sense that it shows lower WCA (46°) as compared with HF and TMAH and is less damaging than TMAH but the SAM deposition time should be controlled to avoid multilayer formation.

Based on the pretreatment conditions optimized in the first part, SAM deposition kinetics are studied. On HF pretreated surface, the silanol groups are scarcely distributed. Monolayers are formed with increasing density but could not cover the whole surface of low-k. On TMAH pretreated surface, SAMs first deposit both on the surface and in the

pores. When the density of SAM on the surface reaches certain threshold so that diffusion into the pores is blocked, the surface SAMs density starts to increase. Eventually SAMs deposition is stopped because the carbon backbone is covering the surface, making it hydrophobic. On SPM pretreated surface, SAMs deposited on the surface with thickness and CH_2 groups increasing simultaneously, indicating that SAMs are depositing on the surface and not in the pores, and in this case, the SAMs density is not increasing for the deposition times tested.

Conclusions on surface activation with CO_2 plasma
It is demonstrated that CO_2 plasma is the most effective plasma in creating a hydrophilic surface without deep low-k damage. Such observation was attributed to high oxidation potential of CO_2^+ ions predominantly formed in the plasma. The high concentration of silanol groups and their localization at the very surface of the porous low-k layer was showcased by deposition of SAMs.

Conclusions on surface activation with pore stuffed
In this chapter, the combination of pore stuffing, SAMs pore sealing and ALD metal barrier was engineered to achieve sealing with minimal plasma induced damage. FTIR and k-value measurements indicate that the pore stuffing treatment efficiently confined the hydrophilic layer to the top surface and reduced diffusion of SAMs into the pores. APTMS outperforms CNSAM by showing lower k-value due to its lower dipole moment in the tail group. TEM and RBS results showed that after a SAM layer is grown on the low-k material, the low-k surface is sealed and metal penetration is below the detectable limit.

9.2 Summary of pretreatments

Table 9.1 summarizes the findings on the surface pretreatments studied in this work. The wet pretreatments can not bring water contact angle sufficiently low without damaging low-k. The silicon evaporation approach can not deliver a film with good uniformity and conformity. The post-evaporate oxidation can not efficiently convert silicon to SiO_2. Therefore the water contact angle is also not very low after this treatment. The pore stuffing approach is complicated with many procedures. The unstuffed polymer fragments might deactivate some of the active sites. And the PMMA polymer we used in this work can only block 50% of VUV. Considering the target of this work (maximizing surface silanol groups while minimizing k value change), the CO_2 plasma shows the most satisfying result. For all the pretreatments tested, SAMs can successfully seal the porous low-k. No metal barrier precursor diffusion is detected on sealed samples.

Table 9.1: Comparing figure of merit for different pretreatments

Pretreatment	Δk ($k_{initial}$)	Si-CH_3 loss, %	WCA, °
SPM	0.28 (2.01)	6.2	46
TMAH	0.36 (2.01)	8.0	43
HF	0.09 (2.01)	4.2	69
CO_2 plasma	0.03 (2.23)	2.0	< 10
pore stuffing	0.18 (2.02)	6.0	35
silicon evaporation (1nm)	0.07 (2.14)	4.7	37

9.3 Proposed future research

The current work was focused on one of the key aspects of highly porous low-k materials integration into the structure of on-chip interconnects – surface confined activation for the purpose of pore sealing. The focus is mainly on

how to pretreat low-k in a way that the activated sites are confined to the surface. By confining the -OH groups to the surface, the surface-bulk selectivity in SAMs deposition can be realized. Despite the rather broad range of solutions extensively discussed in the results section of this thesis, there are many other promising approaches and scientific challenges which remain beyond the scope of this work and may be a subject of future research.

One of the immediate questions which are not yet fully addressed is related to the optimal type of SAM precursor for the pore sealing purpose. As mentioned in Section 2.2.1, there are 3 parameters in the structure of SAM precursor: head/anchoring group, chain length, tail group. It would be interesting to study the impact of the number of hydrolysable groups at the anchoring end of the SAMs molecule on pore sealing efficiency (monodentate, bidentate and tridentate for 1,2 and 3 hydrolyzable groups). The organosilane used in this work has three anchoring groups (Si-X_3). The reason why we choose this SAM precursor is if all three anchoring groups are successfully hydrolyzed and form covalent bonds with low-k, optimal thermal stability and adhesion would be achieved.[148] Though in other studies, it shows that the three anchoring groups might not all attach to low-k. Instead, they can form cross-linking networks. It is reported in the literature that lateral cross-linking via silanol groups condensation takes place between adjacent SAM molecules to form a densely packed monolayer.[106] The drawback of three anchoring groups is that, it would result in the formation of dimer and trimers, agglomerates, or multilayer and messy layer[149]. By using precursors with less anchoring groups or even mono anchoring sites, the agglomeration and messy layer can be mitigated. Figure 9.1 shows the situations discussed. Currently the sealing mechanism of SAM is still not clear, it can be situation I or situation II. Situation III is excluded because a monolayer thickness is measured. By experimenting with monodentate groups, more insight could be gained into the sealing mechanism of whether it is sealing via mechanism I or

mechanism II.

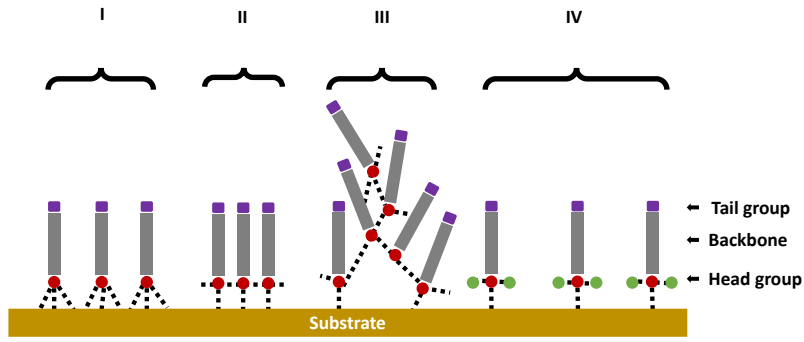

Figure 9.1: Influence of anchoring groups. I. Precursors are tridentate. All anchoring groups are attached to low-k; II. precursors are tridentate. Anchoring groups form a cross-linked network; III. Precursors are tridentate with anchoring groups attached to another precursor, resulting in messy layer formation. IV. Precursors are monodentate. Anchoring groups are attached to the surface. But SAM chains are more scarcely located due to steric effects.

A much wider field to explore is the tail groups of choice. In this respect, using bulky/branched SAM molecules looks appealing. Since the surface of low-k is porous and therefore very rough, the chance that linear SAM precursors align under Van de Waals forces and form crystalline 2D structure is low. Therefore linear SAM precursors are not necessarily better than branched ones. It would be interesting to find a precursor with branched or umbrella-shaped structure. Another direction is to replace amino tail with other functional groups like epoxy. The epoxy rings can be opened by water (affording the corresponding diol), or by nucleophilic attack by –COOH or $–NH_2$ containing molecules, and a bond between the epoxy and the organic molecule can be formed.[150] Therefore this tailing group might offer more possibilities for subsequent deposition. It would also be interesting to explore precursors which can crosslink under UV-exposure. [151][152]

Another interesting point to study would be the interaction of SAMs used for pore sealing with the actual metal composing the conducting lines in the interconnects, i.e. examine the viability of the low-k integration scheme when the metallic diffusion barrier is omitted. In this case, the ability of SAMs to prevent the metal oxidation and metal ion diffusion inside the low-k dielectrics is of paramount importance. Some of the SAMs/low-k combinations have been already shown to provide improved electrical reliability due to suppressed copper in-diffusion (e.g. thiols, porphyrins).[153] However, there was no systematic study on this subject performed so far. The possibility to skip the metallic barrier in the low-k integration scheme would bring remarkable improvement of RC performance as a result of overall reduced line resistivity. Though in this case the adhesion between SAMs and the metal line would be another challenge.

Finally, one more aspect about the SAMs applications in interconnects should be mentioned. As the feature sizes get closer to the dimensions of several tens of atoms, the selective processes start gaining more attention from the industry.[154] In the context of pore sealing of organosilica low-k dielectrics the selectivity issue arises due to exposure of both etched low-k side-walls and the metal surface of the previous metallization layer (at the via bottom) during the SAMs deposition (Section 1.3, Figure 1.6). Lack of selectivity results in attachment of SAMs molecules to the metal and therefore in increased via resistance. Though in this work the absolute selectivity of dielectric over metal was assumed, in the real applications, when the metal surface may be oxidized, approaches directed towards this ideal selectivity are to be developed. Studies in this area include Kayaba et al. [52] and Bent et al.[155]. The selectivity can either come from intrinsic or post-SAM cleaning. The concept of intrinsic selectivity would be first to deposit carbon-terminated thiols SAMs, which is selectively deposited on Cu over low-k. Then deposit organosilanes on low-k. Leveraging the different thermal stability of thiols and organosilanes, the thiols can be

removed by heating up the structure. Post-SAM cleaning can be achieved based on the higher chemical stability of SAMs on dielectrics over metals.

Appendix A

Health, safety and environment (HSE)

Consciously dealing with safety and environmental aspects is one of the keystones during the education program at the KU Leuven's Department of Chemistry. This encompasses the acquisition of structural knowledge and insights in the properties of chemicals which are fundamental to evaluate HSE standards.Daily exposure to potential risks is inevitable and therefore a stringent laboratory safety standard is mandatory. The acquired level of attentiveness concerning HSE was of great importance during the execution of laboratory experiments in support of this thesis. Experiments were evaluated in advance by means of thorough risk assessments. Precautions were taken to ensure the workplace was safe at all times. The most important risks are highlighted here below:

Piranha: *Piranha solution reacts Violently with organic matter.* It should not be combined with significant quantities of organic material and it should also not be stored for long periods of time. Piranha solution should be contained in glass or Pyrex containers. Piranha will melt plastics. The

hydrogen peroxide component should typically be kept to below 30%, never to exceed 50%. Adding any acids or bases to piranha or spraying it with water will accelerate the reaction.

HF: Hydrofluoric acid (HF) has a number of physical, chemical, and toxicological properties that make it especially hazardous to handle. Fluoride ions form insoluble salts with calcium and magnesium in bodily tissue. Use chemically compatible containers, such as those made from polyethylene or Teflon. Keep containers closed to minimize exposure and prevent etching of fume hood glass from HF vapors.

Toluene: Toluene can cause irritation to the eyes, throat, lungs and skin. Breathing in toluene vapours can cause drowsiness, dizziness, headache, sickness and memory problems. Deliberately breathing large amounts of toluene (e.g. from glue-sniffing) can cause permanent damage to the nervous system, coma, heart problems and even death.

Methanol: Methanol is toxic and flammable. Methanol can cause poisoning, systemic acidosis, optic nerve damage and central nervous system (CNS) effects.

SAM precursors (CNSAM, APTMS, DETA): SAM precursors used in this work are organosilanes. This type of compounds is flammable and toxic. Contact with skin and eyes should be avoided. The chemicals should be kept in sealed containers, preferably in an inert ambient, and in a well ventilated fridge.

Metal barrier precursors: metal barrier precursors used in this work are highly flammable. Contact with water should be avoided. Contact with skin and eyes should be avoided. The chemicals should be kept in a tightly closed container. The container should be in a dry and well-ventilated place.

Nanoparticles:For silicon wafer preparation, such as wafer cleavage and back side scratching, particles hazard could be a major health issue. In this case, googles and mouth mask is obliged.

Appendix B

Supplementary methodology

In this chapter, additional details for material preparation, processing and methodology are introduced, which are used, in a way that not very different than general practices every lab is following. This chapter includes: SiO_2 wafer preparation, metal barrier deposition, UV-ozone cleaning, and characterizations like ToF-SIMS, XPS, TEM and XRR.

Material preparation, deposition and processing

SiO_2 —Silicon substrates with a 2 nm native SiO_2 film were used as a nonporous reference which experienced the same silanization procedure as the low-k samples. Native oxide references were selected because of their higher surface silanol density, as compared with thermal oxide.[156]
TiN ALD —The TiN films were deposited from the TDMAT precursor at 120 °C, with either NH_3 as reactive gas for thermal ALD or N_2 plasma as reactive gas for PEALD. For each ALD cycle, the exposure time to the precursor was 10 s and the reactive gas pulse time was 6 s. The samples were exposed to different cycles of the ALD process. The number of cycles

depends on the desired thickness, normally 80 cycles result in an expected TiN film thickness of 10 nm.[157]

MnN CVD —A 3 nm MnN barrier was deposited by $(EtCp)_2Mn$ CVD in a 300mm AMAT Endura platform.[66] Before the CVD, the wafers were degassed under 110 °C or 300 °C under vacuum.

UVO cleaning —Before silanization, the silicon dioxide reference samples was cleaned for 15 min in a UV-ozone (UVO) cleaner equipped with 184.9 and 253.7 nm dual lamp (UVO Cleaner model 144A, Jelight Co. Inc.).

Wet cleaning to remove plasma etching residuals —The cleaning solution is prepared with a commercially available R2304 (90%) and H_2O_2 (10%). The samples are immersed in the cleaning solution for 2 minutes under 50 °C and then rinsed with copious amount of water. Then rinsed with isopropyl alcohol in an ultrasonic bath for 3 minutes. Eventually annealed under 200 °C in N_2 ambient for 2.5 minutes.

Methodology

ToF-SIMS —Time-of-Flight Secondary Ion Mass Spectrometry (TOF-SIMS) analyses were performed with a TOFSIMS IV instrument from ION-TOF GmbH. The negative ion profiles were measured in a dual beam configuration using a Ga (15 keV) gun for analysis and a Xe (350 eV) gun for sputtering. Elemental depth profiles were measured in the non-interlaced mode.

XPS —The XPS measurements were carried out in angle-resolved mode using a Theta300 system from Thermo Instruments. The measurements were performed using a monochromatized Al Kα X-ray source (1486.6 eV) and a spot size of 400 micrometers.

TEM —Transmission electron microscopy (TEM) using Tecnai F30 ST from FEI operating at 300 kV was used to probe the penetration of metal atom inside low-k. TEM samples were prepared by depositing an additional

SOC layer on top of TiN followed by 5kV Pt capping layer.

XRR —High-resolution specular XRR was measured using a $\theta/2\theta$ configuration with a rotating copper anode as the radiation source using a Siemens D5000 2-circles goniometer. A fitting model was used to generate the energy density profiles from the experimental data along the normal to the sample surface. To extract the density profiles, the x-ray reflectivity data were fitted with a nonlinear least squares algorithm using the recursive multilayer method of Parratt.

Bibliography

[1] ITRS. International Technology Roadmap for Semiconductors. Technical report, 2011.

[2] J. Rimsza, L. Deng, and J. Du. Molecular dynamics simulations of nanoporous organosilicate glasses using Reactive Force Field (ReaxFF). *Journal of Non-Crystalline Solids*, 431:103–111, 2016.

[3] G. E. Moore. Cramming more components onto integrated circuits. *Electronics Magazine*, pages 114–117, 1965.

[4] R. Havemann and J. Hutchby. High-performance interconnects: an integration overview. *Proceedings of the IEEE*, 89(5):586–601, 2001.

[5] K. Maex, M. R. Baklanov, D. Shamiryan, F. Lacopi, S. H. Brongersma, and Z. S. Yanovitskaya. Low dielectric constant materials for microelectronics. *Journal of Applied Physics*, 93(11):8793–8841, 2003.

[6] V. Jousseaume, J. El Sabahy, C. Yeromonahos, G. Castellan, A. Bouamrani, and F. Ricoul. SiOCH thin films deposited by chemical vapor deposition: From low-k to chemical and biochemical sensors. *Microelectronic Engineering*, 167:69–79, 2017.

[7] F. Hoffmann, M. Cornelius, J. Morell, and M. Froba. Silica-based mesoporous organic-inorganic hybrid materials. *Angewandte Chemie International Edition*, 45(20):3216–3251, 2006.

[8] P. C. Andricacos, C. Uzoh, J. O. Dukovic, J. Horkans, and H. Deligianni. Damascene copper electroplating for chip interconnections. *IBM Journal of Research and Development*, 42(5):567–574, 1998.

[9] M. Baklanov, K. Maex, and M. Green. *Dielectric films for advanced microelectronics*. John Wiley & Sons, Ltd., Chichester, 2007.

[10] K. Fischer, M. Agostinelli, C. Allen, D. Bahr, M. Bost, P. Charvat, V. Chikarmane, Q. Fu, C. Ganpule, M. Haran, M. Heckscher, H. Hiramatsu, E. Hwang, P. Jain, I. Jin, R. Kasim, S. Kosaraju, K. S. Lee, H. Liu, R. McFadden, S. Nigam, R. Patel, C. Pelto, P. Plekhanov, M. Prince, C. Puls, S. Rajamani, D. Rao, P. Reese, A. Rosenbaum, S. Sivakumar, B. Song, M. Uncuer, S. Williams, M. Yang, P. Yashar, and S. Natarajan. Low-k interconnect stack with multi-layer air gap and tri-metal-insulator-metal capacitors for 14nm high volume manufacturing. In *2015 IEEE International Interconnect Technology Conference and 2015 IEEE Materials for Advanced Metallization Conference (IITC/MAM)*, pages 5–7, Grenoble, 2015.

[11] G. Beyer, A. Satta, J. Schuhmacher, K. Maex, W. Besling, O. Kilpela, H. Sprey, and G. Tempel. Development of sub-10-nm atomic layer deposition barriers for Cu/low-k interconnects. *Microelectronic Engineering*, 64(1-4):233–245, 2002.

[12] T. Mourier, V. Jousseaume, F. Fusalba, C. Lecornec, P. Maury, G. Passemard, P. Haumesser, S. Maitrejean, M. Cordeau, R. Pantel, F. Pierre, M. Fayolle, and H. Feldis. Porous low k pore sealing process study for 65 nm and below technologies. In *Proceedings of the IEEE 2003 International Interconnect Technology Conference*, pages 245–247, Burlingame, 2003.

[13] A. E. Kaloyeros, E. T. Eisenbraun, K. Dunn, and O. Van Der Straten. Zero thickness diffusion barriers and metallization liners for nanoscale device applications. *Chemical Engineering Communications*, 198(11):1453–1481, 2011.

[14] I. Ciofi. Performance and variability of intermediate wires. Technical report, IMEC, Leuven, 2013.

[15] ITRS. International Technology Roadmap for Semiconductors. Technical report, 2013.

[16] K. Lionti, W. Volksen, T. Magbitang, M. Darnon, and G. Dubois. Toward successful integration of porous low-k materials: strategies addressing plasma damage. *ECS Journal of Solid State Science and Technology*, 4(1):N3071–N3083, 2014.

[17] D. J. Michalak, J. M. Blackwell, J. M. Torres, A. Sengupta, L. E. Kreno, J. S. Clarke, and D. Pantuso. Porosity scaling strategies for low-k films. *Journal of Materials Research*, 30(22):3363–3385, 2015.

[18] M. Baklanov, A. Urbanowicz, G. Mannaert, and S. Vanhaelemeersch. Low dielectric constant materials: challenges of plasma damage. In *2006 8th International Conference on Solid-State and Integrated Circuit Technology Proceedings*, volume 234, pages 291–294, 2006.

[19] M. A. Worsley, S. F. Bent, S. M. Gates, N. C. M. Fuller, W. Volksen, M. Steen, and T. Dalton. Effect of plasma interactions with low-k films as a function of porosity, plasma chemistry, and temperature. *Journal of Vacuum Science & Technology B*, 23(2):395, 2005.

[20] J. Shoeb and M. J. Kushner. Mechanisms for sealing of porous low-k SiOCH by combined He and NH3 plasma treatment. *Journal of Vacuum Science & Technology A*, 29(5):051305, 2011.

[21] F. Goethals, M. R. Baklanov, I. Ciofi, C. Detavernier, P. Van Der Voort, and I. Van Driessche. A new procedure to seal the pores

of mesoporous low-k films with precondensed organosilica oligomers. *Chemical Communications*, 48(22):2797, 2012.

[22] T. Abell and K. Maex. Damage minimized plasma pore sealing of microporous low-k dielectrics. *Microelectronic Engineering*, 76(1-4):16–19, 2004.

[23] K. Yanai, T. Hasebe, K. Sumiya, S. Oguni, and K. Koga. Double-layered structure of surface modification of low-k dielectrics induced by He plasma. In *Symposium on Materials, Technology and Reliability of Advanced Interconnects held at the 2005 MRS Spring Meeting*, pages 159–163, San Francisco, 2005.

[24] O. Braginsky, A. S. Kovalev, D. V. Lopaev, E. M. Malykhin, Y. A. Mankelevich, O. V. Proshina, T. V. Rakhimova, A. T. Rakhimov, D. G. Voloshin, A. N. Vasilieva, S. M. Zyryanov, E. A. Smirnov, and M. R. Baklanov. The effect of He plasma treatment on properties of organosilicate glass low-k films. *Journal of Applied Physics*, 109(4):043303, 2011.

[25] H. Cui, R. J. Carter, D. L. Moore, H.-G. Peng, D. W. Gidley, and P. A. Burke. Impact of reductive N2 / H2 plasma on porous low-dielectric constant SiCOH thin films. *Journal of Applied Physics*, 97(11):113302, 2005.

[26] H.-G. Peng, D.-Z. Chi, W.-D. Wang, J.-H. Li, K.-Y. Zeng, R. S. Vallery, W. E. Frieze, M. A. Skalsey, D. W. Gidley, and A. F. Yee. Pore sealing by NH3 plasma treatment of porous low dielectric constant films. *Journal of the Electrochemical Society*, 154(4):G85, 2007.

[27] M. Aimadeddine, V. Arnal, A. Farcy, C. Guedj, T. Chevolleau, N. Posseme, T. David, M. Assous, O. Louveau, F. Volpi, and J. Torres. Impact of patterning and ashing on electrical properties and reliability of interconnects in a porous SiOCH ultra low-k dielectric material. *Microelectronic Engineering*, 82(3-4):341–347, 2005.

[28] W. Puyrenier, V. Rouessac, L. Broussous, D. Rébiscoul, and A. Ayral. Effect of plasma treatments on a porous low-k material – Study of pore sealing. *Microporous and Mesoporous Materials*, 106(1-3):40–48, 2007.

[29] N. Posseme, T. Chevolleau, T. David, M. Darnon, J. Barnes, O. Louveau, C. Licitra, D. Jalabert, H. Feldis, M. Fayolle, and O. Joubert. Efficiency of reducing and oxidizing ash plasmas in preventing metallic barrier diffusion into porous SiOCH. *Microelectronic Engineering*, 85(8):1842–1849, 2008.

[30] C. M. Whelan, Q. T. Le, F. Cecchet, A. Satta, J.-J. Pireaux, P. Rudolf, and K. Maex. Sealing of porous low-k dielectrics. *Electrochemical and Solid-State Letters*, 7(2):F8, 2004.

[31] M. Aimadeddine, V. Arnal, R. Roy, A. Farcy, T. David, T. Chevolleau, N. Posseme, J. Vitiello, L. Chapelon, C. Guedj, Y. Brechet, F. Volpi, and J. Torres. Effect of CH4 plasma on porous dielectric modification & pore sealing for advanced interconnect technology nodes. In *Proceedings of the IEEE 2006 international interconnect technology conference*, pages 81–83, Burlingame, 2006.

[32] D. Rebiscoul, L. Broussous, W. Puyrenier, V. Rouessac, A. Ayral, and R. Cubitt. Study of solvent penetration inside a porous low k material by neutron reflectometry - Influence of material surface modifications and of solvent properties. *Microelectronic Engineering*, 85(10):2089–2093, 2008.

[33] A. M. Urbanowicz, M. R. Baklanov, J. Heijlen, Y. Travaly, and A. Cockburn. Damage reduction and sealing of low-k films by combined He and NH3 plasma treatment. *Electrochemical and Solid-State Letters*, 10(10):G76, 2007.

[34] F. Iacopi. *Ultra-low-k dielectrics in advanced on-chip interconnects: analysis and perspectives for manufacturing and reliability.* PhD thesis, KU Leuven, 2004.

[35] J. Bonitz, S. Schulz, and T. Gessner. Ultra thin CVD TiN layers as diffusion barrier films on porous low-k materials. *Microelectronic Engineering*, 76(1-4):82–88, 2004.

[36] Z. Chen, K. Prasad, C. Y. Li, P. W. Lu, S. S. Su, L. J. Tang, D. Gui, S. Balakumar, R. Shu, and R. Kumar. Dielectric/metal sidewall diffusion barrier for Cu/porous ultralow-k interconnect technology. *Applied Physics Letters*, 84(13):2442–2444, 2004.

[37] Z. Chen, K. Prasad, C. Li, N. Jiang, and D. Gui. Investigation of dielectric/metal bilayer sidewall diffusion barrier for Cu/porous ultra-low-k interconnects. *IEEE Transactions on Device and Materials Reliability*, 5(1):133–141, 2005.

[38] P. de Rouffignac, Z. Li, and R. G. Gordon. Sealing porous low-k dielectrics with silica. *Electrochemical and Solid-State Letters*, 7(12):G306, 2004.

[39] V. Jousseaume, M. Fayolle, C. Guedj, P. H. Haumesser, C. Huguet, F. Pierre, R. Pantel, H. Feldis, and G. Passemard. Pore sealing of a porous dielectric by using a thin PECVD a-SiC:H conformal liner. *Journal of the Electrochemical Society*, 152(10):F156, 2005.

[40] Y.-B. Jiang, N. Liu, H. Gerung, J. L. Cecchi, and C. J. Brinker. Nanometer-thick conformal pore sealing of self-assembled mesoporous silica by plasma-assisted atomic layer deposition. *Journal of the American Chemical Society*, 128(34):11018–11019, 2006.

[41] W. J. Ahearn, P. R. Fitzpatrick, and J. G. Ekerdt. Sealing ultralow-k porous dielectrics with thin boron carbonitride films. *Journal of Vacuum Science & Technology A*, 25(3):570–574, 2007.

[42] Y. Kimura, A. Kobayashi, D. Ishikawa, A. Nakano, K. Matsushita, and N. Kobayashi. Plasma enhanced ALD pore sealing for highly porous SiOCH films with k = 2.0. In *2012 IEEE International Interconnect Technology Conference*, pages 1–3, San Jose, 2012.

[43] D. Ishikawa, A. Kobayashi, A. Nakano, Y. Kimura, K. Matsushita, N. Kobayashi, G. Ditmer, and A. Kiermasz. Plasma-enhanced atomic layer deposition sealing property on extreme low- k film with k = 2.0 quantified by mass metrology. *Japanese Journal of Applied Physics*, 52(5S3):05FG01, 2013.

[44] C. Jezewski, C. J. Wiegand, D. Ye, A. Mallikarjunan, D. Liu, C. Jin, W. A. Lanford, G.-C. Wang, J. J. Senkevich, and T.-M. Lu. Molecular caulking: a pore sealing CVD polymer for ultralow-k dielectrics. *Journal of the Electrochemical Society*, 151(7):F157, 2004.

[45] J. S. Juneja, P.-I. Wang, T. Karabacak, and T.-M. Lu. Dielectric barriers, pore sealing, and metallization. *Thin Solid Films*, 504(1-2):239–242, 2006.

[46] Y. Ou, P.-I. Wang, L. H. Vanamurthy, H. Bakhru, T.-M. Lu, and G. Spencer. Thermal stability study of pore sealing using parylene N. *Journal of the Electrochemical Society*, 155(10):H819, 2008.

[47] F. Goethals, E. Levrau, E. De Canck, M. Baklanov, C. Detavernier, I. Van Driessche, and P. Van Der Voort. Pore narrowing of mesoporous silica materials. *Materials*, 6(2):570–579, 2013.

[48] F. Goethals, E. Levrau, G. Pollefeyt, M. R. Baklanov, I. Ciofi, K. Vanstreels, C. Detavernier, I. Van Driessche, and P. Van Der Voort. Sealed ultra low-k organosilica films with improved electrical, mechanical and chemical properties. *Journal of Materials Chemistry C*, 1(25):3961, 2013.

[49] H. Zhou and S. F. Bent. Highly stable ultrathin carbosiloxane films by molecular layer deposition. *The Journal of Physical Chemistry C*, 117(39):19967–19973, 2013.

[50] Y. Chung, S. Lee, C. Mahata, J. Seo, S.-M. Lim, M.-s. Jeong, H. Jung, Y.-C. Joo, Y.-B. Park, H. Kim, and T. Lee. Coupled self-assembled monolayer for enhancement of Cu diffusion barrier and adhesion properties. *RSC Advances*, 4(104):60123–60130, 2014.

[51] D. Dictus, Y. Dordi, E. Gurer, M. Krishtab, M. Baklanov, and L. Carbonell. Development of a new metallization scheme for making nanoscale interconnects based on plasma-functionalization and electroless deposition. In *2013 Materials for Advanced Metallization - MAM*, pages 261–262, 2013.

[52] Y. Kayaba, H. Tanaka, T. Suzuki, K. Kohmura, and S. S. Ono. Selective formation of an ultra-thin pore seal on mesorporous low-k for a copper dual damascene structure. In *2014 IEEE International Interconnect Technology Conference / Advanced Metallization Conference (IITC/AMC)*, pages 261–263, San Jose, 2014.

[53] A. M. Caro, S. Armini, O. Richard, G. Maes, G. Borghs, C. M. Whelan, and Y. Travaly. Bottom-up engineering of subnanometer copper diffusion barriers using NH2-derived self-assembled monolayers. *Advanced Functional Materials*, 20(7):1125–1131, 2010.

[54] A. Uedono, S. Armini, Y. Zhang, T. Kakizaki, R. Krause-Rehberg, W. Anwand, and A. Wagner. Surface sealing using self-assembled monolayers and its effect on metal diffusion in porous low-k dielectrics studied using monoenergetic positron beams. *Applied Surface Science*, 368:272–276, 2016.

[55] S. Armini, J. L. Prado, M. Krishtab, J. Swerts, P. Verdonck, J. Meersschaut, T. Conard, M. Blauw, H. Struyf, and M. R. Baklanov.

Pore sealing of k 2.0 dielectrics assisted by self-assembled monolayers deposited from vapor phase. *Microelectronic Engineering*, 120:240–245, 2014.

[56] F. Iacopi, Z. Tokei, Q. T. Le, D. Shamiryan, T. Conard, B. Brijs, U. Kreissig, M. Van Hove, and K. Maex. Factors affecting an efficient sealing of porous low- k dielectrics by physical vapor deposition Ta(N) thin films. *Journal of Applied Physics*, 92(3):1548–1554, 2002.

[57] X. Chen, D. Gui, D. Chi, W. Wang, N. Babu, N. Hwang, G. Lo, R. Kumar, N. Balasubramanian, and D.-L. Kwong. Study of Ta-barrier and pore sealing dielectric layer interaction for enhanced barrier performance of Cu/ultralow k interconnects. *IEEE Electron Device Letters*, 26(9):616–618, 2005.

[58] Y.-B. Jiang, G. Xomeritakis, Z. Chen, D. Dunphy, D. J. Kissel, J. L. Cecchi, and C. J. Brinker. Sub-10 nm thick microporous membranes made by plasma-defined atomic layer deposition of a bridged silsesquioxane precursor. *Journal of the American Chemical Society*, 129(50):15446–15447, 2007.

[59] A. Ulman. Formation and structure of self-assembled monolayers. *Chemical reviews*, 96(4):1533–1554, 1996.

[60] S. Altmann and J. Pfeiffer. The hydrolysis/condensation behaviour of methacryloyloxyalkylfunctional alkoxysilanes: structure-reactivity relations. *Monatshefte fur Chemie / Chemical Monthly*, 134(8):1081–1092, 2003.

[61] B. Arkles. Tailoring surfaces with silanes. *Chemtech*, 7(12):766–778, 1977.

[62] J. Heo, S.-J. Won, D. Eom, S. Y. Lee, Y. B. Ahn, C. S. Hwang, and H. J. Kim. The role of the methyl and hydroxyl groups of low-k dielectric

films on the nucleation of ruthenium by ALD. *Electrochemical and Solid-State Letters*, 11(8):H210, 2008.

[63] J. Heo, S. Y. Lee, D. Eom, C. S. Hwang, and H. J. Kim. Enhanced nucleation behavior of atomic-layer-deposited Ru film on low-k dielectrics afforded by UV-O3 treatment. *Electrochemical and Solid-State Letters*, 11(2):G5, 2008.

[64] J. Liu, J. Bao, M. Scharnberg, W. C. Kim, P. S. Ho, and R. Laxman. Effects of surface chemistry on ALD Ta3N5 barrier formation on low-k dielectrics. *Journal of Vacuum Science & Technology A*, 23(4):1107–1113, 2005.

[65] J. W. Elam, C. A. Wilson, M. Schuisky, Z. A. Sechrist, and S. M. George. Improved nucleation of TiN atomic layer deposition films on SiLK low-k polymer dielectric using an Al2O3 atomic layer deposition adhesion layer. *Journal of Vacuum Science & Technology B*, 21(3):1099, 2003.

[66] N. Jourdan, M. B. Krishtab, M. R. Baklanov, J. Meersschaut, C. J. Wilson, J. M. Ablett, E. Fonda, L. Zhao, S. Van Elshocht, Z. Tokei, and E. Vancoille. Study of chemical vapor deposition of manganese on porous SiCOH low-k dielectrics using bis(ethylcyclopentadienyl)manganese. *Electrochemical and Solid-State Letters*, 15(5):H176, 2012.

[67] S. Armini, J. L. Prado, J. Swerts, Y. Sun, M. Krishtab, J. Meersschaut, M. Blauw, M. Baklanov, and P. Verdonck. Pore sealing of porous ultralow-k dielectrics by self-assembled monolayers combined with atomic layer deposition. *ECS Solid State Letters*, 1(2):P42–P44, 2012.

[68] Y. Sun, A. R. Negreira, J. Meersschaut, I. Hoflijk, I. Vaesen, T. Conard, H. Struyf, Z. Tokei, J. Boemmels, M. Moinpour, S. De Feyter, and S. Armini. Optimization and upscaling of spin coating

with organosilane monolayers for low-k pore sealing. *Microelectronic Engineering*, 167:32–36, 2017.

[69] Y. Sun, M. Krishtab, H. Struyf, P. Verdonck, S. De Feyter, M. R. Baklanov, and S. Armini. Impact of plasma pretreatment and pore size on the sealing of ultra-low-k dielectrics by self-assembled monolayers. *Langmuir*, 30(13):3832–3844, 2014.

[70] S. Armini, J. Loyo Prado, M. Krishtab, T. Conard, J. Meersschaut, Q. T. Le, P. Verdonck, and M. R. Baklanov. Study of wet surface activation routes to enable the deposition of monomolecular organic thin films on k 2.0 porous dielectrics. *ECS Journal of Solid State Science and Technology*, 3(1):N3106–N3111, 2014.

[71] L. Guo, X. Qin, and F. Zaera. Chemical treatment of low-k dielectric surfaces for patterning of thin solid films in microelectronic applications. *ACS Applied Materials & Interfaces*, 8(9):6293–6300, 2016.

[72] M.-S. Kuo. *Rational design of non-damaging capacitively coupled plasma etching and photoresist stripping processes for ultralow k dielectric materials.* PhD thesis, University of Maryland, 2010.

[73] H. Shi. *Mechanistic study of plasma damage to porous low-k: process development and dielectric recovery.* PhD thesis, University of Texas in Austin, 2010.

[74] A. Grill and V. Patel. Ultralow-k dielectrics prepared by plasma-enhanced chemical vapor deposition. *Applied Physics Letters*, 79(6):803–805, 2001.

[75] Y. Sun, M. Krishtab, Y. Mankelevich, L. Zhang, S. De Feyter, M. Baklanov, and S. Armini. Surface-confined activation of ultra low-k dielectrics in CO2 plasma. *Applied Physics Letters*, 108(26):262902, 2016.

[76] T. Frot, W. Volksen, S. Purushothaman, R. Bruce, and G. Dubois. Application of the protection/deprotection strategy to the science of porous materials. *Advanced Materials*, 23(25):2828–2832, 2011.

[77] T. Frot, W. Volksen, S. Purushothaman, R. L. Bruce, T. Magbitang, D. C. Miller, V. R. Deline, and G. Dubois. Post porosity plasma protection: scaling of efficiency with porosity. *Advanced Functional Materials*, 22(14):3043–3050, 2012.

[78] L. Zhang. *Innovative solutions for advanced interconnects using ultra low-k dielectrics*. PhD thesis, KU Leuven, 2017.

[79] M. H. Heyne, L. Zhang, J. Liu, I. Ahmad, D. Toma, J. de Marneffe, S. De Gendt, and M. R. Baklanov. Quantitative characterization of pore stuffing and unstuffing for postporosity plasma protection of low-k materials. *Journal of Vacuum Science & Technology B*, 32(6):062202, 2014.

[80] C. M. Whelan, A. C. Demas, A. Romo Negreira, T. Fernandez Landaluce, J. Schuhmacher, L. Carbonell, and K. Maex. Surface engineering using self-assembled monolayers: model substrates for atomic-layer deposition. In E. Zschech, C. Whelan, and T. Mikolajick, editors, *Materials for Information Technology*, pages 69–76. Springer-Verlag, London, 2006.

[81] H. Toyodome, Y. Kaneko, K. Shikinaka, and N. Iyi. Preparation of carboxylate group-containing rod-like polysilsesquioxane with hexagonally stacked structure by sol–gel reaction of 2-cyanoethyltriethoxysilane. *Polymer*, 53(26):6021–6026, 2012.

[82] S. A. Jadhav. Self-assembled monolayers (SAMs) of carboxylic acids: an overview. *Central European Journal of Chemistry*, 9(3):369–378, 2011.

[83] Z. Kong, Q. Wang, and L. Ding. Self-assembling of cyano- and carboxyl-terminated monolayers using short-chain alkylsiloxane. *Applied Surface Science*, 256(5):1372–1376, 2009.

[84] S. M. George, B. Yoon, and A. A. Dameron. Surface chemistry for molecular layer deposition of organic and hybrid organic-inorganic polymers. *Accounts of Chemical Research*, 42(4):498–508, 2009.

[85] D. Xin and Q. Han. Study on interfacial interaction energy of Cu–SAM–epoxy systems in a hot and humid environment. *Journal of Adhesion Science and Technology*, 28(5):434–443, 2014.

[86] A. Grill and D. A. Neumayer. Structure of low dielectric constant to extreme low dielectric constant SiCOH films: Fourier transform infrared spectroscopy characterization. *Journal of Applied Physics*, 94(10):6697–6707, 2003.

[87] R. Hiremath, J. A. Basile, S. W. Varney, and J. A. Swift. Controlling molecular crystal polymorphism with self-assembled monolayer templates. *Journal of the American Chemical Society*, 127(51):18321–18327, 2005.

[88] D. Shamiryan. *Novel application of ellipsometry and solvent probes for characterising Cu/low-k dielectric materials for advanced semiconductor interconnects*. PhD thesis, KU Leuven, 2004.

[89] M. Baklanov and K. Mogilnikov. Non-destructive characterisation of porous low-k dielectric films. *Microelectronic Engineering*, 64(1-4):335–349, 2002.

[90] M. R. Baklanov, K. P. Mogilnikov, V. G. Polovinkin, and F. N. Dultsev. Determination of pore size distribution in thin films by ellipsometric porosimetry. *Journal of Vacuum Science & Technology B*, 18(3):1385, 2000.

[91] D. Shamiryan, M. R. Baklanov, and K. Maex. Diffusion barrier integrity evaluation by ellipsometric porosimetry. *Journal of Vacuum Science & Technology B*, 21(1):220, 2003.

[92] S. Gregg and K. Sing. *Adsorption, surface area and porosity.* Academic Press, 1982.

[93] G. Andersson, H. Morgner, and H. Pohl. Energy-loss straggling of helium projectiles at low kinetic energies: Deconvolution of concentration depth profiles of inorganic salt solutes in aqueous solutions. *Physical Review A*, 78(3):032904, 2008.

[94] I. Ciofi, M. R. Baklanov, Z. Tokei, and G. P. Beyer. Capacitance measurements and k-value extractions of low-k films. *Microelectronic Engineering*, 87(11):2391–2406, 2010.

[95] T. Rakhimova, A. Rakhimov, Y. Mankelevich, D. Lopaev, A. Kovalev, A. Vasil'eva, S. Zyryanov, K. Kurchikov, O. Proshina, D. Voloshin, N. Novikova, M. Krishtab, and M. Baklanov. Low-k films modification under EUV and VUV radiation. *Journal of Physics D: Applied Physics*, 47(2):025102, 2014.

[96] E. Kunnen, M. R. Baklanov, A. Franquet, D. Shamiryan, T. V. Rakhimova, A. M. Urbanowicz, H. Struyf, and W. Boullart. Effect of energetic ions on plasma damage of porous SiCOH low-k materials. *Journal of Vacuum Science & Technology B*, 28(3):450–459, 2010.

[97] S. Desbief, L. Patrone, D. Goguenheim, D. Guerin, and D. Vuillaume. Impact of chain length, temperature, and humidity on the growth of long alkyltrichlorosilane self-assembled monolayers. *Physical Chemistry Chemical Physics*, 13(7):2870–2879, 2011.

[98] P. Marsik, A. M. Urbanowicz, P. Verdonck, D. De Roest, H. Sprey, and M. R. Baklanov. Effect of ultraviolet curing wavelength on low-k

dielectric material properties and plasma damage resistance. *Thin Solid Films*, 519(11):3619–3626, 2011.

[99] M. Niwano, J. Kageyama, K. Kinashi, J. Sawahata, and N. Miyamoto. Oxidation of hydrogen-terminated Si surfaces studied by infrared spectroscopy. *Surface Science*, 301(1-3):L245–L249, 1994.

[100] M. Tanaka, T. Sawaguchi, M. Kuwahara, and O. Niwa. Surface modification of silicon oxide with trialkoxysilanes toward close-packed monolayer formation. *Langmuir*, 29(21):6361–6368, 2013.

[101] M. R. Baklanov, J.-F. de Marneffe, D. Shamiryan, A. M. Urbanowicz, H. Shi, T. V. Rakhimova, H. Huang, and P. S. Ho. Plasma processing of low-k dielectrics. *Journal of Applied Physics*, 113(4):041101, 2013.

[102] J. Shoeb, M. M. Wang, and M. J. Kushner. Damage by radicals and photons during plasma cleaning of porous low- k SiOCH. I. Ar/O2 and He/H2 plasmas. *Journal of Vacuum Science & Technology A*, 30(4):041303, 2012.

[103] J. Shoeb and M. J. Kushner. Damage by radicals and photons during plasma cleaning of porous low- k SiOCH. II. Water uptake and change in dielectric constant. *Journal of Vacuum Science & Technology A: Vacuum, Surfaces, and Films*, 30(4):041304, jul 2012.

[104] T. Rakhimova, O. Braginsky, A. Kovalev, D. Lopaev, Y. Mankelevich, E. Malykhin, A. Rakhimov, A. Vasilieva, S. Zyryanov, and M. Baklanov. Recombination of O and H atoms on the surface of nanoporous dielectrics. *IEEE Transactions on Plasma Science*, 37(9):1697–1704, 2009.

[105] J. A. Lim, J. H. Cho, Y. Jang, J. T. Han, and K. Cho. Precise control of surface wettability of mixed monolayers using a simple wiping method. *Thin Solid Films*, 515(4):2079–2084, 2006.

[106] A. Ulman. *An introduction to ultrathin organic films*. Academic Press, Inc., Boston, 1991.

[107] M. J. Stevens. Thoughts on the structure of alkylsilane monolayers. *Langmuir*, 15(8):2773–2778, 1999.

[108] F. Tielens, C. Gervais, J. F. Lambert, F. Mauri, and D. Costa. Ab initio study of the hydroxylated surface of amorphous silica: a representative model. *Chemistry of Materials*, 20(10):3336–3344, 2008.

[109] F. Bernardoni, M. Kouba, and A. Y. Fadeev. Effect of curvature on the packing and ordering of organosilane monolayers supported on solids. *Chemistry of Materials*, 20(2):382–387, 2008.

[110] J. Lee and D. B. Graves. Synergistic damage effects of vacuum ultraviolet photons and O2 in SiCOH ultra-low-k dielectric films. *Journal of Physics D: Applied Physics*, 43(42):425201, 2010.

[111] F. Iacopi, J. H. Choi, K. Terashima, P. M. Rice, and G. Dubois. Cryogenic plasmas for controlled processing of nanoporous materials. *Physical Chemistry Chemical Physics*, 13(9):3634, 2011.

[112] E. Feresenbet, D. Raghavan, and G. A. Holmes. The role of the terminal functional group of self-assembled monolayers on fiber matrix adhesion. *Journal of Applied Polymer Science*, 106(1):462–469, 2007.

[113] J. Deval, T. A. Umali, B. L. Spencer, E. H. Lan, B. Dunn, and C.-M. Ho. Reconfigurable hydrophobic/hydrophilic surfaces based on self-assembled monolayers. In *Symposium on Materials Inspired by Biology held at the the MRS Spring Meeting*, volume 774, pages 203–208, San Francisco, 2003.

[114] Y. Sun, E. Levrau, M. Blauw, J. Meersschaut, P. Verdonck, H. Struyf, C. Detavernier, M. Baklanov, S. De Feyter, and S. Armini. Sealing

of low-k dielectric (k=2.0) with self-assembled monolayers (SAMs) for the atomic layer deposition (ALD) of TiN. *MRS Proceedings*, 1559(9):mrss13–1559–aa05–22, 2013.

[115] A. M. Urbanowicz, D. Shamiryan, A. Zaka, P. Verdonck, S. De Gendt, and M. R. Baklanov. Effects of He plasma pretreatment on low-k damage during Cu surface cleaning with NH3 plasma. *Journal of the Electrochemical Society*, 157(5):H565, 2010.

[116] J. Lee and D. B. Graves. Roles of plasma-generated vacuum-ultraviolet photons and oxygen radicals in damaging nanoporous low-k films. *Journal of Vacuum Science & Technology A*, 31(4):041302, 2013.

[117] J. Shoeb and M. J. Kushner. Polymer cleaning from porous low-dielectrics in He/H2 plasmas. *IEEE Transactions on Plasma Science*, 39(11):2828–2829, 2011.

[118] Y. C. Kim and M. Boudart. Recombination of oxygen, nitrogen, and hydrogen atoms on silica: kinetics and mechanism. *Langmuir*, 7(12):2999–3005, 1991.

[119] J. R. Woodworth, M. E. Riley, V. A. Amatucci, T. W. Hamilton, and B. P. Aragon. Absolute intensities of the vacuum ultraviolet spectra in oxide etch plasma processing discharges. *Journal of Vacuum Science & Technology A*, 19(1):45–55, 2001.

[120] E. Levrau, K. Devloo-Casier, J. Dendooven, K. F. Ludwig, P. Verdonck, J. Meersschaut, M. R. Baklanov, and C. Detavernier. Atomic layer deposition of TiO2 on surface modified nanoporous low-k films. *Langmuir*, 29(39):12284–12289, 2013.

[121] L. Abelmann and C. Lodder. Oblique evaporation and surface diffusion. *Thin Solid Films*, 305(1-2):1–21, 1997.

[122] Q. T. Le, E. Kesters, S. Decoster, B. T. Chan, M. P. Nguyen, T. Conard, A. Vanleenhove, F. Holsteyns, and S. De Gendt. Characterization of patterned porous low- k dielectrics: surface sealing and residue removal by wet processing/cleaning. *ECS Journal of Solid State Science and Technology*, 5(3):N5–N9, 2016.

[123] V. G. Polovinkin and M. R. Baklanov. Materials characterization by ellipsometry. In B. Derby, editor, *Engineering Materials and Processes*, pages 461–473. Springer-Verlag, London, 2005.

[124] T. Ohwaki, M. Takeda, and Y. Takai. Characterization of silicon native oxide formed in SC-1, H2O2 and wet ozone processes. *Japanese Journal of Applied Physics*, 36(9A):5507–5513, 1997.

[125] Y.-L. Wang, C. Liu, S.-T. Chang, M.-S. Tsai, M.-S. Feng, and W.-T Tseng. Chemical-mechanical polishing of low-dielectric-constant spin-on-glasses: film chemistries, slurry formulation and polish selectivity. *Thin Solid Films*, 308:550–554, 1997.

[126] P.-H. Chen, H.-Y. Peng, C.-M. Hsieh, and M. K. Chyu. The characteristic behavior of TMAH water solution for anisotropic etching on both Silicon substrate and SiO2 layer. *Sensors and Actuators A: Physical*, 93(2):132–137, 2001.

[127] K. Yamamoto, A. Nakamura, and U. Hase. Control of cleaning performance of an ammonia and hydrogen peroxide mixture (APM) on the basis of a kinetic reaction model. *IEEE Transactions on Semiconductor Manufacturing*, 12(3):288–294, 1999.

[128] D. M. Knotter. Etching mechanism of vitreous silicon dioxide in HF-based solutions. *Journal of the American Chemical Society*, 122(18):4345–4351, 2000.

[129] R. L. Jones, N. C. Pearsall, and J. D. Batteas. Disorder in alkylsilane monolayers assembled on surfaces with nanoscopic curvature. *The Journal of Physical Chemistry C*, 113(11):4507–4514, 2009.

[130] P. Lazzeri, G. J. Stueber, G. S. Oehrlein, R. McGowan, E. Busch, S. Pederzoli, M. Bersani, and M. Anderle. Time of flight secondary ion mass spectroscopy investigation of ultralow-k dielectric modifications in hydrogen and deuterium plasmas. *Journal of Vacuum Science & Technology B*, 24(6):2695, 2006.

[131] K. Van Laer, S. Tinck, V. Samara, J. de Marneffe, and A. Bogaerts. Etching of low-k materials for microelectronics applications by means of a N2/H2 plasma: modeling and experimental investigation. *Plasma Sources Science and Technology*, 22(2):025011, 2013.

[132] H.-S. Lu, K. Gottfried, N. Ahner, S. Schulz, and X.-P. Qu. Investigation of CH4, NH3, H2 and He plasma treatment on porous low-k films and its effects on resisting moisture absorption and ions penetration. *Microelectronic Engineering*, 106:85–90, 2013.

[133] Y. Sun, E. Levrau, L. Zhang, J. Geypen, J. Meersschaut, A. Franquet, Q. T. Le, J.-F. de Marneffe, H. Bender, H. Struyf, C. Detavernier, M. M. Baklanov, S. De Feyter, and S. Armini. Stuffing-enabled surface confinement of silanes used as sealing agents on CF4 plasma-exposed 2.0 p-OSG films. *Microelectronic Engineering*, 137:70–74, 2015.

[134] M. R. Baklanov, K. P. Mogilnikov, and Q. T. Le. Quantification of processing damage in porous low dielectric constant films. *Microelectronic Engineering*, 83(11-12):2287–2291, 2006.

[135] F. Iacopi, Y. Travaly, M. Van Hove, A. Jonas, J. Molina-Aldareguia, M. Elizalde, and I. Ocana. Extent of plasma damage to porous organosilicate films characterized with nanoindentation, x-ray reflectivity, and surface acoustic waves. *Journal of Materials Research*, 21(12):3161–3167, 2006.

[136] O. Braginsky, A. Kovalev, D. Lopaev, E. Malykhin, Y. Mankelevich, T. Rakhimova, A. Rakhimov, A. Vasilieva, S. Zyryanov, and M. Baklanov. The mechanism of low-k SiOCH film modification by oxygen atoms. *Journal of Applied Physics*, 108(7):073303, 2010.

[137] Y. Susa, H. Ohtake, Z. Jianping, L. Chen, and T. Nozawa. Characterization of CO2 plasma ashing for less low-dielectric-constant film damage. *Journal of Vacuum Science & Technology A*, 33(6):061307, 2015.

[138] S. H. M. Wandurraga. *Reduced reaction kinetics model for CO2 dissociation in non-thermal microwave discharges.* PhD thesis, Delft University of Technology, 2015.

[139] P. G. Reyes, E. F. Mendez, D. Osorio-Gonzalez, F. Castillo, and H. Martinez. Optical emission spectroscopy of CO2 glow discharge at low pressure. *Physica status solidi (C)*, 5(4):907–910, 2008.

[140] R. W. B. Pearse and A. G. Gaydon. *The identification of molecular spectra.* Chapman and Hall Ltd., 1965.

[141] T. T. Olawumi, E. Levrau, M. Krishtab, C. Detavernier, J. W. Bartha, K. Xu, F. Lazzarino, and M. R. Baklanov. Modification of ultra low-k dielectric films by O2 and CO2 plasmas. *ECS Journal of Solid State Science and Technology*, 4(1):N3048–N3057, 2014.

[142] N. Posseme, T. Chevolleau, O. Joubert, L. Vallier, and N. Rochat. Etching of porous SiOCH materials in fluorocarbon-based plasmas. *Journal of Vacuum Science & Technology B*, 22(6):2772, 2004.

[143] Q. T. Le, J.-F. de Marneffe, T. Conard, I. Vaesen, H. Struyf, and G. Vereecke. Effect of UV irradiation on modification and subsequent wet removal of model and post-etch fluorocarbon residues. *Journal of the Electrochemical Society*, 159(3):H208–H213, 2012.

[144] Z. El Otell, V. Samara, A. Zotovich, T. Hansen, J.-F. de Marneffe, and M. R. Baklanov. Vacuum ultra-violet emission of CF4 and CF3I containing plasmas and Their effect on low-k materials. *Journal of Physics D: Applied Physics*, 48(39):395202, 2015.

[145] B. Jinnai, S. Fukuda, H. Ohtake, and S. Samukawa. Prediction of UV spectra and UV-radiation damage in actual plasma etching processes using on-wafer monitoring technique. *Journal of Applied Physics*, 107(4):043302, 2010.

[146] L. Zhang, J.-F. de Marneffe, M. H. Heyne, S. Naumov, Y. Sun, A. Zotovich, Z. El Otell, F. Vajda, S. De Gendt, and M. R. Baklanov. Improved plasma resistance for porous low-k dielectrics by pore stuffing approach. *ECS Journal of Solid State Science and Technology*, 4(1):N3098–N3107, 2014.

[147] D. J. Russell. NIST Computational Chemistry Comparison and Benchmark Database, 2017.

[148] L.-O. Srisombat, S. Zhang, and T. R. Lee. Thermal stability of mono-, bis-, and tris-chelating alkanethiol films assembled on gold nanoparticles and evaporated "flat" gold. *Langmuir*, 26(1):41–46, 2010.

[149] A. Chauhan, D. Aswal, S. Koiry, S. Gupta, J. Yakhmi, C. Surgers, D. Guerin, S. Lenfant, and D. Vuillaume. Self-assembly of the 3-aminopropyltrimethoxysilane multilayers on Si and hysteretic current–voltage characteristics. *Applied Physics A*, 90(3):581–589, 2007.

[150] L. Russo, L. Gabrielli, E. M. Valliant, F. Nicotra, J. Jimenez-Barbero, L. Cipolla, and J. R. Jones. Novel silica/bis(3-aminopropyl) polyethylene glycol inorganic/organic hybrids by sol–gel chemistry. *Materials Chemistry and Physics*, 140(1):168–175, 2013.

[151] S.-H. Kim, H. Ohtsuka, M. C. R. Tria, K. Tanaka, R. C. Advincula, and H. Usui. Preparation of surface-tethered polymer layer on inorganic substrates by photoreactive self-assembled monolayer. *Thin Solid Films*, 554:78–83, 2014.

[152] A. Turchanin, M. El-Desawy, and A. Gölzhäuser. High thermal stability of cross-linked aromatic self-assembled monolayers: Nanopatterning via selective thermal desorption. *Applied Physics Letters*, 90(5):053102, 2007.

[153] T. R. Naik, V. Singh, M. Ravikanth, and V. R. Rao. A vapor phase self-assembly of porphyrin monolayer as a copper diffusion barrier for Back-End-of-Line CMOS technologies. *IEEE Transactions on Electron Devices*, 63(5):2009–2015, 2016.

[154] A. J. M. Mackus, A. A. Bol, and W. M. M. Kessels. The use of atomic layer deposition in advanced nanopatterning. *Nanoscale*, 6(19):10941–10960, 2014.

[155] F. S. M. Hashemi, C. Prasittichai, and S. F. Bent. A new resist for area selective atomic and molecular layer deposition on metal–dielectric patterns. *The Journal of Physical Chemistry C*, 118(20):10957–10962, 2014.

[156] T. Suni, K. Henttinen, I. Suni, and J. Makinen. Effects of plasma activation on hydrophilic bonding of Si and SiO2. *Journal of the Electrochemical Society*, 149(6):G348, 2002.

[157] J. Musschoot, Q. Xie, D. Deduytsche, S. Van den Berghe, R. Van Meirhaeghe, and C. Detavernier. Atomic layer deposition of titanium nitride from TDMAT precursor. *Microelectronic Engineering*, 86(1):72–77, 2009.

Scientific Contributions

Journals

1. **Sun, Y.**; Swerts, J.; Verdonck, P.; Maheshwari, A.; Prado, J. L.; de Feyter, S.; Armini, S. *Solid State Phenomena* 195:146–149, 2012.

2. **Sun, Y.**; Krishtab, M.; Struyf, H.; Verdonck, P.; De Feyter, S.; Baklanov, M. R.; Armini, S. *Langmuir* **2014**, 30(13):3832–3844, 2014.

3. **Sun, Y.**; Levrau, E.; Zhang, L.; Geypen, J.; Meersschaut, J.; Franquet, A.; Le, Q. T.; de Marneffe, J.-F.; Bender, H.; Struyf, H.; Detavernier, C.; Baklanov, M.; De Feyter, S.; Armini, S. *Microelectronic Engineering* 137:70–74, 2015.

4. **Sun, Y.**; Krishtab, M.; Mankelevich, Y.; Zhang, L.; De Feyter, S.; Baklanov, M.; Armini, S. *Applied Physics Letters* 108(26):262902, 2016.

5. **Sun, Y.**; Negreira, A. R.; Meersschaut, J.; Hoflijk, I.; Vaesen, I.; Struyf, H.; Tokei, Z.; Boemmels, J.; Moinpour, M.; Feyter, S. De; Armini, S. *Microelectronic Engineering* 167:32–36, 2017.

Conferences

1. **Sun, Y.**; Levrau, E.; Blauw, M.; Meersschaut, J.; Verdonck, P.; Struyf, H.; Detavernier, C.; Baklanov, M.; De Feyter, S.; Armini, S. *In MRS Proceedings*1559(5), page aa05-22, 2013.

2. **Sun, Y.**; Levrau, E.; Zhang, L.; Geypen, J.; Franquet, A.; LeQuoc, T.; DeMarneffe, J.-F.; Bender, H.; Struyf, H.; Baklanov, M.; Detavernier, C.; DeFeyter, S.; Armini, S. *In 23rd Conference on Materials for Advanced Metallization - MAM*, Chemnitz, 2014.

3. **Sun, Y.**; DeRoover, R.; Struyf, H.; DeFeyter, S.; Armini, S. *In Materials for Advanced Metallization Conference - MAM*, Brussels, page 115, 2016.

Patent

Le, Q. T.; Baklanov, M.; Sun, Y.; Silvia, A. Method For Activating A Porous Layer Surface, 2015.

FACULTY OF SCIENCE
DEPARTMENT OF CHEMISTRY
MOLECULAR IMAGING AND PHOTONICS
Kapeldreef 75
B-3001 Leuven
yiting.sun@chem.kuleuven.be
https://www.chem.kuleuven.be